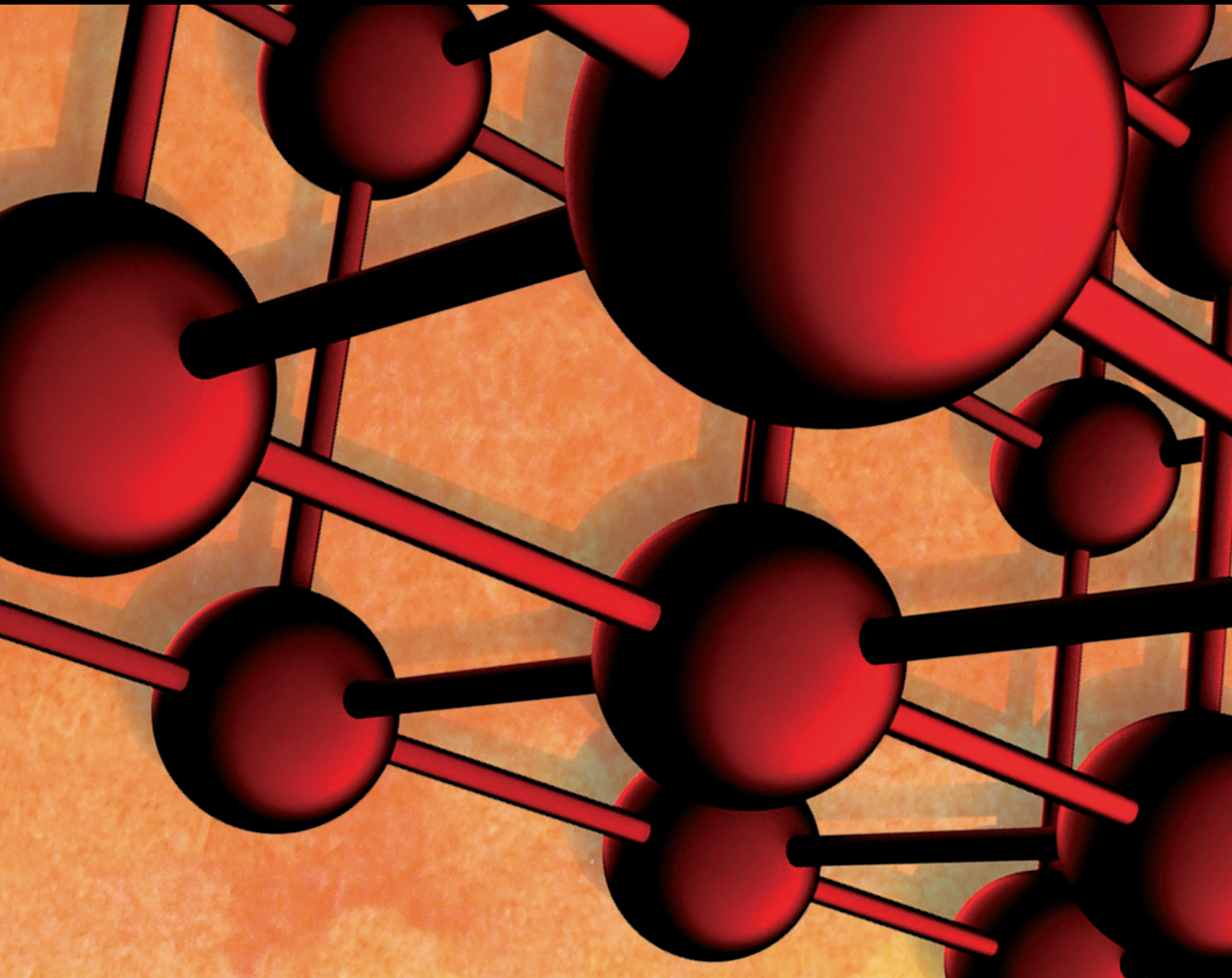


Development of High-Performance Metastable Aluminum Composites for Industrial Applications

Lead Guest Editor: Adel Mohamed

Guest Editors: Penchal Reddy and Anil Kumar Birru





Development of High-Performance Metastable Aluminum Composites for Industrial Applications

Advances in Materials Science and Engineering

Development of High-Performance Metastable Aluminum Composites for Industrial Applications

Lead Guest Editor: Adel Mohamed


Guest Editors: Penchal Reddy and Anil Kumar
Birru



Copyright © 2024 Hindawi Limited. All rights reserved.

This is a special issue published in "Advances in Materials Science and Engineering." All articles are open access articles distributed under the Creative Commons Attribution License, which permits unrestricted use, distribution, and reproduction in any medium, provided the original work is properly cited.

Chief Editor































Amit Bandyopadhyay , USA

Associate Editors

Vamsi Balla , India
Mitun Das , USA
Sandip Harimkar, USA
Ravi Kumar , India
Peter Majewski , Australia
Enzo Martinelli , Italy
Luigi Nicolais , Italy
Carlos R. Rambo , Brazil
Michael J. Schütze , Germany
Kohji Tashiro , Japan
Zhonghua Yao , China
Dongdong Yuan , China
Wei Zhou , China

Academic Editors

Antonio Abate , Germany
Hany Abdo , Saudi Arabia
H.P.S. Abdul Khalil , Malaysia
Ismael Alejandro Aguayo Villarreal , Mexico
Sheraz Ahmad , Pakistan
Michael Aizenshtein, Israel
Jarir Aktaa, Germany
Bandar AlMangour, Saudi Arabia
Huaming An, China
Alicia Esther Ares , Argentina
Siva Avudaiappan , Chile
Habib Awais , Pakistan
NEERAJ KUMAR BHOI, India
Enrico Babilio , Italy
Renal Backov, France
M Bahubalendruni , India
Sudharsan Balasubramanian , India
Markus Bambach, Germany
Irene Bavasso , Italy
Stefano Bellucci , Italy
Brahim Benmokrane, Canada
Jean-Michel Bergheau , France
Guillaume Bernard-Granger, France
Giovanni Berselli, Italy
Patrice Berthod , France
Michele Bianchi , Italy
Hugo C. Biscaia , Portugal

Antonio Boccaccio, Italy
Mohamed Bououdina , Saudi Arabia
Gianlorenzo Bussetti , Italy
Antonio Caggiano , Germany
Marco Cannas , Italy
Qi Cao, China
Gianfranco Carotenuto , Italy
Paolo Andrea Carraro , Italy
Jose Cesar de Sa , Portugal
Wen-Shao Chang , United Kingdom
Qian Chen , China
Francisco Chinesta , France
Er-Yuan Chuang , Taiwan
Francesco Colangelo, Italy
María Criado , Spain
Enrique Cuan-Urquizo , Mexico
Lucas Da Silva , Portugal
Angela De Bonis , Italy
Abílio De Jesus , Portugal
José António Fonseca De Oliveira
Correia , Portugal
Ismail Demir , Turkey
Luigi Di Benedetto , Italy
Maria Laura Di Lorenzo, Italy
Marisa Di Sabatino, Norway
Luigi Di Sarno, Italy
Ana María Díez-Pascual , Spain
Guru P. Dinda , USA
Hongbiao Dong, China
Mingdong Dong , Denmark
Frederic Dumur , France
Stanislaw Dymek, Poland
Kaveh Edalati , Japan
Philip Eisenlohr , USA
Luis Evangelista , Norway
Michele Fedel , Italy
Francisco Javier Fernández Fernández , Spain
Spain
Isabel J. Ferrer , Spain
Massimo Fresta, Italy
Samia Gad , Egypt
Pasquale Gallo , Finland
Sharanabasava Ganachari, India
Santiago Garcia-Granda , Spain
Carlos Garcia-Mateo , Spain

Achraf Ghorbal , Tunisia
Georgios I. Giannopoulos , Greece
Ivan Giorgio , Italy
Andrea Grilli , Italy
Vincenzo Guarino , Italy
Daniel Guay, Canada
Jenő Gubicza , Hungary
Xuchun Gui , China
Benoit Guiffard , France
Zhixing Guo, China
Ivan Gutierrez-Urrutia , Japan
Weiwei Han , Republic of Korea
Simo-Pekka Hannula, Finland
A. M. Hassan , Egypt
Akbar Heidarzadeh, Iran
Yi Huang , United Kingdom
Joshua Ighalo, Nigeria
Saliha Ilican , Turkey
Md Mainul Islam , Australia
Ilia Ivanov , USA
Jijo James , India
Hafsa Jamshaid , Pakistan
Hom Kandel , USA
Kenji Kaneko, Japan
Rajesh Kannan A , Democratic People's
Republic of Korea
Mehran Khan , Hong Kong
Akihiko Kimura, Japan
Ling B. Kong , Singapore
Pramod Koshy, Australia
Hongchao Kou , China
Alexander Kromka, Czech Republic
Abhinay Kumar, India
Avvaru Praveen Kumar , Ethiopia
Sachin Kumar, India
Paweł Kłosowski , Poland
Wing-Fu Lai , Hong Kong
Luciano Lamberti, Italy
Fulvio Lavecchia , Italy
Laurent Lebrun , France
Joon-Hyung Lee , Republic of Korea
Cristina Leonelli, Italy
Chenggao Li , China
Rongrong Li , China
Yuanshi Li, Canada

Guang-xing Liang , China
Barbara Liguori , Italy
Jun Liu , China
Yunqi Liu, China
Rong Lu, China
Zhiping Luo , USA
Fernando Lusquiños , Spain
Himadri Majumder , India
Dimitrios E. Manolakos , Greece
Necmettin Maraşlı , Turkey
Alessandro Martucci , Italy
Roshan Mayadunne , Australia
Mamoun Medraj , Canada
Shazim A. Memon , Kazakhstan
Pratima Meshram , India
Mohsen Mhadhbi , Tunisia
Philippe Miele, France
Andrey E. Miroshnichenko, Australia
Ajay Kumar Mishra , South Africa
Hossein Moayedi , Vietnam
Dhanesh G. Mohan , United Kingdom
Sakar Mohan , India
Namdev More, USA
Tahir Muhmood , China
Faisal Mukhtar , Pakistan
Dr. Tauseef Munawar , Pakistan
Roger Narayan , USA
Saleem Nasir , Pakistan
Elango Natarajan, Malaysia
Rufino M. Navarro, Spain
Miguel Navarro-Cia , United Kingdom
Behzad Nematollahi , Australia
Peter Niemz, Switzerland
Hiroschi Noguchi, Japan
Dariusz Oleszak , Poland
Laurent Orgéas , France
Togay Ozbakkaloglu, United Kingdom
Marián Palcut , Slovakia
Davide Palumbo , Italy
Gianfranco Palumbo , Italy
Murlidhar Patel, India
Zbyšek Pavlík , Czech Republic
Alessandro Pegoretti , Italy
Gianluca Percoco , Italy
Andrea Petrella, Italy

Claudio Pettinari , Italy
Giorgio Pia , Italy
Candido Fabrizio Pirri, Italy
Marinos Pitsikalis , Greece
Alain Portavoce , France
Simon C. Potter, Canada
Ulrich Prah, Germany
Veena Ragupathi , India
Kawaljit Singh Randhawa , India
Baskaran Rangasamy , Zambia
Paulo Reis , Portugal
Hilda E. Reynel-Avila , Mexico
Yuri Ribakov , Israel
Aniello Riccio , Italy
Anna Richelli , Italy
Antonio Riveiro , Spain
Marco Rossi , Italy
Fernando Rubio-Marcos , Spain
Francesco Ruffino , Italy
Giuseppe Ruta , Italy
Sachin Salunkhe , India
P Sangeetha , India
Carlo Santulli, Italy
Fabrizio Sarasini , Italy
Senthil Kumaran Selvaraj , India
Raffaele Sepe , Italy
Aabid H Shalla, India
Poorva Sharma , China
Mercedes Solla, Spain
Tushar Sonar , Russia
Donato Sorgente , Italy
Charles C. Sorrell , Australia
Damien Soulat , France
Adolfo Speghini , Italy
Antonino Squillace , Italy
Koichi Sugimoto, Japan
Jirapornchai Suksaeree , Thailand
Baozhong Sun, China
Sam-Shajing Sun , USA
Xiaolong Sun, China
Yongding Tian , China
Hao Tong, China
Achim Trampert, Germany
Tomasz Trzepieciński , Poland
Kavimani V , India

Matjaz Valant , Slovenia
Mostafa Vamegh, Iran
Lijing Wang , Australia
Jörg M. K. Wiezorek , USA
Guosong Wu, China
Junhui Xiao , China
Guoqiang Xie , China
YASHPAL YASHPAL, India
Anil Singh Yadav , India
Yee-wen Yen, Taiwan
Hao Yi , China
Wenbin Yi, China
Tetsu Yonezawa, Japan
Hiroshi Yoshihara , Japan
Bin Yu , China
Rahadian Zainul , Indonesia
Lenka Zaji#c#kova# , Czech Republic
Zhigang Zang , China
Michele Zappalorto , Italy
Gang Zhang, Singapore
Jinghuai Zhang, China
Zengping Zhang, China
You Zhou , Japan
Robert Černý , Czech Republic

Contents

Retracted: Influences of Aqueous Nanofluid Emulsion on Diesel Engine Performance, Combustion, and Emission: IoT (Emission Monitoring System)

Advances in Materials Science and Engineering

Retraction (1 page), Article ID 9828361, Volume 2024 (2024)

Retracted: Response Surface Methodology Approach to Predict the Flexural Moment of Ferrocement Composites with Weld Mesh and Steel Slag as Partial Replacement for Fine Aggregate

Advances in Materials Science and Engineering

Retraction (1 page), Article ID 9805723, Volume 2024 (2024)

Retracted: Dynamic Analysis and Fabrication of Single Screw Conveyor Machine

Advances in Materials Science and Engineering




Retraction (1 page), Article ID 9812754, Volume 2023 (2023)

Retracted: Optimization of Water Absorption and Mechanical and Thermal Behavior of Polylactic Acid/Chitosan/Titanium Carbide

Advances in Materials Science and Engineering




Retraction (1 page), Article ID 9802670, Volume 2023 (2023)

[Retracted] Optimization of Water Absorption and Mechanical and Thermal Behavior of Polylactic Acid/Chitosan/Titanium Carbide

S. Krishnamohan , Harishchander Anandaram, V. Rathinam, S. Kaliappan, S. Sekar, Pravin P Patil, Asheesh Kumar , and Venkatesan Govindaraajan 


Research Article (8 pages), Article ID 5176584, Volume 2022 (2022)

[Retracted] Influences of Aqueous Nanofluid Emulsion on Diesel Engine Performance, Combustion, and Emission: IoT (Emission Monitoring System)

B. Venkatesh , J. Chinna Babu , Sandeep Kumar Mathivanan, Prabhu Jayagopal, S. Prasanna, and Md Salah Uddin 









Research Article (9 pages), Article ID 8470743, Volume 2022 (2022)

[Retracted] Response Surface Methodology Approach to Predict the Flexural Moment of Ferrocement Composites with Weld Mesh and Steel Slag as Partial Replacement for Fine Aggregate

Jayaprakash Sridhar, Ganesh Bhausaheb Shinde, D Vivek, Khalida Naseem, Piyush Gaur, Pravin P Patil, and Misganaw Tesfaye Tesema 


Research Article (9 pages), Article ID 9179480, Volume 2022 (2022)

Influence of Planetary Ball Mill Parameters on Powder Flowability of AlSi10Mg with Niobium Carbide Using Central Composite Design (CCD)

Raj Mohan R , Venkatraman R , Raghuraman S , Manoj Kumar P , Rajneesh Sharma , Ankit , Atul Sarojwal , and Rajkumar S 

Research Article (11 pages), Article ID 2869225, Volume 2022 (2022)

[Retracted] Dynamic Analysis and Fabrication of Single Screw Conveyor Machine

Sundarraaj Moorthi, Meikandan Megaraj, Lenin Nagarajan, Alagar Karthick, Murugesan Bharani , and Pravin P. Patil

Research Article (10 pages), Article ID 3843968, Volume 2022 (2022)

Retraction

Retracted: Influences of Aqueous Nanofluid Emulsion on Diesel Engine Performance, Combustion, and Emission: IoT (Emission Monitoring System)

Advances in Materials Science and Engineering

Received 8 January 2024; Accepted 8 January 2024; Published 9 January 2024

Copyright © 2024 Advances in Materials Science and Engineering. This is an open access article distributed under the Creative Commons Attribution License, which permits unrestricted use, distribution, and reproduction in any medium, provided the original work is properly cited.

This article has been retracted by Hindawi following an investigation undertaken by the publisher [1]. This investigation has uncovered evidence of one or more of the following indicators of systematic manipulation of the publication process:

- (1) Discrepancies in scope
- (2) Discrepancies in the description of the research reported
- (3) Discrepancies between the availability of data and the research described
- (4) Inappropriate citations
- (5) Incoherent, meaningless and/or irrelevant content included in the article
- (6) Manipulated or compromised peer review

The presence of these indicators undermines our confidence in the integrity of the article's content and we cannot, therefore, vouch for its reliability. Please note that this notice is intended solely to alert readers that the content of this article is unreliable. We have not investigated whether authors were aware of or involved in the systematic manipulation of the publication process.

Wiley and Hindawi regrets that the usual quality checks did not identify these issues before publication and have since put additional measures in place to safeguard research integrity.

We wish to credit our own Research Integrity and Research Publishing teams and anonymous and named external researchers and research integrity experts for contributing to this investigation.

The corresponding author, as the representative of all authors, has been given the opportunity to register their agreement or disagreement to this retraction. We have kept a record of any response received.

References

- [1] B. Venkatesh, J. C. Babu, S. K. Mathivanan, P. Jayagopal, S. Prasanna, and M. S. Uddin, "Influences of Aqueous Nanofluid Emulsion on Diesel Engine Performance, Combustion, and Emission: IoT (Emission Monitoring System)," *Advances in Materials Science and Engineering*, vol. 2022, Article ID 8470743, 9 pages, 2022.

Retraction

Retracted: Response Surface Methodology Approach to Predict the Flexural Moment of Ferrocement Composites with Weld Mesh and Steel Slag as Partial Replacement for Fine Aggregate

Advances in Materials Science and Engineering

Received 8 January 2024; Accepted 8 January 2024; Published 9 January 2024

Copyright © 2024 Advances in Materials Science and Engineering. This is an open access article distributed under the Creative Commons Attribution License, which permits unrestricted use, distribution, and reproduction in any medium, provided the original work is properly cited.

This article has been retracted by Hindawi following an investigation undertaken by the publisher [1]. This investigation has uncovered evidence of one or more of the following indicators of systematic manipulation of the publication process:

- (1) Discrepancies in scope
- (2) Discrepancies in the description of the research reported
- (3) Discrepancies between the availability of data and the research described
- (4) Inappropriate citations
- (5) Incoherent, meaningless and/or irrelevant content included in the article
- (6) Manipulated or compromised peer review

The presence of these indicators undermines our confidence in the integrity of the article's content and we cannot, therefore, vouch for its reliability. Please note that this notice is intended solely to alert readers that the content of this article is unreliable. We have not investigated whether authors were aware of or involved in the systematic manipulation of the publication process.

Wiley and Hindawi regrets that the usual quality checks did not identify these issues before publication and have since put additional measures in place to safeguard research integrity.

We wish to credit our own Research Integrity and Research Publishing teams and anonymous and named external researchers and research integrity experts for contributing to this investigation.

The corresponding author, as the representative of all authors, has been given the opportunity to register their agreement or disagreement to this retraction. We have kept a record of any response received.

References

- [1] J. Sridhar, G. B. Shinde, D. Vivek et al., "Response Surface Methodology Approach to Predict the Flexural Moment of Ferrocement Composites with Weld Mesh and Steel Slag as Partial Replacement for Fine Aggregate," *Advances in Materials Science and Engineering*, vol. 2022, Article ID 9179480, 9 pages, 2022.

Retraction

Retracted: Dynamic Analysis and Fabrication of Single Screw Conveyor Machine

Advances in Materials Science and Engineering

Received 11 July 2023; Accepted 11 July 2023; Published 12 July 2023

Copyright © 2023 Advances in Materials Science and Engineering. This is an open access article distributed under the Creative Commons Attribution License, which permits unrestricted use, distribution, and reproduction in any medium, provided the original work is properly cited.

This article has been retracted by Hindawi following an investigation undertaken by the publisher [1]. This investigation has uncovered evidence of one or more of the following indicators of systematic manipulation of the publication process:

- (1) Discrepancies in scope
- (2) Discrepancies in the description of the research reported
- (3) Discrepancies between the availability of data and the research described
- (4) Inappropriate citations
- (5) Incoherent, meaningless and/or irrelevant content included in the article
- (6) Peer-review manipulation

The presence of these indicators undermines our confidence in the integrity of the article's content and we cannot, therefore, vouch for its reliability. Please note that this notice is intended solely to alert readers that the content of this article is unreliable. We have not investigated whether authors were aware of or involved in the systematic manipulation of the publication process.

Wiley and Hindawi regrets that the usual quality checks did not identify these issues before publication and have since put additional measures in place to safeguard research integrity.

We wish to credit our own Research Integrity and Research Publishing teams and anonymous and named external researchers and research integrity experts for contributing to this investigation.

The corresponding author, as the representative of all authors, has been given the opportunity to register their agreement or disagreement to this retraction. We have kept a record of any response received.

References

- [1] S. Moorthi, M. Megaraj, L. Nagarajan, A. Karthick, M. Bharani, and P. P. Patil, "Dynamic Analysis and Fabrication of Single Screw Conveyor Machine," *Advances in Materials Science and Engineering*, vol. 2022, Article ID 3843968, 10 pages, 2022.

Retraction

Retracted: Optimization of Water Absorption and Mechanical and Thermal Behavior of Polylactic Acid/Chitosan/Titanium Carbide

Advances in Materials Science and Engineering

Received 11 July 2023; Accepted 11 July 2023; Published 12 July 2023

Copyright © 2023 Advances in Materials Science and Engineering. This is an open access article distributed under the Creative Commons Attribution License, which permits unrestricted use, distribution, and reproduction in any medium, provided the original work is properly cited.

This article has been retracted by Hindawi following an investigation undertaken by the publisher [1]. This investigation has uncovered evidence of one or more of the following indicators of systematic manipulation of the publication process:

- (1) Discrepancies in scope
- (2) Discrepancies in the description of the research reported
- (3) Discrepancies between the availability of data and the research described
- (4) Inappropriate citations
- (5) Incoherent, meaningless and/or irrelevant content included in the article
- (6) Peer-review manipulation

The presence of these indicators undermines our confidence in the integrity of the article's content and we cannot, therefore, vouch for its reliability. Please note that this notice is intended solely to alert readers that the content of this article is unreliable. We have not investigated whether authors were aware of or involved in the systematic manipulation of the publication process.

Wiley and Hindawi regrets that the usual quality checks did not identify these issues before publication and have since put additional measures in place to safeguard research integrity.

We wish to credit our own Research Integrity and Research Publishing teams and anonymous and named external researchers and research integrity experts for contributing to this investigation.

The corresponding author, as the representative of all authors, has been given the opportunity to register their agreement or disagreement to this retraction. We have kept a record of any response received.

References

- [1] S. Krishnamohan, H. Anandaram, V. Rathinam et al., "Optimization of Water Absorption and Mechanical and Thermal Behavior of Polylactic Acid/Chitosan/Titanium Carbide," *Advances in Materials Science and Engineering*, vol. 2022, Article ID 5176584, 8 pages, 2022.

Retraction

Retracted: Optimization of Water Absorption and Mechanical and Thermal Behavior of Polylactic Acid/Chitosan/Titanium Carbide

Advances in Materials Science and Engineering

Received 11 July 2023; Accepted 11 July 2023; Published 12 July 2023

Copyright © 2023 Advances in Materials Science and Engineering. This is an open access article distributed under the Creative Commons Attribution License, which permits unrestricted use, distribution, and reproduction in any medium, provided the original work is properly cited.

This article has been retracted by Hindawi following an investigation undertaken by the publisher [1]. This investigation has uncovered evidence of one or more of the following indicators of systematic manipulation of the publication process:

- (1) Discrepancies in scope
- (2) Discrepancies in the description of the research reported
- (3) Discrepancies between the availability of data and the research described
- (4) Inappropriate citations
- (5) Incoherent, meaningless and/or irrelevant content included in the article
- (6) Peer-review manipulation

The presence of these indicators undermines our confidence in the integrity of the article's content and we cannot, therefore, vouch for its reliability. Please note that this notice is intended solely to alert readers that the content of this article is unreliable. We have not investigated whether authors were aware of or involved in the systematic manipulation of the publication process.

Wiley and Hindawi regrets that the usual quality checks did not identify these issues before publication and have since put additional measures in place to safeguard research integrity.

We wish to credit our own Research Integrity and Research Publishing teams and anonymous and named external researchers and research integrity experts for contributing to this investigation.

The corresponding author, as the representative of all authors, has been given the opportunity to register their agreement or disagreement to this retraction. We have kept a record of any response received.

References

- [1] S. Krishnamohan, H. Anandaram, V. Rathinam et al., "Optimization of Water Absorption and Mechanical and Thermal Behavior of Polylactic Acid/Chitosan/Titanium Carbide," *Advances in Materials Science and Engineering*, vol. 2022, Article ID 5176584, 8 pages, 2022.

Research Article

Optimization of Water Absorption and Mechanical and Thermal Behavior of Polylactic Acid/Chitosan/Titanium Carbide

S. Krishnamohan ¹, Harishchander Anandaram,² V. Rathinam,³ S. Kaliappan,⁴ S. Sekar,⁵ Pravin P Patil,⁶ Asheesh Kumar ⁷, and Venkatesan Govindaraajan ⁸

¹Department of Mechanical Engineering, E.G.S. Pillay Engineering College, Nagapattinam, Tamil Nadu, India

²Centre for Computational Engineering and Networking (CEN), Amrita Vishwa Vidyapeetham, Coimbatore, Tamil Nadu, India

³Automobile Engineering Department, VNR Vignana Jyothi Institute of Engineering and Technology, Hyderabad, Telangana, India

⁴Department of Mechanical Engineering, Velammal Institute of Technology, Chennai, Tamil Nadu, India

⁵Department of Mechanical Engineering, Rajalakshmi Engineering College, Rajalakshmi Nagar, Thandalam, Chennai, India

⁶Department of Mechanical Engineering, Graphic Era Deemed to Be University, Bell Road, Clement Town, Dehradun, Uttarakhand, India

⁷Mechanical Engineering Department, Mahatma Gandhi Institute of Technology, Hyderabad, Telangana, India

⁸Department of Mechanical Engineering, Haramaya Institute of Technology, Haramaya University, Dire Dawa, Ethiopia

Correspondence should be addressed to Venkatesan Govindaraajan; venkatesanggg2011@gmail.com

Received 3 April 2022; Revised 14 July 2022; Accepted 25 July 2022; Published 8 October 2022

Academic Editor: Penchal Reddy

Copyright © 2022 S. Krishnamohan et al. This is an open access article distributed under the Creative Commons Attribution License, which permits unrestricted use, distribution, and reproduction in any medium, provided the original work is properly cited.

Nanocomposites are being studied for their mechanical, thermal, and water absorption capabilities. Polylactic acid/chitosan blends have been studied extensively for their physical, mechanical, and morphological properties. Although the three materials have been blended, no research has been done on the mechanical or morphological properties of PLA/CS/TiC NPs. PLA/CS bonding is quite deprived, and thus researchers are trying to improve it by introducing TiC NPs; this would improve the composites' overall quality (mechanical and thermal characteristics as well as water absorption) by increasing the strength of the bond between the two materials. The impacts of TiC NPs on PLA/CS properties are studied using FTIR and XRD and thermal (TGA) and mechanical investigations. Titanium carbide nanoparticles in the polylactic acid/chitosan matrix increase the mechanical characteristics of the materials. As an outcome, the TiC content in the sample rises to 4 wt % even though adding TiC NPs increased the mechanical properties by up to 2%. The findings of this study might be applied to the development of environmentally friendly casings.

1. Introduction

Renewable bio-sourced components have become more popular in recent years as a replacement for petroleum-based goods [1]. To put it another way, a biomaterial is anything that may be utilized for a long length of time to cure, enhance, or replace an organ or tissue in the body [2, 3]. A number of advantages of bio-composite materials include the capacity for scientists and engineers to alter the

qualities of the material. Chitosan (CS) is a bio-based polymer that has no genuine petrochemical equivalent since its inherent qualities are so unique and important. Thus, the fundamental properties of CS allow it to be used for its own sake. Biopolymers such as chitosan, a commercially available polymer, have been proven to be useful in the immobilization of certain biomolecules [4]. Hydrogels, films, fibers, and sponges can also be made with CS. However, the CS material's stability is often poorer [5] due to its hydrophilic

nature, particularly its susceptibility to pH. The introduction of inorganic particles into CS has proven effective in controlling its mechanical and chemical characteristics [6]. Owing to its biodegradability and excellent mechanical qualities, PLA is a widely accessible, economically viable, and environmentally acceptable polymer. Polylactic acid is a biodegradable, non-toxic, and biocompatible substance that may be utilized in a variety of applications [7]. As a result, mugs and teabags may be made from CS because it is renewable, non-toxic, edible, and biodegradable. It may be used to carry food, treat wounds, and more. CS's water sensitivity can be modified by mixing it in alternative biodegradable polymers, such as poly(-caprolactone) and PLC [8]. The hydrophobic characteristics of PLA make it an appealing alternative for improving the stability of CS. Titanium carbide, a metal oxide, can be added to the composite to fix the problem [9]. As a well-known and widely used ecologically friendly and multifunctional inorganic additive, titanium carbide nanoparticles (TiC NPs) might be viewed as a nanofiller for different polymeric substances, giving features including sterile action or intense UV absorption [10]. Research on the morphological and mechanical aspects of PLA/CS mixtures has been conducted extensively. However, no one study has focused on the mechanical characteristics and morphological characterization of PLA/CS/TiC NP blends [11, 12]. Direct precipitation is employed to create TiC NPs, which are then utilized to create polylactic acid, chitosan, and titanium carbide nanoparticle compounds by mixing the solution and casting with solvents. It is widely used because of its wide range of qualities and uses [13, 14]. Titanium carbide (TiC) rubber vulcanization is a process in which the rubber reacts to generate mechanisms that enhance the quality of the goods. In order to activate the cure, stearic acid was combined with TiC, which also increases flex fatigue and ageing resistance. Because of this, TiC NPs are frequently referred to be "non-toxic." A study by Li et al. [15] found that zinc nitrate (TiC) NPs were hazardous to *E. coli*, *Staphylococcus aureus*, and primary human immune cells. Identical particles have had little effect on the viability of primary human T cells at attentions bactericidal to both gramme positive and negative pathogens, despite TiC NPs' shown ability to suppress growth [16, 17]. Toxic properties of TiC NPs have been established for certain bacteria, which opens the door to potential biological and antibacterial uses. According on its intended purpose, titanium carbide (TiC) NPs can either be regarded an industrial chemical or a specialized semiconductor. As an instance, its high refractile index (1.96–2.12) makes it ideal for pigment applications. It is also possible to employ the "active" grades in chemical plant desulfurization operations because of their high specific surface area [18]. The controlled precipitation/sol-gel approach is utilized to synthesize TiC NPs in this research because it provides a reproducible result. The sol-gel technique is favoured due to its ease of use, low cost, reliability, repeatability, and very mild synthesis conditions that let to modify the surface of TiC with certain organic molecules. It may be employed in a variety of ways because of its ability to modify its features [19]. A reducing agent is used to quickly and spontaneously

reduce a zinc salt solution in order to limit the formation of particles of a particular size and then a precursor of titanium carbide is precipitated from the solution [20, 21]. Next, the precursor is heated and milled to eliminate any remaining impurities. pH, temperature, and precipitation time are all factors that influence the precipitation process [22, 23]. The literature survey revealed that tons of work were performed on the PLA but despite the fact that the three materials have been combined, no study on the mechanical or morphological characteristics of PLA/CS/TiC NPs has been done. PLA/CS bonding is lacking, and thus an attempt was made to increase it by including TiC NPs. This would improve the overall quality of the composites by boosting the strength of the bind between the two materials.

2. Materials and Methods

Polymer composites are made using the generated TiC NPs. Next, the compatibility and characteristics of the produced TiC NPs and the generated polymer compounds are evaluated. There is a complete list of the TiC NP and compound characterization tools, as well as the chemicals and procedures used to manufacture them in this section. Experiments were conducted using substance grade chemicals. Melt flow index (MFI) is 15 grams per minute at 190°C with specific gravity of 1.24 grams per cubic centimeter (2.16 Kg). As a reinforcing filler, this study makes use of practical grade 75% DD chitosan (CS) from Sigma Aldrich. As part of the synthesis process, water that has been deionized is used as shown in Figure 1.

2.1. Preparation of Pure PLA, PLA/Chitosan, and Polylactic Acid/Chitosan/Titanium Carbide NP Composites. To create a pure PLA composite film, chloroform is used to dissolve PLA pellets at 600°C in a water bath. Afterwards, the polylactic acid solution is kept at ambient temperature for 24 hours to let the solvent drain. The poured solution has a 100 m thickness. Next, the film is pulled away from the molding surface and removed. Chloroform solution is used to combine 10% PLA pellets with 5% CS in order to create the PLA/CS blend composite. There are no pellets left after the solution is agitated in a water soaked at 60°F for an hour. It is then dispensed into a Petri plate and kept at room temperature for 24 hours so that the solvent may evaporate. Afterwards, the casted solution has a thickness of around 100 μm. The film is then removed from the molding substance. The TiC NPs (1, 2, and 3wt %) are dissolved in chloroform with PLA pellets (10wt %) and CS (5wt %) to create composite materials comprising polylactic acid, chitosan, and titanium carbide nanoparticles. There are no pellets left after the result is agitated in a water bath at 60°F for an hour. Finally, a Petri plate is used to cast the solution of polylactic acid, chitosan, and titanium carbide nanoparticles, which is allowed to dry. A dial thickness gauge, model 7301, was used to measure the film thickness. Measurements of thickness were made at several sites. The depth of all blended flicks was discovered to be about 0.10 mm [24]. After that, the casting



FIGURE 1: Synthesis of poly(lactic acid)/chitosan/titanium carbide nanoparticles.

surface is scraped clean of them. Mechanical, thermal, and morphological aspects of composites are also investigated.

2.2. Physical-Chemical Description

2.2.1. X-Ray Diffraction (XRD). The 6000 X-ray machine manufactured by GE was utilized with Ni clean $\text{CuK}\alpha$ ($\lambda = 1.542\text{\AA}$) energy to investigate the TiC NP's structural features. Nanoparticle crystallite sizes were calculated using Scherrer's relation.

The following calculation was employed to evaluate the crystallinity to amorphous ratio of various materials.

$$\% \text{ Crystallinity} = \left[\frac{I_{\max} - I_{\min}}{I_{\max}} \right] \times 100, \quad (1)$$

where D is the crystalline size (nm), λ is the wavelength of X-ray ($\lambda = 1.542\text{\AA}$), β is the full width at half maximum (FWHM-in radian) intensity, and θ is the Bragg diffraction angle ($^\circ$).

The XRD analysis scans at a rate of 2°Cmin^{-1} at an angle of $20 - 80^\circ \text{C}$ in 2θ ranges.

2.2.2. FTIR. A 1725 X spectrometer is utilized for FTIR spectroscopy. Pellets are formed by distributing, mixing, and rolling a TiC NP/KBr combination. The spectral range of TiC NPs is $4000 - 280 \text{ cm}^{-1}$. Compound spectrum varied from 4000 cm^{-1} to 400 cm^{-1} for the tested materials.

2.3. Mechanical Test. Tensile characteristics of pure PLA and mixed composite films are evaluated in accordance with ASTM D882, which calls for a UTM with a load volume of 10 kN. The strain rate was 10 mm/min at atmosphere temperature, and the findings were averaged over four experiments.

2.4. Thermogravimetric Analysis (TGA). The thermal stabilization of the specimen is evaluated by TGA and a heating range of 10°C/min in nitrogen atmosphere. Analyzing around 2 mg of each specimen is used to determine the sample's weight loss.

2.5. Water Absorption. For each distinct composite, spherical specimens with a diameter of 6 mm are manufactured in compliance with ASTM D570. In a desiccator,

the specimens are preserved by drying for one hour at 60°C and then cooled. After cooling, the samples are weighed and left in deionized water for 24 hours before being analyzed. The specimens are taken out, patted dry, and weighed once they have been removed. Ten days after the specimens were weighed, they were returned to the water and weighed again. (2) shows the method for calculating water absorption, which is given as a weight gain as a percentage.

$$\text{Water absorption (\%)} = \frac{(W_2 - W_1)}{W_1 \times 100\%}, \quad (2)$$

where W_1 is the dry weight of the sample and W_2 is the wet weight of the sample.

The findings of this test are based on an average of five different test specimens.

3. Results and Discussion

3.1. Description of TiC Nanoparticles

3.1.1. XRD. TiC in its pure hexagonal phase has lattice factors $a = 3.2568$ and $c = 5.2125$, which may be used to determine the source of all these reflections. TiC powder sample's standard value and the intensity values observed in Figure 2 are quite close to each other. It is easy to see that TiC nanoparticles have great crystallinity because of their sharp peaks. The crystallite size is determined by using the plane. According to Scherrer's relation, the crystallinity of the produced TiC NPs is about 87%.

3.1.2. FTIR. Titanium carbide nanoparticles that were made in the range were $400 \text{ cm}^{-1} - 4000 \text{ cm}^{-1}$ analysed using Fourier transfer infrared spectroscopy. The group at 3379.54 cm^{-1} is caused by stretching atmospheres of the O-H group in water, liquors, and hydroxybenzenes. Remains of zinc acetate may be responsible for an absorption peak at 1560.89 cm^{-1} that is associated with C=O group carboxylic derivatives. According to [25], the carboxylate group stretching vibrations at 1410.6 cm^{-1} were detected. Ti tetrahedral coordination is responsible for the absorption at $838.20, \text{ cm}^{-1}$. The E2 method of hexagonal TiC was discovered to have a large ring of absorption at 366.72 cm^{-1} (Raman active). Other TiC NP researchers have reported a similar outcome.

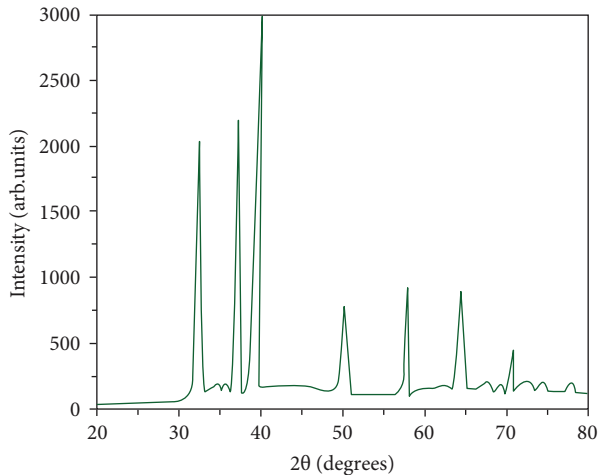


FIGURE 2: XRD image of room-temperature TiC NPs.

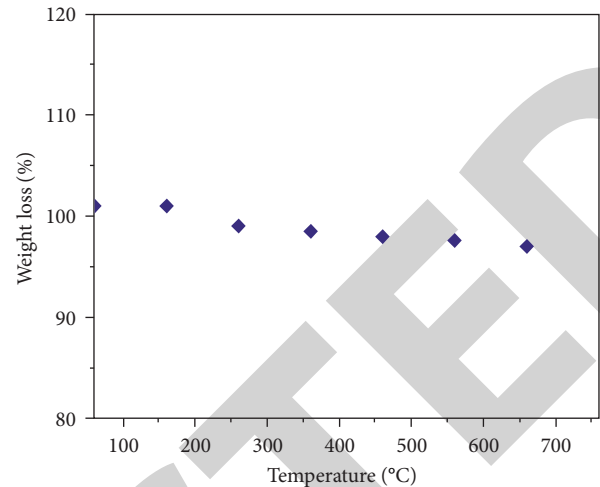


FIGURE 3: TGA of TiC NPs.

3.1.3. *TGA*. Images of the thermogram and its derivatives of titanium carbide nanoparticles are displayed in Figures 3 and 4. Thermal breakdown of TiC NPs was shown to occur in a single step by the results shown in Figure 3. While heating from 175°C to 211°C, there was a little loss of TG weight (2%). The water that was physically absorbed by the body is to blame for this small weight reduction. For up to 700°C, there is no more weight loss to be seen in the subjects. This showed that the breakdown product at 211°C completed the production of TiC nanocrystalline.

3.2. Description of PLA, PLA/Chitosan, and PLA/Chitosan/TiC Materials

3.2.1. *FTIR*. The polymer phase behavior and intermolecular interactions are studied using FTIR. In this work, the FTIR spectroscopy is used to explore the polylactic acid, chitosan, and TiC NPs interactions, as shown in Figure 5. On the other hand, PLA/CS is shown in Figure 6 to demonstrate the difference between the PLA/CS FTIR spectrum and the FTIR spectrum with 2, 3, and 4wt % TiC NP loading. As displayed in Figure 5, the typical absorption groups represented in the figure are those of OH twisting/elongating, CH unequal stretching vibration, and C=O stretching vibration. There was also an absorption group at 1450.89 cm^{-1} in PLA's FTIR spectra, which corresponded to the CH stretching in CH_3 . But in contrast to this, the polylactic acid or chitosan materials in Figure 5 revealed distinctive absorption groups at 3511.62 cm^{-1} and 2986.32 cm^{-1} , which are owing to higher wave number stretching vibrations of the OH and CH after the insertion of CS. This change showed the presence of PLA/CS composites that had interacted. The band intensity at 2978.25 cm^{-1} and 1749.72 cm^{-1} was likewise reduced by the addition of chitosan.

It is possible that the PLA/CS composite was formed by the diffusion of CS inside PLA. Figure 6 shows the FTIR spectrum of polylactic acid, chitosan, and (2 wt %) titanium carbide nanoparticles. When titanium carbide nanoparticles are additional to the mixture, the characteristic absorption groups at 3506.52 cm^{-1} , 2979.77 cm^{-1} , and 1748.82 cm^{-1} ,

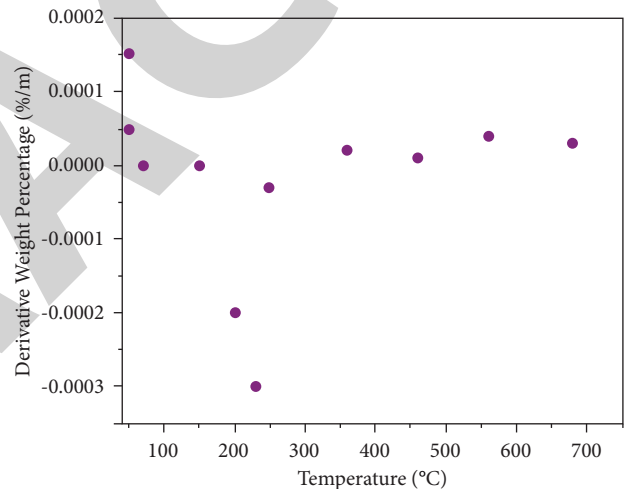


FIGURE 4: DTG of TiC NPs.

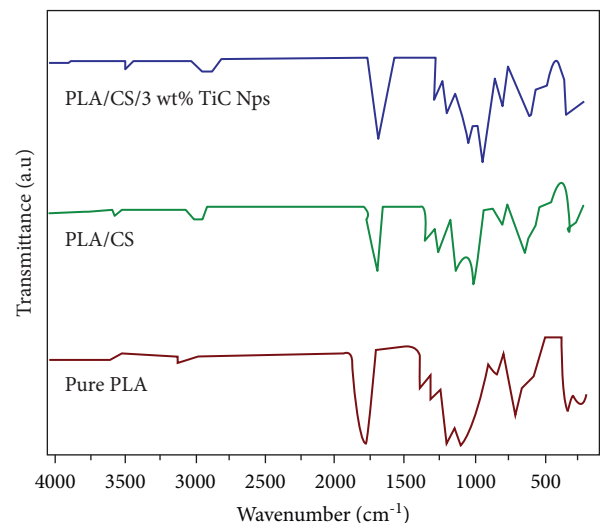


FIGURE 5: FTIR spectrum.

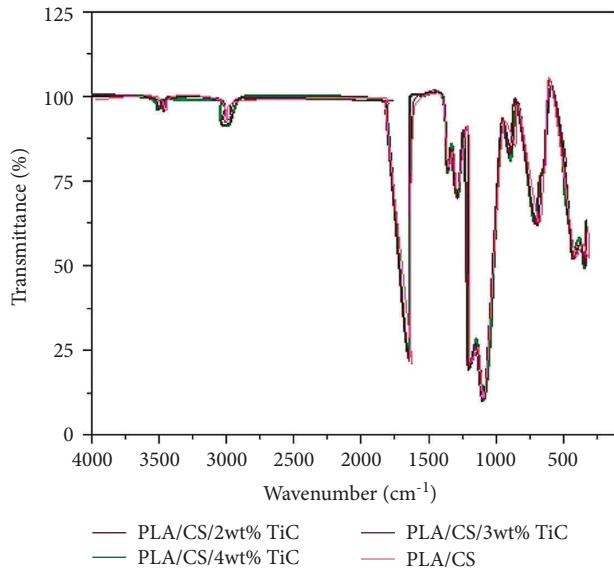


FIGURE 6: (a) Tensile strength, (b) tensile modulus, and (c) elongation at break of different composites.

which are induced by OH stretching and bending, CH irregular stretching, and C=O elongating vibrations, are pushed toward less wave numbers. Some interactions with a surface resulted in PLA/CS/TiC NP composites. Compared to polylactic acid or chitosan materials, the intensity of the 2979.77 cm^{-1} and 1748.82 cm^{-1} bands improved as well. This shows that strong intercomponent interactions and superior distribution have affected the polymeric chain organization which is then imitated in the peak intensity.

For PLA/CS/TiC NPs, the FTIR peak intensity coincided with the intensity at its highest point of the polylactic acid and chitosan compounds as shown in Figure 5. TiC nanoparticles in PLA/CS/2 wt % composites enhanced the peak intensity of the FTIR spectrum. There are no PLA or PLA/CS composite spectra in Figure 7 to compare to the polylactic acid/chitosan and pure polylactic acid/chitosan spectra.

3.2.2. Mechanical Test. These composites' elongational break, tensile strength, and tensile modulus all depend on the optimal distribution and intercomponent interaction of polylactic acid, chitosan, and titanium carbide nanoparticles. Polymer matrix-filler interactions are said to improve mechanical and thermodynamic characteristics of composites when highly compatible filler is dispersed in a homogeneous manner. Tensile and modulus properties of pure PLA material deteriorated when carbon fibers were added. Polylactic acid and chitosan materials with TiC nanoparticles demonstrated a rise in tensile strength and tensile modulus up to specific loading amounts of TiC NPs. Polylactic acid, chitosan, and titanium carbide nanoparticle compounds' elongation at break increased steadily up to 3wt titanium carbide nanoparticle loading.

Figure 8 depicts a typical reaction to stress curve for PLA/CS compounds loaded with 2 wt % TiC NPs. In order to determine strength of the compound materials, the ability of

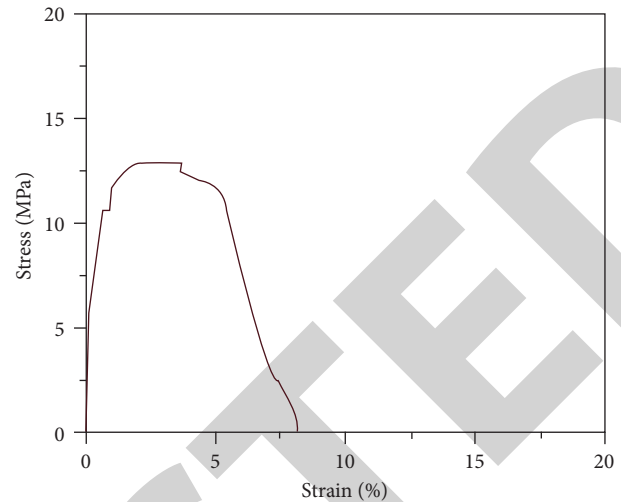


FIGURE 7: FTIR spectrum of different composites.

strengthening to transmit stress effectively between the matrix and filler is critical. The TiC nanoparticles are also a nano reinforcement, allowing the matrix and filler to transmit strain more easily. As indicated in Figure 6(a), the tensile properties of PLA/CS materials were less than those of pure polylactic acid composites. PLA and chitosan created hydrogen bonds between PLA's C=O body molecules and NH₃ molecules. The tensile strength of the PLA/CS material is a product of chitosan.

Polylactic acid/chitosan's tensile strength reduced as the PLA/CS ratio increased; this might be because intramolecular hydrogen bonds formed instead of intermolecular hydrogen bonds, causing phase separation between the two major components.

Titanium carbide nanoparticle incorporation into PLA/CS composite outcome is higher in tensile strength of 34% to 46% at a loading of 2wt%. However, increasing the TiC NP content to 4 weight % decreased the composite's tensile strength.

According to Figure 6(b), when pure PLA was combined with carbon steel, it lost 14% in its modulus of tensile deformation. Incorporating titanium carbide nanoparticles into the PLA/CS materials resulted in a dramatic increase in tensile strength. PLA/CS/3 wt% TiC NP composite's modulus reduced. At 2wt % polylactic acid/CS/TiC NP compounds, elongation at break was consistently enhanced in Figure 6(c). Elongation at break of polylactic acid/chitosan/3wt% titanium carbide nanoparticle material was reduced considerably. Ring structures in the CS and PLA are to blame for this.

As a result, the intermolecular hydrogen connections among polylactic acid, chitosan, and titanium carbide nanoparticles weaken, creating it simpler for the molecular chain to rotate or move. Because of this, the composites' tensile strength, tensile modulus, and elongational break are considerably improved. TiC NPs, however, must be included into the polylactic acid and CS matrix in the correct proportion to improve its mechanical characteristics, since excess TiC NPs caused the composite to become brittle.

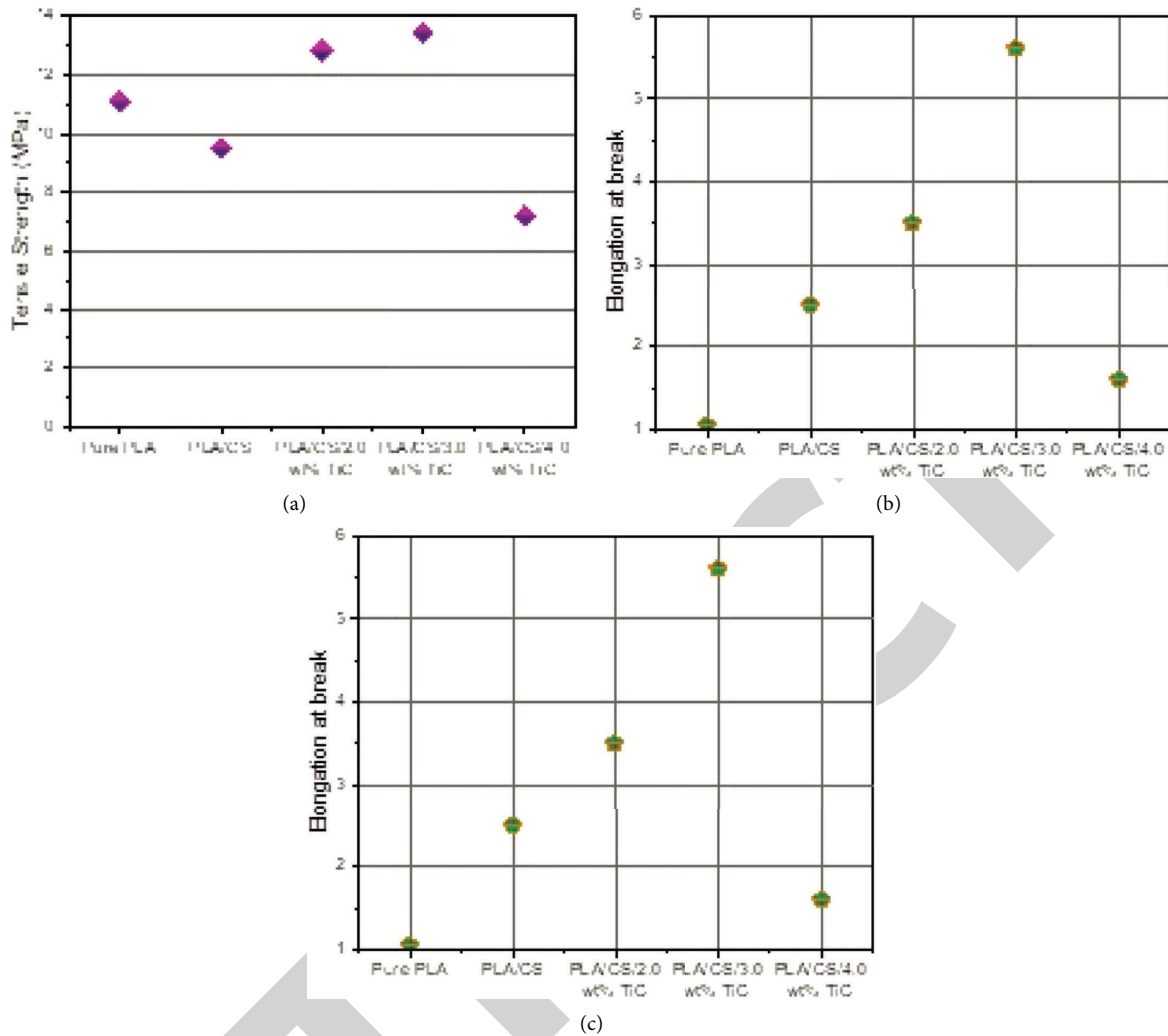


FIGURE 8: Typical stress-strain curve for pure polylactic acid/chitosan composite.

3.2.3. TGA. As can be seen in Table 1, various composites have varying melting points, maximum degradation temperatures, and breakdown percentages. Figures 9 and 10 display derivative thermogram of a variety of composite materials.

Pure PLA composite began thermal degradation at 279.8°C with a decomposition percentage of 89.7%. In contrast with the pure polylactic acid composite, PLA/chitosan composite has better thermal stability with thermal disintegration starting at 265.9°C and a decomposition percentage of 101.6%. For one thing, the thermal breakdown temperature is reduced by 12–17 % once the TiC NPs are included in the PLA/CS matrix. Thermal breakdown temperature of the polylactic acid/chitosan/3wt % titanium carbide nanoparticle material is somewhat higher than the 2 and 3wt% TiC loading, despite the reduced thermal stability of the polylactic acid/chitosan/titanium carbide nanoparticle compounds. This shows that adding more TiC NPs to the polylactic acid/chitosan/titanium carbide nanoparticle materials improves its thermal stability.

3.2.4. Water Absorption. In Figure 11, the composites' water absorption patterns are clearly defined. As varying amounts of water are absorbed by the composites, the samples' water absorption increases and falls unevenly during the test. Figure 11 shows that the water absorption content of pure PLA film ranged from 0% to 0.02% during the course of the 10 days of testing. Using PLA as a hydrophobic component was validated by the results of the test, which showed that it was water resistant enough. Modification of PLA hydrophobicity (e.g., plasma treatment) can be used to improve their compatibility.

However, PLA/chitosan material demonstrated an increase in absorption of liquids 0.04 to 0.06% after blending with CS. The reason for this is because CS was extremely sensitive to dampness. Pure CS film's water sensitivity was lowered by including PLA in an earlier experiment. Over the course of the 10-day test period, the water absorption % of polylactic acid/chitosan composite films including TiC NPs with varying TiC NP compositions (2, 3, and 4 wt %) varied. The polylactic acid/chitosan/2 wt %titanium carbide NP blend composite presented a greater increase in water

TABLE 1: Onset temperature, maximal temperature, and % of decomposition of different composites.

Composites	Onset temperature (°C)	Maximal degradation temperature, T_{max}	% of decomposition
Polylactic acid	279.9	363.6	89
Polylactic acid/CS	266.8	366.2	102.6
Polylactic acid/CS/2 wt% TiC NPs	218.6	287.3	80
PLA/CS/3 wt% TiC NPs	208.1	281.2	85.3
PLA/CS/4 wt% TiCNPs	234.5	278.3	712.8

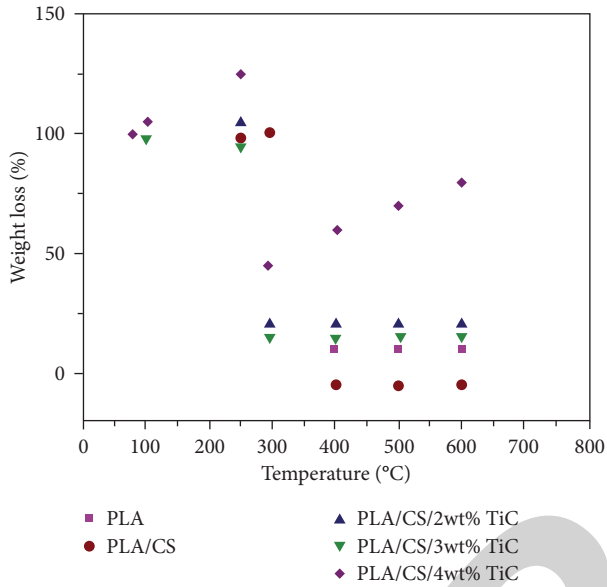


FIGURE 9: TGA thermograms of various composites.

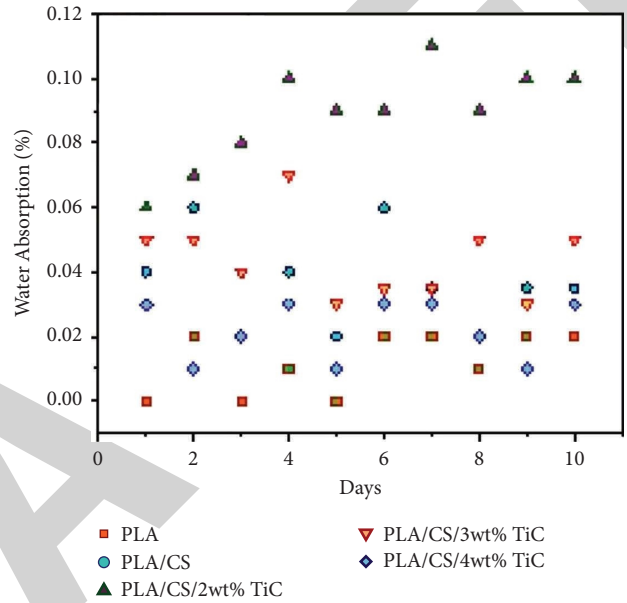


FIGURE 11: Water absorption behavior for various TiC NP loadings.

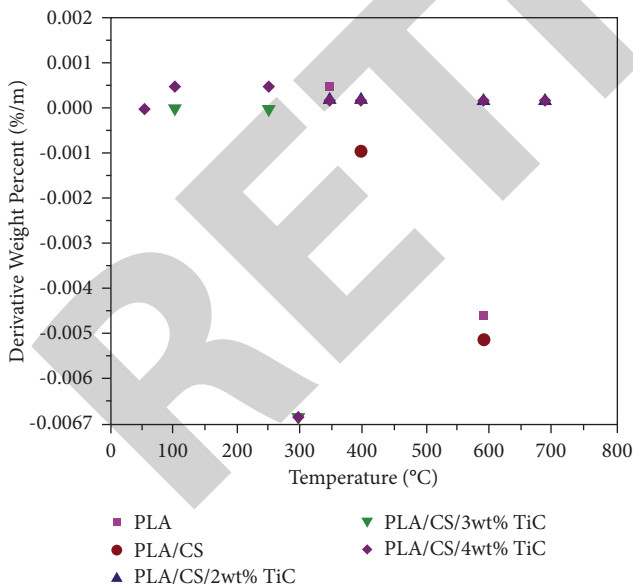


FIGURE 10: DTG thermograms of different composites.

absorption content than the polylactic acid/CS composite, with a range of 0.06 to 0.11%. PLA/CS with 2 weight % TiC NPs had poor water barrier characteristics, as revealed by this finding. Comparing the polylactic acid/chitosan/2 wt % titanium carbide nanoparticle group material, there was a

decrease in water absorption content of between 0.03 and 0.05%. Titanium carbide nanoparticles were shown to enhance the water barrier qualities of polylactic acid/CS composites by adding 2% TiC NPs to the mixture. Figure 11 exhibits an even lower water absorption drop compared to the 0.01–0.03% decrease in water absorption and the increased water barrier ability of the polylactic acid/chitosan/3.0 wt % titanium carbide nanoparticle blend composite (0.01–0.03%).

As a result, it can be inferred that the water barrier capabilities of the PLA/chitosan/TiC NP materials are enhanced with increasing TiC NP loadings.

4. Conclusion

This study examines the main properties of pure polylactic acid and polylactic acid nanocomposite films. TiC NPs may be produced via direct precipitation from a solution of dihydrate and NaOH at room temperature. There are also synthesized titanium carbide nanoparticles with a middling particle size (105 nm) and thermal stability (2110°C). It is utilized to create innovative PLA/chitosan/TiC NP-based materials via solution mixing and film casting. It is evident from the FTIR spectrum that the TiC NPs were well integrated into the PLA/chitosan matrix, as shown by the outstanding attraction and interaction between the PLA and CS. These gains are attributed to better intercomponent

Retraction

Retracted: Influences of Aqueous Nanofluid Emulsion on Diesel Engine Performance, Combustion, and Emission: IoT (Emission Monitoring System)

Advances in Materials Science and Engineering

Received 8 January 2024; Accepted 8 January 2024; Published 9 January 2024

Copyright © 2024 Advances in Materials Science and Engineering. This is an open access article distributed under the Creative Commons Attribution License, which permits unrestricted use, distribution, and reproduction in any medium, provided the original work is properly cited.

This article has been retracted by Hindawi following an investigation undertaken by the publisher [1]. This investigation has uncovered evidence of one or more of the following indicators of systematic manipulation of the publication process:

- (1) Discrepancies in scope
- (2) Discrepancies in the description of the research reported
- (3) Discrepancies between the availability of data and the research described
- (4) Inappropriate citations
- (5) Incoherent, meaningless and/or irrelevant content included in the article
- (6) Manipulated or compromised peer review

The presence of these indicators undermines our confidence in the integrity of the article's content and we cannot, therefore, vouch for its reliability. Please note that this notice is intended solely to alert readers that the content of this article is unreliable. We have not investigated whether authors were aware of or involved in the systematic manipulation of the publication process.

Wiley and Hindawi regrets that the usual quality checks did not identify these issues before publication and have since put additional measures in place to safeguard research integrity.

We wish to credit our own Research Integrity and Research Publishing teams and anonymous and named external researchers and research integrity experts for contributing to this investigation.

The corresponding author, as the representative of all authors, has been given the opportunity to register their agreement or disagreement to this retraction. We have kept a record of any response received.

References

- [1] B. Venkatesh, J. C. Babu, S. K. Mathivanan, P. Jayagopal, S. Prasanna, and M. S. Uddin, "Influences of Aqueous Nanofluid Emulsion on Diesel Engine Performance, Combustion, and Emission: IoT (Emission Monitoring System)," *Advances in Materials Science and Engineering*, vol. 2022, Article ID 8470743, 9 pages, 2022.

Research Article

Influences of Aqueous Nanofluid Emulsion on Diesel Engine Performance, Combustion, and Emission: IoT (Emission Monitoring System)

B. Venkatesh ¹, **J. Chinna Babu** ², **Sandeep Kumar Mathivanan**,³ **Prabhu Jayagopal**,³ **S. Prasanna**,³ and **Md Salah Uddin** ⁴

¹Department of Mechanical Engineering, Annamacharya Institute of Technology & Sciences, Rajampet, Kadapa, Andhra Pradesh, India

²Department of Electronics and Communication Engineering, Annamacharya Institute of Technology and Sciences, Rajampet 516126, Andhra Pradesh, India

³School of Information Technology and Engineering, Vellore Institute of Technology, Vellore, Tamil Nadu, India

⁴Department of Multimedia and Creative Technology, Daffodil International University, Dhaka-1207, Bangladesh

Correspondence should be addressed to B. Venkatesh; bvenkatesh.me.aits@annamacharyagroup.org and Md Salah Uddin; jahid.mct@diu.edu.bd

Received 15 July 2022; Accepted 16 August 2022; Published 28 September 2022

Academic Editor: Adel Mohamed

Copyright © 2022 B. Venkatesh et al. This is an open access article distributed under the Creative Commons Attribution License, which permits unrestricted use, distribution, and reproduction in any medium, provided the original work is properly cited.

Pollution is the primary ecological threat to nature and it also raises the temperature of the Earth. The primary cause of air pollution is exhaust emissions from the combustion chamber. This study aims to focus on controlling emissions using an aqueous nanoemulsion method and to analyze positive vibrations for the reduction of pollutants in diesel engines. In this study 3% NWED (nano-based water emulsion diesel), 7% NWED, and 12% NWED emulsion blended diesel were mixed with Tween-20 as a solvent. In addition, this work was accomplished with a multiuser remote control system for the continuous monitoring of emissions with IoT technology applied to diesel engines. Experimental results have been measured with an IoT kit and five gas analyzers and reported that emission of oxides of nitrogen and hydrocarbons can be reduced by using a 7% NWED blend when compared with diesel. In addition, the experimental result also shows that the brake-specific fuel consumption is reduced with an improvement in thermal efficiency at 7% NWED when compared with other blends.

1. Introduction

As the rate of fossil fuel depletion is increasing daily, there is a need to fulfill the energy demand for alternative fuels [1]. Since the 1970s, the use of energy resources such as oil, gas, coal, nuclear and hydro, has increased tremendously to meet energy demand [2]. The transport, industry, non-composted, and building sectors depend mainly on petroleum fuels [3]. Combustion emissions such as CO, CO₂, HC, NO_x, and smoke are released into the atmosphere through exhaust pipes [4]. These emissions generate chemical reactions in the atmosphere, creating a greenhouse effect [5]. Controlling pollution mixture formation in diesel engines

has been the prime objective of many researchers, who have found alternative fuels that have not shown any modifications to the engine, by reducing emissions and improving engine performance [6]. Biodiesel has been studied worldwide as the dominant diesel fuel. To achieve better performance and lower pollution, researchers have selected different biodiesel feedstocks or varying engine parameters such as injecting opening pressures (IOPs), fuel injection timings, compression ratio (CR), and additives, such as diethylether and antioxidants [7]. As a result that biodiesel blends produced lower CO, HC, and smoke emissions than diesel fuel, while combustion exhaust gas temperature, CO₂, and NO_x emissions were higher [8]. Researchers based on

several studies on diesel engines using alternative fuels have claimed that NO_x emissions have increased owing to the high combustion and heat release rate inside the combustion chamber [9].

In addition, several scholars have found that additives such as nanoparticles and water emulsions in diesel offer useful performance improvements by reducing the emissions of a diesel engine. In most cases, additives such as metal oxide particles are added to the base fuels to achieve secondary atomization and improve thermal efficiency. Additionally, these particles reduce unburnt hydrocarbon and carbon monoxide emissions [10]. Graphene, carbon nanotubes, cerium oxide, manganese, nickel oxide, and other metal oxides have been studied extensively. The presence of these dissolved metal oxide nanoparticles enhances combustion by promoting cleaner combustion and reducing ignition delay. Consequently, the engine-specific consumption is reduced [11, 12].

Water and diesel are framed into emulsion mixtures by using surfactants [13, 14]. O/W, W/O, and multiple (O/W/O and W/O/W) emulsion methods are used to stabilize water and diesel [15]. W/O emulsion is a strong bonding for the stabilization of water emulsions [16]. During the combustion process, these suspended water particles absorb heat from the cylinder walls and reduce the cylinder temperature, resulting in a reduction in the oxides of nitrogen and particulate matter [17]. Water emulsion leads to a longer delay, resulting in potholed engine operation and a longer ignition delay [18, 19].

Nanoparticles and Nanofluids act as a fuel additive to enrich the combustion rate and reduce emissions [20]. The addition of a nanocatalyst to diesel fuel improves fuel oxidation and reduces the ignition delay period time [21]. The doping of nanoparticles and the thermal brake efficiency of engine performance can be improved by reducing the emissions of CO, HC, and NO_x [22]. In diesel engines, improved events in the heat transfer rate, and thermal conductivity of nano fluid and diesel blends are helpful and the blend preposition helps to form long-term stability and good dielectric property. When using nanofluids, NO_x rates increase because of the high latent heat of vaporization [23].

The Internet of Things technology is the most efficient system for continuous monitoring of emissions, but there have been many techniques and precautions implemented in order to control emissions. Internet of Things (IoT) technology is a revolutionary, wireless health monitoring tool that integrates embedded sensors, actuators, and RFID tags to improve operations, enhance daily activities, and monitor health care [24]. A wireless communication system is well suited to measure and interpret urban environmental indicators and natural resources. In the European Union, smart IoT technology is currently being used to monitor and update emission standards. Smart IoT systems continuously collect and transmit data to detect natural threats. Using web applications, it reports back to the user whether they are threats. Intelligent mobility (e.g., route stability, smart metro traffic, vehicle tracking, and Internet of vehicles), smart living (e.g., healthcare, tourism, education, buildings, and public safety), smart environment (e.g., monitoring of city

air quality, air pollution, trees, water quality, green spaces, weather, waste collection, vehicles parking emission monitoring, management, and energy efficiency), smart citizens, smart government, smart economy, and smart architecture and technologies all benefit from it [25]. IoT can be used in various applications, such as monitoring and controlling press shop assembly, weather forecasting, prediction of plant leaf diseases, and food processing units [26, 27].

The aforementioned literature concludes that a reduction of NO_x for diesel engines has different methodologies. Among that nanofluid was used as a fuel additive because very rarely implemented in the engine literature studies for the reduction of NO_x . Furthermore, this study was carried out to reduce emissions and continuously monitor the emissions with IoT as a future scope in a different way.

The main objective of this work is to focus on controlling the emissions of oxides of nitrogen, hydrocarbons, and carbon monoxide as well as improving combustion by blending nanofluids in a diesel engine. The secondary objective of this work is to develop specific IoT technology aids for the continuous monitoring of emissions in diesel engines at regular intervals of time.

2. Experimental Setup and Process

2.1. Emulsion Fuel Preparation. Water is a polar substance, whereas diesel is nonpolar in nature. Both polar and non-polar molecules are unbondable in nature. To obtain a homogenous mixture, a process called emulsification was implemented. Al_2O_3 nanoparticles dispersed in water emulsions significantly improve the properties of thermo-physical combustion. The incorporation of nanoparticles into a base fluid is a vital process. Therefore, special care was required. The prepared nanofluid must be an agglomerate-free stable suspension for extended periods without sedimentation.

Generally, for the preparation of nanofluids, the two-step method is optimistic, easy, and less expensive. The steps involved in preparing the nanofluid were as follows: a specific amount of $\gamma\text{-Al}_2\text{O}_3$ nanoparticles, Tween-20, and distilled water. Distilled water was poured into a beaker and nanoparticles and Tween-20 were slowly poured and stirred with a magnetic stirrer. Water and Al_2O_3 were thoroughly mixed using an ultrasonicator for at least one hour to obtain a nanofluid. Figure 1 shows a flow diagram for the preparation of the nano-fluid using a two-step method. Figure 2 shows SEM and TEM Images of the aluminum nanoparticles.

After the preparation of the nanofluid based on the blending ratio, the aqueous nanofluids were titrated with diesel fuel. A 3% NWED, 7% NWED, and 12% NWED emulsion blended ratio was prepared for experimentation. The properties of the diesel and emulsion blend are shown in Table 1.

2.2. Experimental Equipment Specification. The investigation was conducted on a single cylinder naturally aspirated vertical water-cooled diesel engine with a rated power of 5.12 kW at 1500 rpm and a compression ratio of 17.5 : 1. Figure 3 shows a

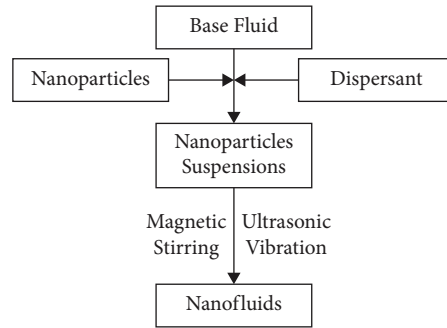


FIGURE 1: Procedure to prepare nanofluids using the two-step method.

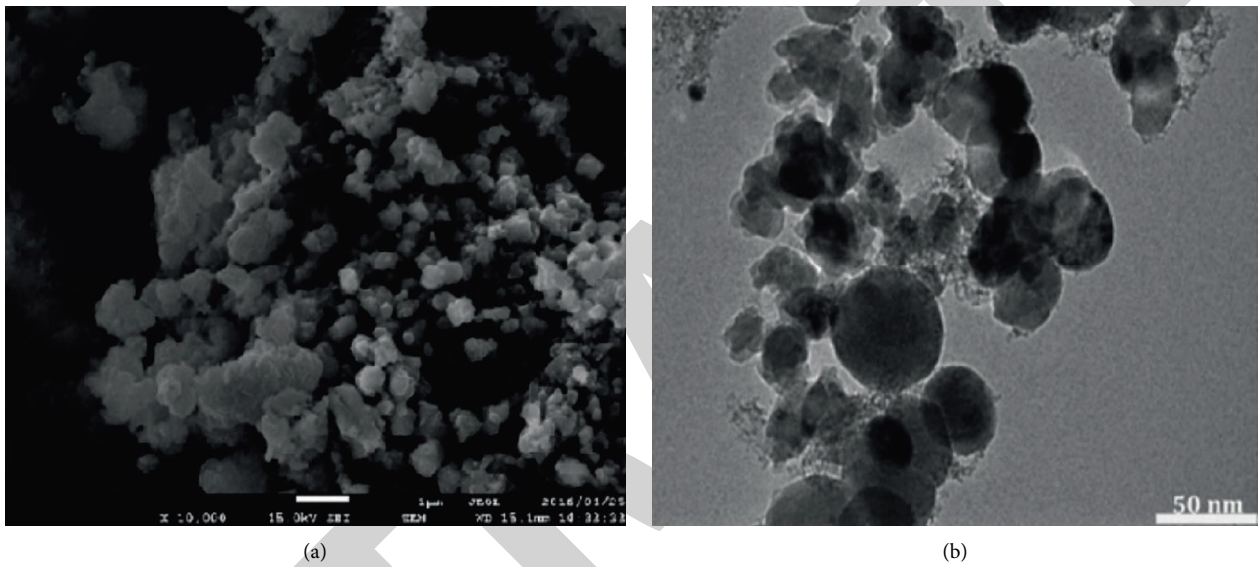


FIGURE 2: SEM and TEM image of Alumina nanoparticle.

TABLE 1: Properties of fuel.

Test description	Unit	Reference	Al ₂ O ₃ water emulsion blend			
		Limit	Diesel B0	3% NWED	7% NWED	12% NWED
Density	Gm/cc	0.800–0.900	0.832	0.833	0.846	0.854
Calorific value	MJ/kg	34–45	42.70	41.85	39.33	38.89



FIGURE 3: Photographic views of diesel engine.

detailed view of the diesel engine and explains the details of the engine that had been used for experimentation. The specifications and model names of the emission analyzers are also mentioned in detail in Tables 2 and 3.

- (i) Diesel engine specification
- (ii) Five gas analyzers

2.3. Statistical Analysis

- (a) Brake-specific fuel consumption

$$B_{sfc} = \frac{\text{Fuel flow in (kg/Hr)}}{\text{Brake power (kW)}} \times 100. \tag{1}$$

TABLE 2: Engine model: Kirloskar engine TV 1.

Type	Four stroke, single cylinder vertical water-cooled diesel engine
Rated power	5.12 kW
Rated speed	1500 rpm
Bore dia (D)	87.5 mm
Stroke (L)	110 mm
Compression ratio	17.5 : 1
Dynamometer	Eddy current dynamometer make: Techno mech Model: TMEC-10

TABLE 3: Details of five gas analyzer.

Model	AVL DI GAS 444 N
Measurement data	Resolution
Co-0-15% vol	0.0001% vol
HC-0-20000 ppm vol	1 ppm/10 ppm
NOx 0-6000 ppm vol	1 ppm vol

(b) Brake thermal efficiency

$$\text{BTE} = \frac{\text{Brake Power (kW)} \times 3600}{\text{FuelFlow (Kg/Hr)} \times \text{Calorific Value (KJ/Kg)}} \times 100. \quad (2)$$

The aforementioned equations were used for statistical analysis of brake-specific fuel consumption and brake thermal efficiency.

2.4. IoT Emission Setup. The Internet of Things is the ability to transmit data over a network, without the need for a computer, for humans or a human, provided by interconnected computing devices, mechanical and digital machines, objects, animals, or unique identifiers to each other. Initial deigning of the IoT kit used, Thinker CAD helps in executing the weather the algorithm suits the program. Figure 4 shows the circuit diagram for multiple gas sensors connected to the emission monitoring device layout. Finally, using the Arduino board all emission sensors are connected, and the code is uploaded to the board which executes the program easily. Figure 5 shows the IoT setup of the emission monitor device.

IoT requires a cloud for storing and sharing the data obtained from the kit. ThingSpeak is an open-source server that helps to transmit live emission data stored in the cloud and to visualize and analyze diesel emission results for analysts.

2.5. Uncertainty Analysis. There was no error-free experimental setup. Errors may occur owing to the inaccuracy of devices or instruments, inaccurate calibration, and lack of humanity; therefore, before starting any experimental work, uncertainty analysis is mandatory. To obtain the uncertainties of the independent and performance characteristics, a sequential perturbation technique was employed. These include the air flow rate (1.1%), engine load (0.1%), fuel flow rate (0.1%), and engine speed (1.3%). As a result, the

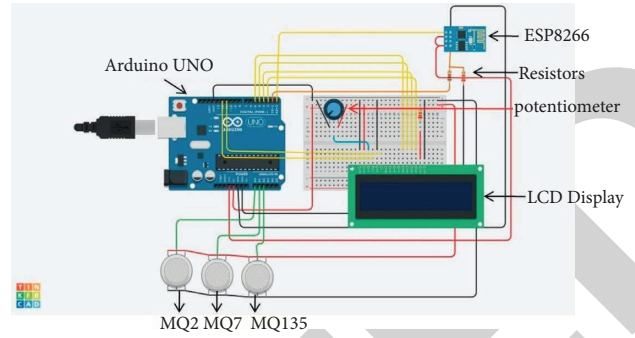


FIGURE 4: The circuit diagram for multiple gas sensors connected emission monitor device.

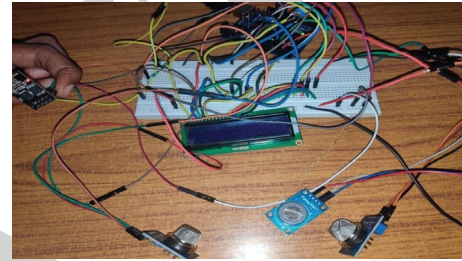


FIGURE 5: Emission monitors device IoT setup.

calculated accuracy of the performance and combustion study for both nano-based water emulsion and diesel-run engines were found to be within ± 3.6 . However, the emission accuracy was within $\pm 2.1\%$. Generally, the uncertainty calculation value is obtained using the following equation:

$$R = \sum X_i^2, \quad (3)$$

where R = root mean square value of the uncertainty and X_i = parameter's uncertainty values.

The standard deviation formula is given as follows:

$$\sigma = \sqrt{\frac{\sum_{i=1}^n (x_i - \bar{x})^2}{N}}, \quad (4)$$

where σ = standard deviation, x_i = terms given in the data, \bar{x} = mean, and N = total number of terms.

The standard error formula is given as follows:

$$\text{SE} = \frac{\sigma}{\sqrt{N}}, \quad (5)$$

where SE = standard error, σ = standard deviation, and N = total number of terms.

Table 4 shows the error chart for brake thermal efficiency, brake-specific fuel consumption and emissions at regular intervals of time operation.

3. Results and Discussion

3.1. Performance Analysis. The brake-specific fuel consumption (BSFC) of the engine using diesel and the three types of nano-W/D under different load conditions with constant speed are illustrated in Figure 6. As shown in the

TABLE 4: Error chart.

	Brake power (kW)	Brake thermal efficiency (%)	Brake-specific fuel consumption (kg/kWh)	Carbon monoxide (%)	Hydro carbons (Ppm)	Oxide of nitrogen (Ppm)	Smoke (%)	Time of operation (min)
	2.61	27.73	0.31	0.025	27	991	14.7	30
	2.61	27.73	0.32	0.026	25	990	14.6	60
	2.61	27.74	0.29	0.025	27	991	14.7	90
	2.61	27.73	0.31	0.025	27	992	14.7	120
	2.61	27.74	0.31	0.024	26	991	14.8	180
Mean	2.61	27.73	0.31	0.025	26.4	991	14.7	
Standard deviation	0	0.005	0.011	0.0007	0.89	0.71	0.07	
Standard error	0	0.002	0.005	0.0003	0.4	0.32	0.03	
Upper control limit	2.61	27.745	0.343	0.0271	29.67	992.13	14.91	
Lower control limit	2.61	27.724	0.295	0.024	25	990	14.6	

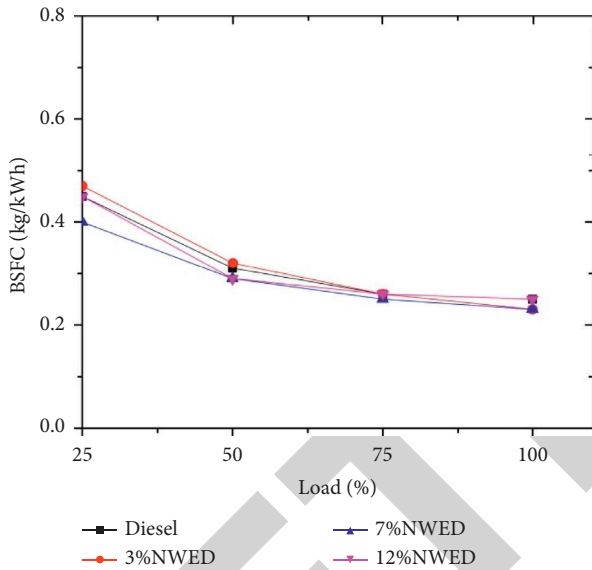


FIGURE 6: Load vs. BSFC.

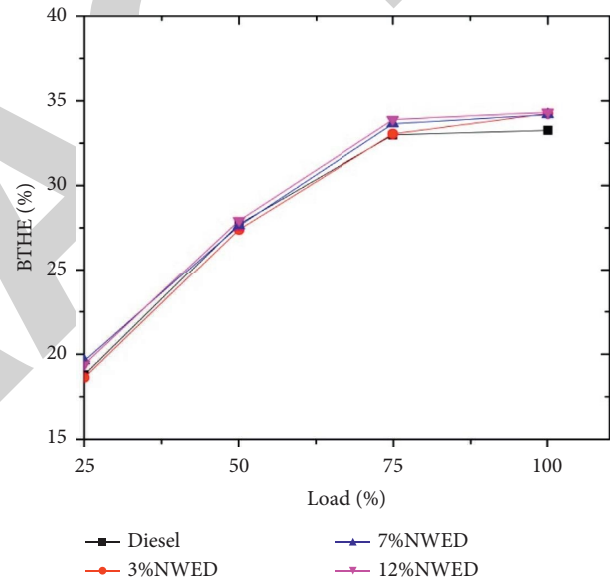


FIGURE 7: Load vs. BTHE.

graph, all three nano-W/D ratios show that BSFC at initial loads is high owing to the lower heating value in the presence of nano-based water emulsion and gradually reduces when the load is increasing, which indicates that the fuel burns in the engine effectively at higher engine loads. While running the engine with nano-W/D no identities are found in misfiring or unusual behavior. The potential benefit of water in diesel nanoemulsion fuels are as follows: (i) The overall impact of the secondary atomization and microexplosion phenomenon, resulting in strong evaporation and better mixing of air and changes in improving the combustion reactions inside the engine cylinders, (ii) Improved air-penetration in the spray due to increased spray momentum, (iii) Better-premixed combustion due to ignition delay, (iv) Increase in excess air ratio due to the presence of water in the emulsion, (v) Reduction of cooling loss due to a decrease in combustion temperature, (vi) Quash of thermal dissociation as a result of dropping in combustion temperature, and (vii) The presence of Al_2O_3 nanofluid in diesel emulsion that

triggers less combustion gas release. Both 7% and 12% NWED blends show better fuel consumption, and it was observed that 7% NWED showed better load conditions. If the percentage of emulsion increases, the cylinder temperature decreases owing to the water percentage and its effect on combustion and emissions.

Figure 7 shows the variations in brake thermal efficiency of $\gamma-Al_2O_3$ with water and diesel test fuels under different engine loads. Compared with diesel and nano-based water emulsion blends, the blends showed an improvement in performance at higher loads. This is due to the addition of $\gamma-Al_2O_3$ in water and diesel at high temperatures; these mixtures turn into hydro-liquid fuel and emit high energy in the combustion process. Figure 8 clearly shows that the brake thermal efficiency increased at different concentrations of aqueous nanofluid emulsion on diesel engines with different loads. The percentage of aqueous nanofluid increased the brake thermal efficiency at higher loads.

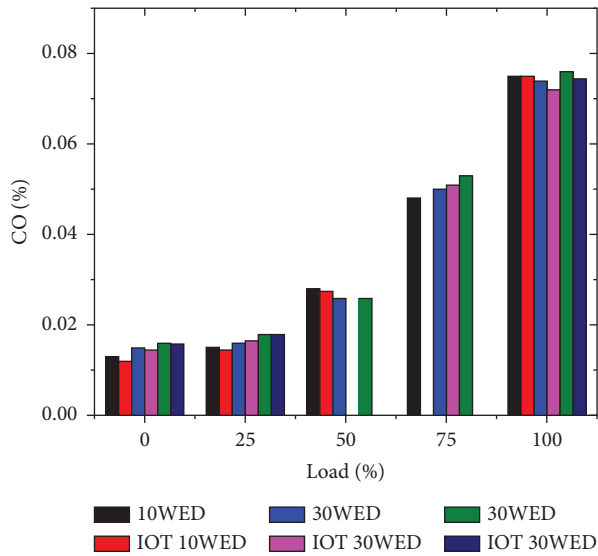


FIGURE 8: Load vs. CO.

3.2. *Combustion Analysis.* Figure 9 shows the crank vs. cylinder pressure at full load with diesel, 3%, 7%, and 12% aqueous γ -Al₂O₃ emulsion blends. The peak pressures at full load on diesel are 71.99 bar, 71.82 bar, 72.17 bar, and 71.75 bar at 23°. BTDC injection timing. In addition, the cylinder pressure is improved owing to the better atomization of air and nano-W/D fuel particles during ignition, which helps to improve the heat release rate inside the engine cylinder.

Figure 10 shows the rate of heat released inside the combustion chamber with different fuel blends under full load conditions in diesel engines. The addition of γ -Al₂O₃ with water and diesel at the time of surface flame formation causes, water and nanoparticles to penetrate and convert water into hydrogen gas, and γ -Al₂O₃ procures a sufficient amount of oxygen for better atomization to improve the combustion rate. When compared with aqueous blends, the 7% NWED blend showed the best results.

3.3. *Emission Analysis.* According to Zeldovich's approach, the formation of nitrogen oxides depends on oxygen density, the time required for formation, and temperature. In water with high oxygen content, the water content within the inner phase absorbs the calorific heat charge of the emulsion. Consequently, this reduces the burning gasoline temperature during the combustion and consequently restricts the generation of NO_x. At the time of combustion, the aqueous solution vaporized and tended to reduce the flame temperature. Figure 11 shows the variation between NO_x and the load. Compared with diesel, the emulsion blends showed little difference in the graph. This is because γ -Al₂O₃ reduces the cylinder wall temperature inside the engine chamber, thus restricting the NO_x formation. An increase in the percentage of aqueous emulsions reduced the NO_x level. The average reduction of 3%, 7%, and 12% NWED for every load were 31.46%, 38.76%, and 45.48%, respectively.

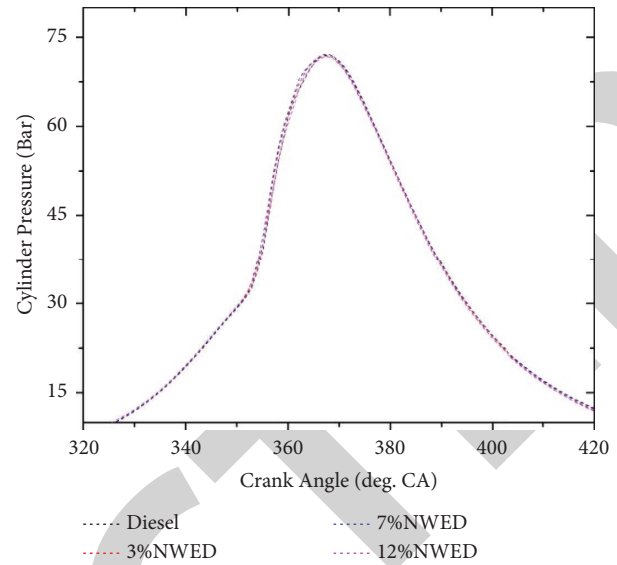


FIGURE 9: Crank angle vs. cylinder pressure.

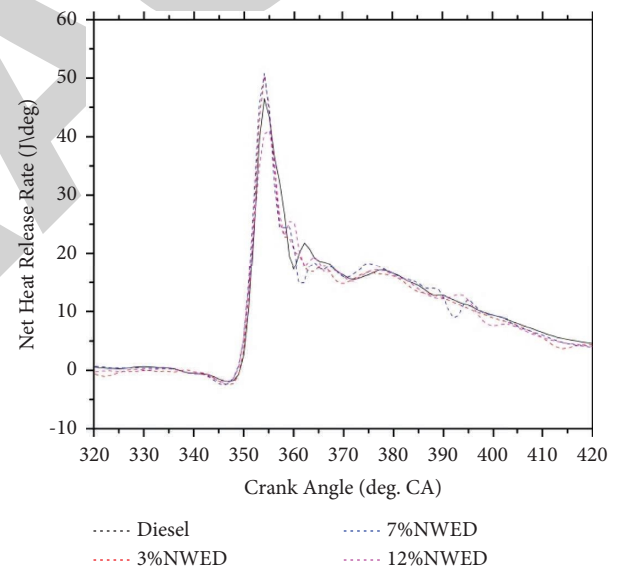


FIGURE 10: Crank angle vs. net heat release rate.

Figure 12 shows the CO formation at various loads. The formation of CO depends on the air-fuel ratio. The lean mixture led to the low CO formation in the CI engines. By the addition of γ -Al₂O₃ in water emulsion diesel formation of OH levels, leads to a clean and high combustion rate and clearly shows that incomplete combustion is reduced. When the percentage of aqueous γ -Al₂O₃ increased, it enhanced the rate of combustion, and the nanoparticles provided a sufficient amount of oxygen to help reduce CO and HC emissions. Figure 13 shows HC versus load. In the 7% NWED blend, the diesel engine showed a reduction in HC and CO emissions compared with diesel. Nanoparticles provide a surplus of oxygen molecules at a higher load to complete the combustion process.

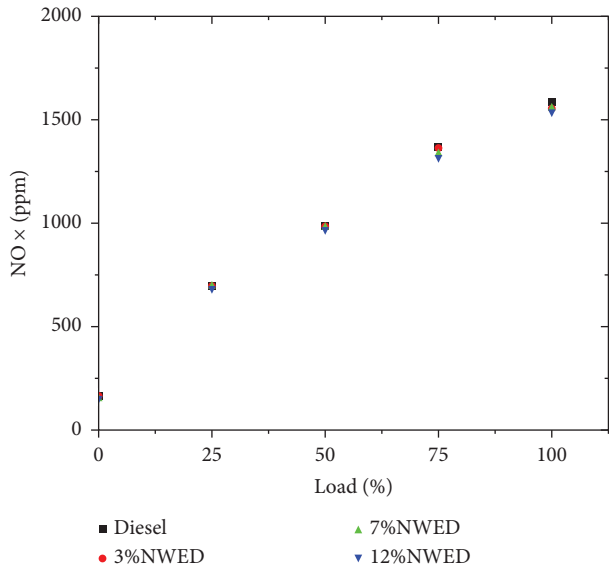


FIGURE 11: Load vs. NO_x.

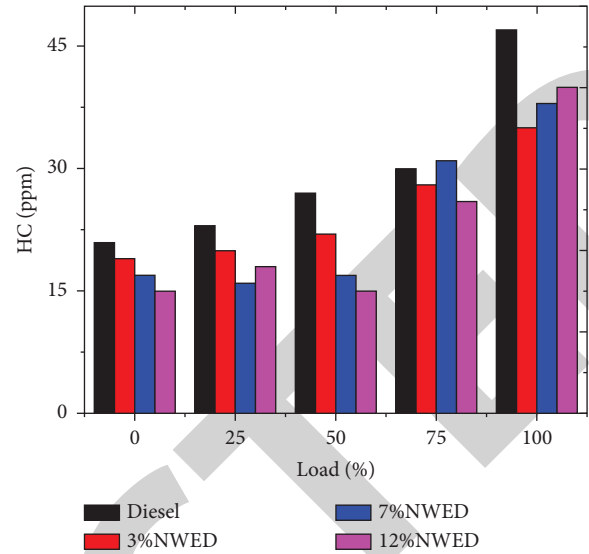


FIGURE 13: Load vs. HC.

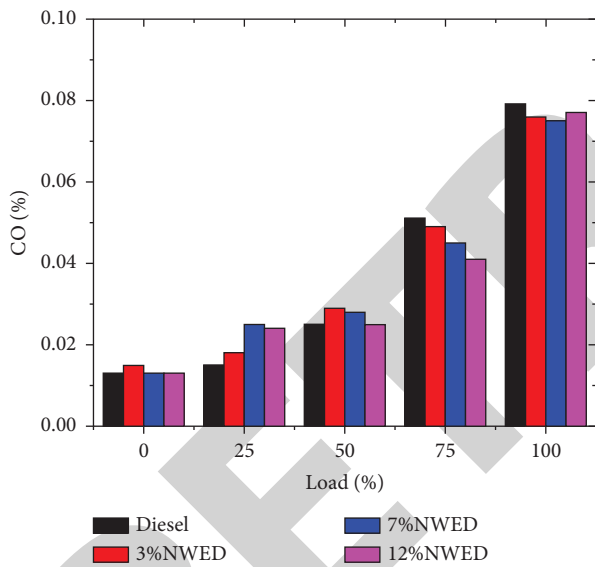


FIGURE 12: Load vs. CO.

3.4. Emission Analysis with IoT. Emissions are monitored with the help of AVL DI GAS 444 N. AVL compulsorily needs a human presence for collecting the emission data and it is an expensive process. In the 20th century Internet of things (IoT), there are tremendous changes in the usage of mechanical equipment and the monitoring system. With the help of IoT and the arrangement of its auxiliary components without the presence of human need emissions would be recorded and sent to the server. By comparing the IoT kit and AVL gas analyzer the emission values are aqua-rated. Figure 14 shows the emission monitoring data visualized in the system. The comparison of HC, CO, and NOx with both analyzers shows that the variations vary around ± 0.2 as shown in Figures 8, 15, 16.

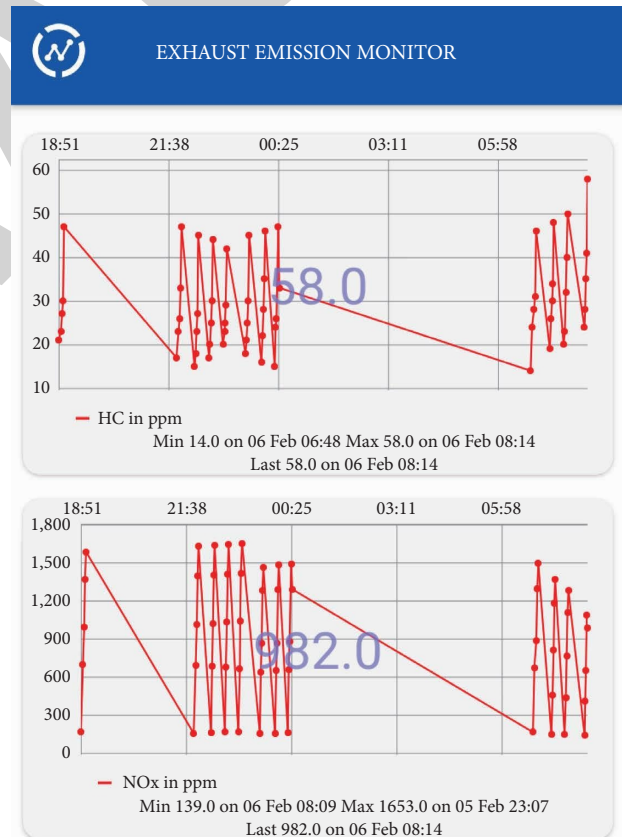


FIGURE 14: The channel opens the access to read the data stored (portrait mode).

3.4.1. Carbon Monoxide (CO). A comparison of CO emissions with the five gas emission analyzer and IoT emission kit is shown in Figure 8. Carbon monoxide is produced during incomplete combustion. Anything that leads to incomplete combustion increases CO production. In other words, as the

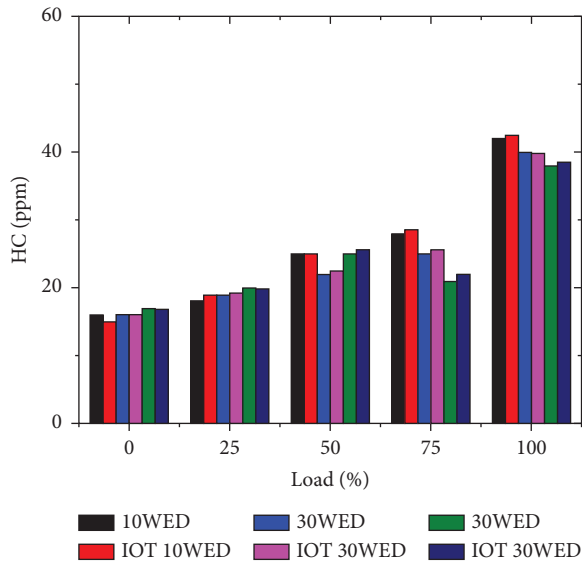


FIGURE 15: Load vs. HC.

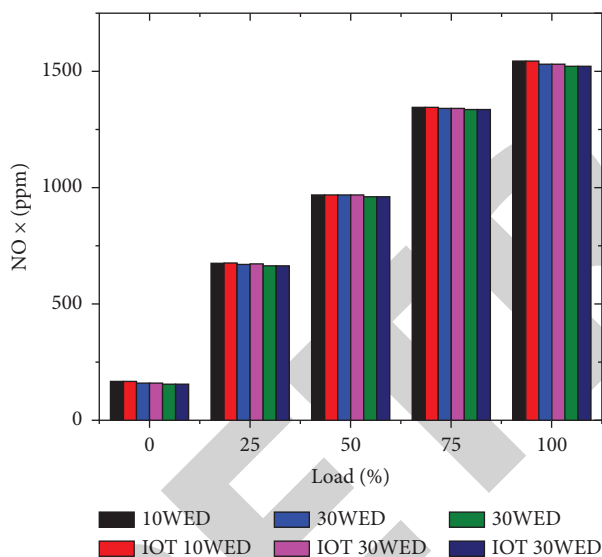


FIGURE 16: Load vs. NOx.

load increases, CO emissions increase, as a lower combustion temperature results in higher CO emissions.

3.4.2. Hydrocarbons (HC). In an engine, there is a small amount of fuel oil, rich in hydrocarbons, which pass through unburnt, while other hydrocarbons are produced during combustion. As a result, hydrocarbons are mainly particles of unburned or partially burned fuels. Additionally, lubrication oil emits hydrocarbons. The variation in hydrocarbon emissions with load is shown in Figure 15.

3.4.3. Oxide of Nitrogen (NO_x). At high temperatures, combining oxygen with nitrogen results in nitrogen oxides (NO_x) released into the atmosphere. The two types of

emission analyzers are shown in Figure 16 to illustrate the variation in NO_x emissions.

4. Conclusion

In this study, emphasis was placed on the impact of an aqueous nanofluid diesel emulsion on diesel engine performance, combustion, and emission characteristic in comparison with diesel. Based on the results and investigation, the following conclusions were drawn:

- (1) It has been observed that the brake-specific fuel consumption is reduced to 4.2% when compared with diesel on the addition of γ -Al₂O₃ in water emulsion. However, the engine brake thermal efficiency slightly improved when compared with aqueous nanofluids diesel emulsion, and diesel fuel.
- (2) With the addition of aqueous γ -Al₂O₃ to diesel, the combustion rate, and cylinder pressure exhibited almost the same peaks. Further, increases the blend percentage of aqueous γ -Al₂O₃ it affects in-cylinder temperature.
- (3) In the combustion process, the addition of aqueous γ -Al₂O₃ to diesel produces a surplus amount of oxygen atoms to complete the effective combustion inside a diesel engine, which helps to reduce HC, NO_x, and CO.
- (4) The IoT emission monitoring kit helps for continuous monitoring of emission data.

Nomenclature/Abbreviations

Al ₂ O ₃ :	Aluminum oxide
BSFC:	Brake-specific fuel consumption
BTDC:	Before top dead center
BTHE:	Brake thermal efficiency
B0:	Pure diesel
CAD:	Computer-aided design
CO:	Carbon monoxide
CO ₂ :	Carbon dioxide
HC:	Hydrocarbons
Gm/cc:	Gram per cubic centimeter
IOPs:	Injecting opening pressures
IoT:	Internet of Things
Kg/kWh:	Kilogram/kilowatt-hour
KW:	Kilo Watt
Mj/kg:	Mega joules per kilogram
Mm:	Millimeter
Min:	Minute
NWED:	Nano-based water emulsion Diesel
NO _x :	Nitrogen oxides
OH:	Hydroxyl radical
O/W:	Oil-in-water
O/W/O:	Oil-in-water-in-oil
Ppm:	Parts per million
RFID:	Radio-frequency identification
Rpm:	Revolutions per minute
SEM:	Scanning electron microscope
TEM:	Transmission electron microscope

Retraction

Retracted: Response Surface Methodology Approach to Predict the Flexural Moment of Ferrocement Composites with Weld Mesh and Steel Slag as Partial Replacement for Fine Aggregate

Advances in Materials Science and Engineering

Received 8 January 2024; Accepted 8 January 2024; Published 9 January 2024

Copyright © 2024 Advances in Materials Science and Engineering. This is an open access article distributed under the Creative Commons Attribution License, which permits unrestricted use, distribution, and reproduction in any medium, provided the original work is properly cited.

This article has been retracted by Hindawi following an investigation undertaken by the publisher [1]. This investigation has uncovered evidence of one or more of the following indicators of systematic manipulation of the publication process:

- (1) Discrepancies in scope
- (2) Discrepancies in the description of the research reported
- (3) Discrepancies between the availability of data and the research described
- (4) Inappropriate citations
- (5) Incoherent, meaningless and/or irrelevant content included in the article
- (6) Manipulated or compromised peer review

The presence of these indicators undermines our confidence in the integrity of the article's content and we cannot, therefore, vouch for its reliability. Please note that this notice is intended solely to alert readers that the content of this article is unreliable. We have not investigated whether authors were aware of or involved in the systematic manipulation of the publication process.

Wiley and Hindawi regrets that the usual quality checks did not identify these issues before publication and have since put additional measures in place to safeguard research integrity.

We wish to credit our own Research Integrity and Research Publishing teams and anonymous and named external researchers and research integrity experts for contributing to this investigation.

The corresponding author, as the representative of all authors, has been given the opportunity to register their agreement or disagreement to this retraction. We have kept a record of any response received.

References

- [1] J. Sridhar, G. B. Shinde, D. Vivek et al., "Response Surface Methodology Approach to Predict the Flexural Moment of Ferrocement Composites with Weld Mesh and Steel Slag as Partial Replacement for Fine Aggregate," *Advances in Materials Science and Engineering*, vol. 2022, Article ID 9179480, 9 pages, 2022.

Research Article

Response Surface Methodology Approach to Predict the Flexural Moment of Ferrocement Composites with Weld Mesh and Steel Slag as Partial Replacement for Fine Aggregate

Jayaprakash Sridhar,¹ Ganesh Bhausaheb Shinde,² D Vivek,³ Khalida Naseem,⁴ Piyush Gaur,⁵ Pravin P Patil,⁶ and Misganaw Tesfaye Tesema ⁷

¹Department of Civil Engineering, GMR Institute of Technology, Rajam, Srikakulam, Andhra Pradesh, India

²Department of Chemical Engineering, Sir Visvesvaraya Institute of Technology, Nashik 422101, India

³Department of Civil Engineering, KPR Institute of Engineering and Technology, Coimbatore, Tamil Nadu, India

⁴Department of Basic and Applied Chemistry, Faculty of Science and Technology, University of Central Punjab, Lahore, Pakistan

⁵Mechanical Engineering Cluster, School of Engineering, University of Petroleum and Energy Studies, Bidholi Campus Via Premnagar, Dehradun, Uttarakhand 248002, India

⁶Department of Mechanical Engineering, Graphic Era Deemed to Be University, Bell Road, Clement Town 248002, Dehradun, Uttarakhand, India

⁷Department of Chemical Engineering, College of Biological and Chemical Engineering, Addis Ababa Science and Technology University, Addis Ababa, Ethiopia

Correspondence should be addressed to Misganaw Tesfaye Tesema; misganaw.tesfaye@aastustudent.edu.et

Received 8 May 2022; Revised 12 June 2022; Accepted 15 July 2022; Published 30 August 2022

Academic Editor: Akbar Heidarzadeh

Copyright © 2022 Jayaprakash Sridhar et al. This is an open access article distributed under the Creative Commons Attribution License, which permits unrestricted use, distribution, and reproduction in any medium, provided the original work is properly cited.

Design of Experiment-Response surface methodology approach is adopted to obtain the optimal flexural moment of ferrocement composites comprising galvanised square weld mesh with weight fraction of fine aggregate by steel slag. To get the optimal combination of progression variables on a flexural moment of ferrocement composites, the central composite design of response surface methodology was adopted. Regression models for responses were justified using analysis of variance and the Pareto chart. The test results show that a maximum ultimate load of 3.30 kN and moment capacity of 220 kNm was obtained for ferrocement with a volume fraction of 2.733% and steel slag of 25% replacement. From the analysis of variance, it is evident that the p value is less than 0.005, the predicted R^2 and the adjustable R^2 are less than 20%, and the predicted values go in hand with the experimental result which indicates that the proposed models are highly suitable. Moreover, the volume fraction of galvanised square weld mesh has a higher significance on a flexural moment of ferrocement composites. Surface plot, Pareto chart, and regression analysis outcomes show that the most substantial and influential factor for a flexural moment is the volume fraction of galvanised square weld mesh.

1. Introduction

Ferrocement is a special form of composite with 90% of its total volume occupied by cement mortar and the rest by galvanised weld mesh or chicken mesh etc. The composites may contain discontinuous fibres also [1, 2]. As it contains uniform mesh reinforcement spread throughout its surface, the crack arresting mechanism of ferrocement is high when compared to concrete structures [3]. Ferrocement reinforced

with galvanised square weld mesh shows higher load carrying capacity and moment capacity when compared with ferrocement with GI mesh. Increase in the volume fraction of mesh reinforcement increases the moment capacity [4]. The ultimate moment capacity of ferrocement prediction by group method of data handling (GMDH) has higher accuracy when compared to other models [5]. Ferrocement with a chicken mesh having a volume fraction of 3.77% and 30% partial replacement of fine aggregate by steel slag has a

greater first crack load and ultimate load when related to other specimens [6]. Predicted moment capacity of ferrocement with self-evolving network model has higher accuracy when compared with plastic analysis and mechanism approach method [7]. Ferrocement with 2 and 4 layers of weld mesh increases axial stress by 61% and 31%, respectively, with rich mortar containing silica fumes and metakaolin [8]. To learn the influence of the autonomous variables on the outcomes with the least experiments, statistical and mathematical method of Design of Experiments (DOE) preferably Response Surface Methodology can be adopted [9–12]. The test variables can be optimised with DOE which provides a relationship between the empirical model and independent variables and finally delivers optimal response for experimental data [13]. The predicted moment capacity of ferrocement composites with artificial neural network has more accuracy when compared to other methods like GMDH and ANFIs [14]. Ferrocement laminates characterised using digital image correlation reveal that as mesh volume fraction increases, flexural capacity, ductility index, energy absorption, and number of cracks by length increase, whereas the width of the crack decreases [15]. Ferrocement slabs reinforced with chicken mesh having skeleton reinforcement with bamboo and mortar mix of 1:3 have higher mechanical properties, and predicted theoretical results support the experimental results [16]. Ferrocement with 2 and 4 layers of weld mesh increases axial stress by 61% and 31%, respectively, with rich mortar containing silica fumes and metakaolin [8]. When the number of layers of wire mesh increased in ferrocement for strengthening of reinforced concrete better yield loads, ultimate loads and stiffnesses are obtained [17].

In the current study, an effort was made to improve the load carrying capacity and moment capacity of ferrocement with galvanised square weld mesh and steel slag. Design of experiment (DOE) is used to design the experiments. The effect of autonomous parameters on experimental results can be studied with the help of the DOE technique. To get the optimal combination of independent variables (volume fraction and steel slag) and to study the influence of independent variables on ultimate load and moment capacity, central composite method (CCM) statistical analysis was accomplished.

2. Methodology

The present experimental programme is designed by using the response surface methodology which evaluates the effect and interaction of multiple variables on a dependent variable. The experimental data were obtained from the flexural behaviour of ferrocement laminates under flexure. The appropriate regression model is chosen by the most appropriate transform due to lack of fit or by removing the extra or insignificant factors due to overfitting. The final model is obtained when the linear regression assumptions are satisfied. Optimization is done for the combined effect of volume fraction and steel slag replacement for fine aggregate to achieve maximum ultimate load and moment capacity. The step-by-step procedure to achieve response models and optimisation is shown in Figure 1.

3. Response Surface Method

The Response Methodology is a mathematical and statistical tool helpful in designing, enhancing, and developing issues where outcomes are influenced by many influencing factors [18]. In RSM, central composite design is used to determine the relationship between outcome variables and independent variables [19]. In DOE of RSM, autonomous variables, factors, and levels of variables are to be provided as shown in Table 1 for considered two responses. The required number of experiments is obtained by

$$N = 2^k + 2k + n, \quad (1)$$

where k is the number of factors, and n is the number of centre points [20]. To obtain the optimum response, following the quadratic model or second order polynomial (2) was used:

$$Y = \beta_0 + \sum_{i=1}^n \beta_i x_i + \sum_{i=1}^n \beta_{ii} x_i^2 + \sum_{i=1}^n \sum_{i=n}^n \beta_{ij} x_i x_j; (i \neq j), \quad (2)$$

where β_0 is a constant; and β_{ii} and β_{ij} are the linear coefficient, quadratic coefficient, and interactive coefficient, respectively.

4. Materials and Testing

OPC 53 having a specific gravity of 3.15, an initial setting time of 35 minutes as per IS: 4031-1988 and IS: 12269-1987 was used for this investigation [21, 22]. River sand passing through 2.36 mm having a specific gravity of 2.68 as per IS: 383-1970 and ACI 549 1R-93, 1999 is used for ferrocement [23, 24]. Steel slag an effective substitute material is used as a partial replacement for river sand [25]. Steel slag passing through 2.36 mm with a specific gravity of 2.95 was used as per the recommendations of IS 228, 1987 [26] and ACI 233 R-03, 200 [27]. Galvanized square weld mesh having a yield strength of 660 N/mm² was used. Ferrocement of size 150 mm × 25 mm × 500 mm were cast as per the specifications in Table 2. The ferrocement composites are tested under flexure with a simply supported span of 400 mm.

5. Results and Discussion

5.1. Experimental Investigation: From Figure 2, it is evident that an ultimate moment of 2.80 kN is obtained for ferrocement laminates with a volume fraction of 1.425% with 25% weight fraction of steel slag and 2.35% volume fraction with 0% steel slag. Similarly, a maximum ultimate load of 3.30 kN was obtained for ferrocement laminates with 2.73% of volume fraction and 25% of steel slag substitution for fine aggregate. It is observed that ultimate load reduces for specimens with 0.5% volume fraction and 50% of steel slag replacement. Moreover, it is evident that ultimate load reduces with reduce in volume fraction and an increase in steel slag substitution [28].

Similarly, from Figure 3 it is observed that maximum moment capacity is obtained for ferrocement laminates with a volume fraction of 2.73% with 25% of steel slag for fine

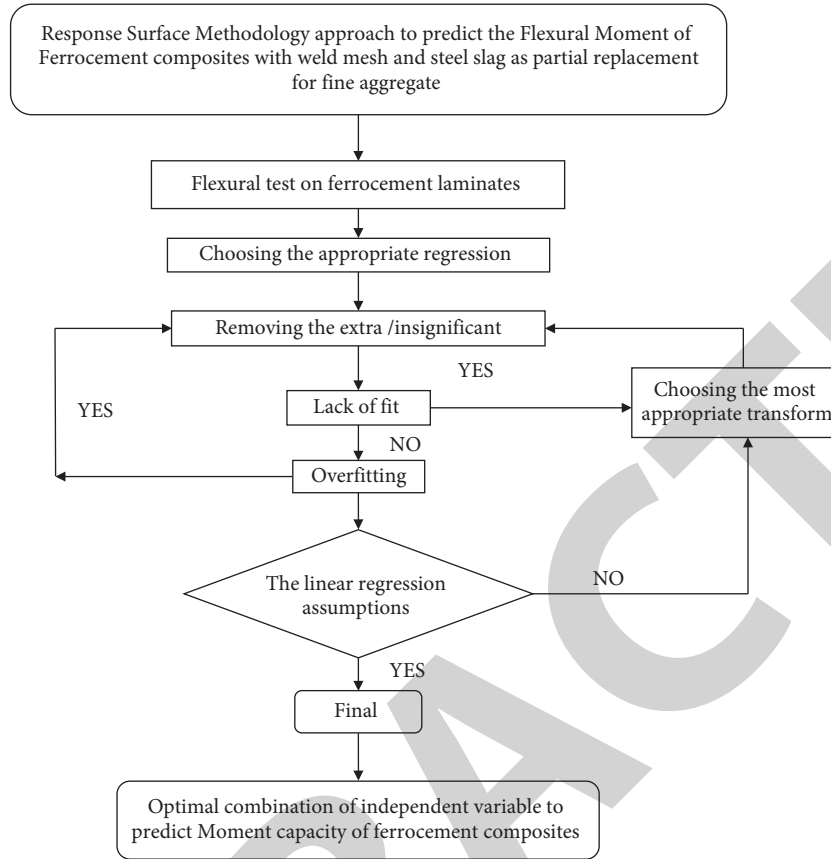


FIGURE 1: Step-by-step approach to achieve response models and optimisation.

TABLE 1: Levels of variables.

Variables	Low level (-1)	Intermediate level (0)	High level (+1)
Ferrocement volume fraction	≤ 0.01	1.425	2.35
Steel slag	≤ 0.01	25	50

aggregate. It is evident that for the lower volume fraction of galvanised square weld mesh, ultimate load and moment capacity reduces. On the other hand, for higher volume fraction, ultimate load and moment capacity increases. It is clear from the graph that for the increase in volume fraction moment capacity increases because of increased moment arm distance and increased passive confining pressure. Moreover, the diameter of weld mesh and mesh opening provides good anchorage between cement matrix and weld mesh which indirectly increases moment carrying capacity [29, 30]. The galvanised square weld mesh wires were found to be more effective in increasing the ultimate load.

5.2. RSM Modelling: Observations and Discussions. In this study, central composite design (CCD) is used to know the impact of independent parameters of volume fraction and steel slag on the ultimate load and moment capacity of ferrocement laminates. As shown in Table 3 experiments were considered to determine the response on ultimate load and moment capacity. The estimated responses are given in (3) and (4):

$$ULFC = 0.203 + 1.865(X_1) + 0.0516(X_2) - 0.320(X_1)*(X_1) - 0.000879(X_2)*(X_2) - 0.00486(X_2)*(X_2), \quad (3)$$

$$\text{Moment capacity} = 13.5 + 124.3(X_1) + 3.44(X_2) - 21.33(X_1)*(X_1) - 0.0586(X_2)*(X_2) - 0.324(X_1)*(X_2). \quad (4)$$

The normal probability of ultimate load and moment capacity responses are shown in Figure 4. From the figure, it is clear that all the responses fall near the straight line, which

confirms that errors are evenly distributed. Analysis of variance is useful to know the relationship between autonomous variables and responses to a collection of

TABLE 2: Details of test specimen with galvanised square weld mesh for flexure test.

Designation	Volume fraction (X_1)	Steel slag (X_2)
FCWM01	1.425	0.0000
FCWM02	1.425	25.0000
FCWM03	2.350	0.0000
FCWM04	1.425	25.0000
FCWM05	2.350	50.0000
FCWM06	1.425	25.0000
FCWM07	0.116	25.0000
FCWM08	1.425	60.3553
FCWM09	1.425	25.0000
FCWM10	0.500	50.0000
FCWM11	0.500	0.0000
FCWM12	2.733	25.0000
FCWM13	1.425	25.0000

statistical models and it is arrayed in Table 4. From Table 4, it is evident that p value is less than 0.005 which indicates that models are highly suitable. From Table 5, it is seen that variation of predicted R^2 and the adjustable R^2 are less than 20%. Moreover, the R^2 value of ultimate load and moment capacity is 93.14%. From Figures 5 and 6, it is clear that the model arrived can be used to predict the ultimate load and moment capacity of ferrocement laminates as the predicted values go in hand with experimental results. Moreover, the models can be validated based on the F value.

5.3. *Pareto Analysis and Lack of Fit (p Value)*. The independent variables can be considered as important and extremely important if the p value of the progression variable is < 0.005 and < 0.001 , respectively. If the p value of the independent variable is more than 0.005, then it is considered as insignificant. From ANNOVA Table 4, it is clear that the p value of the linear and quadratic X_1 is less than 0.005, but the p values of the linear and quadratic X_2 were higher than 0.005. So, it clearly indicates that volume fraction is highly significant for ultimate load and moment capacity. Moreover, as steel slag is higher than 0.005, the significance of steel slag is less for volume fraction and moment capacity. From the Pareto chart as shown in Figures 7(a) and 7(b), the value of linear (A) was higher when compared to linear AA, AB, and BB which shows that volume fraction is more significant than steel slag for ultimate load and moment capacity. Similarly, from ANOVA Table 4 the p value of linear X_1 is higher when compared to X_2 , which means the volume fraction is the most substantial factor in evaluating the ultimate load and moment capacity. The observations agree with previous literature which clearly states that volume fraction may enhance the ultimate load and moment capacity significantly.

5.4. *Surface Plot Analysis, Contour Plot Analysis, and Optimisation of Progression Variables*. Three-dimensional (3D) surface plots were plotted in Figures 8(a) and 8(b) to comprehend the effect of independent variables on the responses. In the surface plot, the independent variables volume fraction and steel slag were plotted in the “x” and “y” direction and the



FIGURE 2: Ultimate load for different steel slag replacement and volume fraction of weld mesh ferrocement laminates.

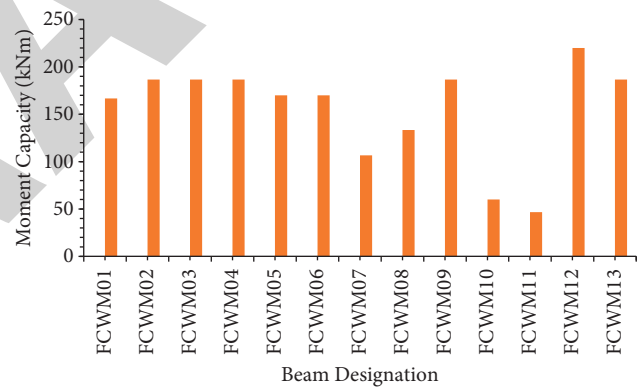


FIGURE 3: Moment capacity for different steel slag replacement and volume fraction of weld mesh ferrocement laminates.

TABLE 3: Comparison of experimental and predicted results.

Designation	Ultimate load (kN)		Moment capacity (kNm)	
	Exp	RSM	Exp	RSM
FCWM01	2.50	2.25	166.67	147.31
FCWM02	2.80	2.81	186.67	185.15
FCWM03	2.80	2.92	186.67	187.81
FCWM04	2.80	2.81	186.67	185.15
FCWM05	2.55	2.73	170.00	175.24
FCWM06	2.55	2.81	170.00	185.15
FCWM07	1.60	1.14	106.67	76.07
FCWM08	2.00	1.74	133.34	113.60
FCWM09	2.80	2.81	186.67	185.15
FCWM10	0.90	1.32	60.00	87.72
FCWM11	0.70	1.06	46.67	70.32
FCWM12	3.30	3.45	220.00	221.13
FCWM13	2.80	2.81	186.67	185.15

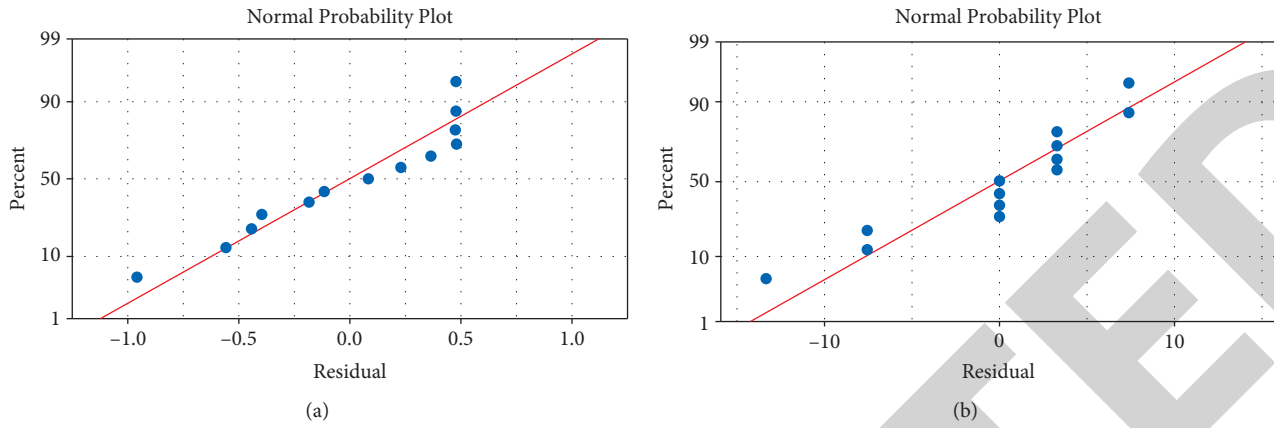


FIGURE 4: Normality graph of (a) ultimate load; (b) moment capacity.

TABLE 4: ANOVA for ultimate load and moment capacity.

Source	Ultimate load			Moment capacity		
	DF	F-value	p value	DF	F value	p value
Model	5	12.81	0.002	5	12.81	0.002
Linear	2	22.39	0.001	2	22.39	0.001
X_1	1	44.76	≤ 0.01	1	44.76	≤ 0.01
X_2	1	0.02	0.887	1	0.02	0.887
Square	2	9.08	0.011	2	9.08	0.011
X_1^2	1	5.00	0.060	1	5.00	0.060
X_2^2	1	13.83	0.007	1	13.83	0.007
Two-way interaction	1	0.48	0.511	1	0.48	0.511
$X_1 * X_2$	1	0.48	0.511	1	0.48	0.511

TABLE 5: proportion of variance (R^2) of the regression model.

Responses	R^2 (%)	Adjusted R^2 (%)	Predicted R^2 (%)	Difference between adjusted R^2 and predicted R^2 (%)
Ultimate load	93.14	90.10	87.23	2.87
Moment capacity	93.14	90.10	87.23	2.87

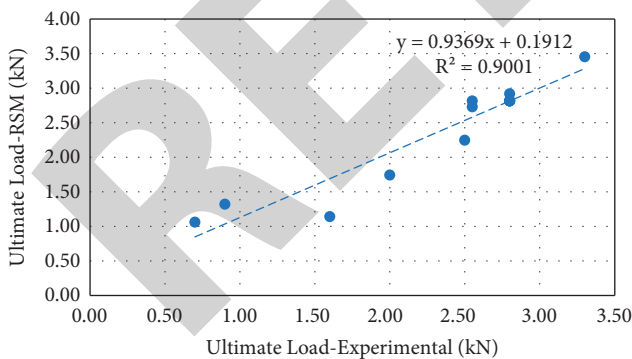


FIGURE 5: Predicted and actual values of ultimate load.

response ultimate load and moment capacity were plotted in the “z” axis. From Figures 8(a) and 8(b), it is understood that the increase in volume fraction from 0.5% to 2.35% increases the ultimate load and moment capacity for the ferrocement laminates, which clearly depicts volume fraction has a high significance in ultimate load and moment capacity. Although the volume fraction is the significant factor for ultimate load and moment capacity, the addition of steel slag also increases

the load carrying capacity up to 25% replacement of fine aggregate by steel slag, beyond which ultimate load and moment capacity reduces. From the surface plot, it is understood that maximum ultimate load and moment capacity was obtained for the volume fraction of 2.73% and steel slag of 25% by weight of fine aggregate. From Figures 9(a) and 9(b), the contour plot which is plotted for independent variables volume fraction and steel slag shows the range of distribution of ultimate load and moment capacity. The response of the graph confirms with results obtained from 3D surface plots. The optimised ultimate load and moment capacity of ferrocement laminates are shown in Figures 9(a) and 9(b). The notations “y” and “d” plotted in Figure 9 refer to the maximum ultimate load and moment capacity value and appeal of the independent variables from zero to one, where zero indicates the undesirable variable and one represents the desirable variable. From Figures 10(a) and 10(b), it can be seen that to attain the maximum ultimate load and moment capacity, the optimal value of volume fraction and steel slag was found to be 2.73% and 21.95% of weight fraction, respectively. The validation test was executed to confirm the outcomes as shown in Table 6.

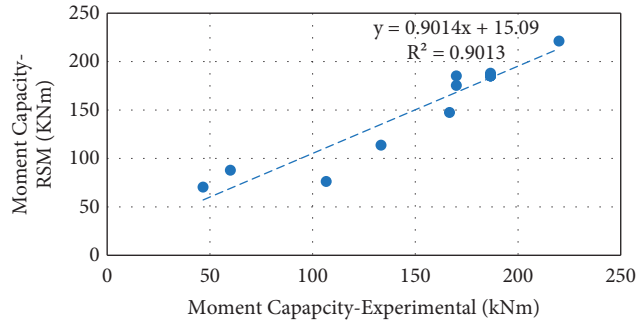


FIGURE 6: Predicted and actual values of moment capacity.

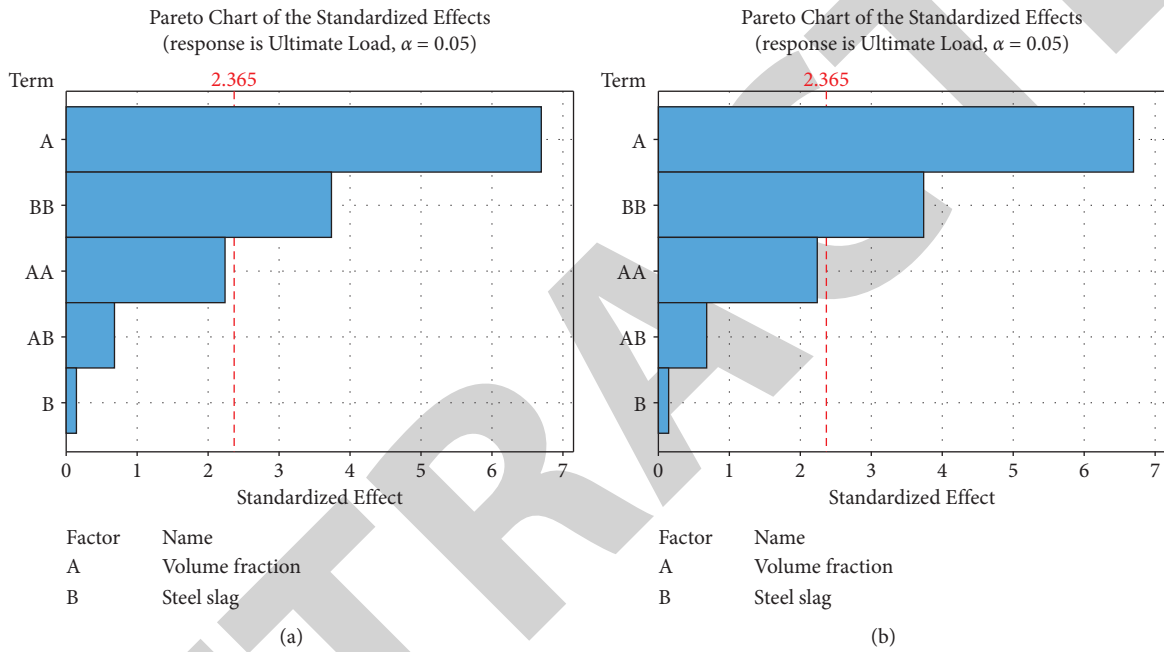


FIGURE 7: Pareto chart. (a) Ultimate load; (b) moment capacity.

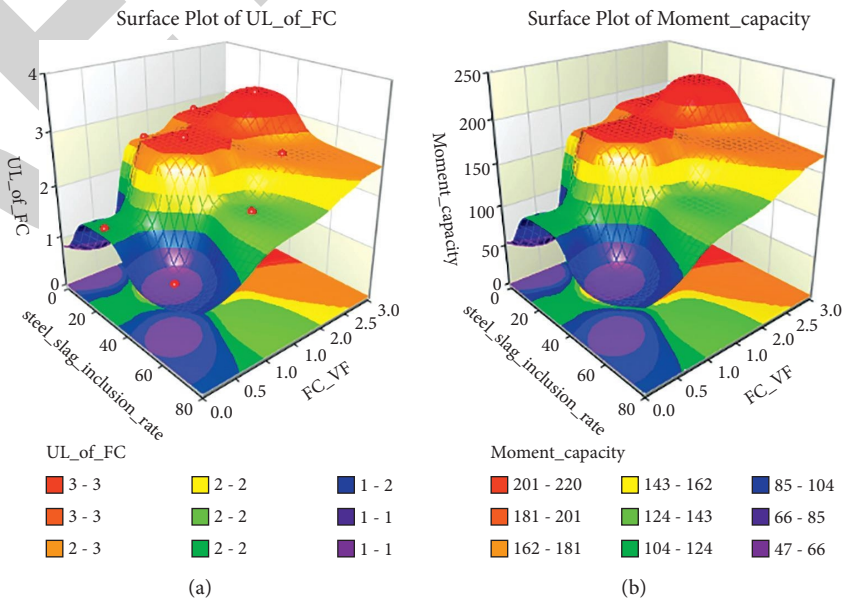


FIGURE 8: 3D Surface plot for: (a) ultimate load; (b) moment capacity.

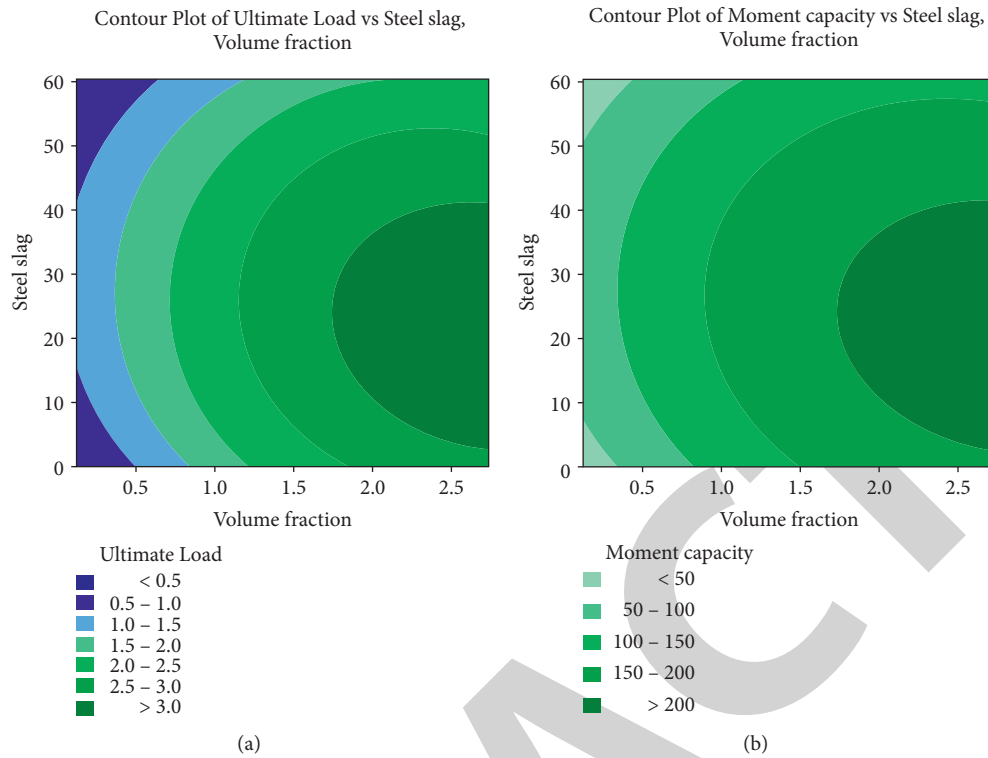


FIGURE 9: Contour Plot: (a) ultimate load; (b) moment capacity.

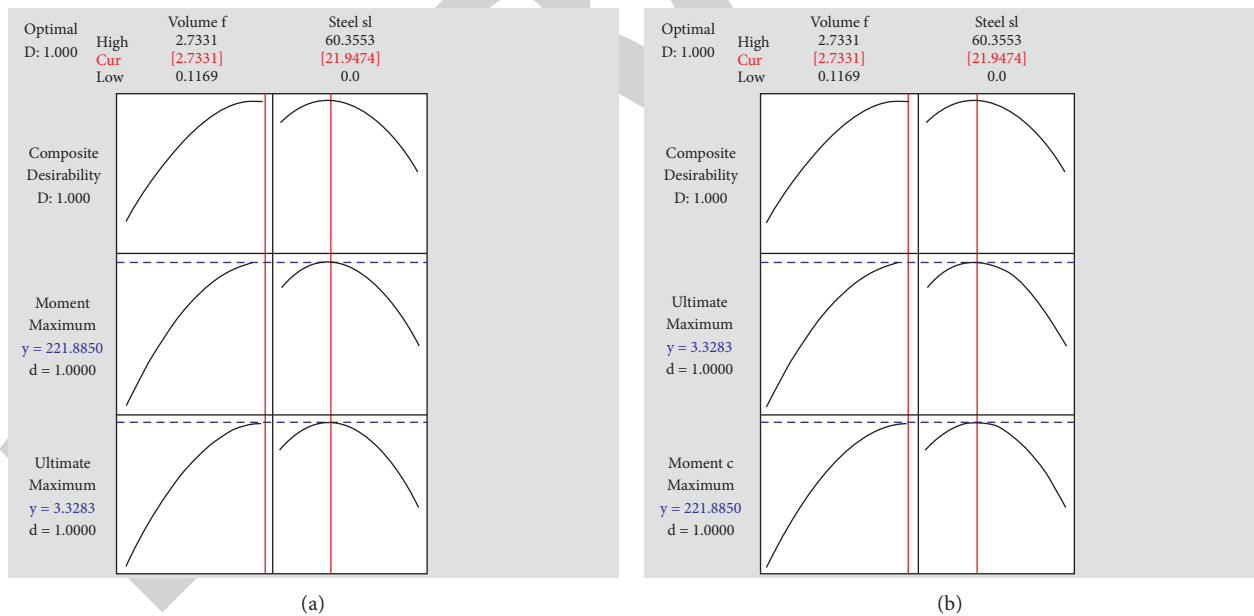


FIGURE 10: Response optimisation plots: (a) ultimate load; (b) moment capacity.

TABLE 6: Confirmation of Test results.

Properties	Volume fraction	Steel slag	Predicted result RSM	Confirmation results
Ultimate load	2.73	21.95	3.46	3.31
Moment capacity	2.73	21.95	221.73	220.56

6. Conclusions

In this present study, optimisation of ultimate load and moment capacity of ferrocement composites with different volume fractions and steel slag using the central composites method of RSM is made and the conclusions arrived are given below:

- (i) The addition of steel slag has moderately enhanced the ultimate load and moment capacity of ferrocement laminates. But for higher levels of steel slag content the ultimate load and moment capacity reduces.
- (ii) Ferrocement with volume fraction of 2.73% and 25% of steel slag by weight fraction of fine aggregate has improved the ultimate load and moment capacity of ferrocement laminates
- (iii) A total of two responses ultimate load and moment capacity were considered in the central composite method of RSM examination, the influences and the level of each outcome were 2 and 2, respectively.
- (iv) The ANNOVA results show that the most contributing factor for ultimate load and moment capacity is the volume fraction of mesh reinforcement.
- (v) The model established using regression analysis to predict ultimate load and moment capacity shows that forecast values go in hand with the experimental results.
- (vi) The ANOVA and Pareto chart examination showed that the regression models for ultimate load and moment capacity are highly significant. The mathematical outputs of the models are of high precision as the p value of the models was less than 0.005. The most substantial factor for ultimate load and moment capacity was found to be volume fraction (X_1).

Data Availability

The data used to support the findings of this study are included in the article.

Conflicts of Interest

The authors declare that there are no conflicts of interest regarding the publication of this article.

References

- [1] FMC, *Ferrocement Model Code. Building Code Recommendations for the Ferrocement*, International Ferrocement Society, Tavares, FL, USA, IFS 10-01 2001, 2001.
- [2] A. E. Naaman, *Ferrocement and Laminated Cementitious Composites*, Techno Press 3000, Michigan, USA, 2000.
- [3] J. C. Babu, M. S. Kumar, P. Jayagopal et al., "IoT-based intelligent system for internal crack detection in building blocks," *Journal of Nanomaterials*, vol. 2022, Article ID 3947760, 8 pages, 2022.
- [4] S. Sebastin, M. F. David, A. Karthick et al., "Investigation on mechanical and durability performance of reinforced concrete containing red soil as alternate for M-sand," *Journal of Nanomaterials*, vol. 2022, Article ID 5404416, 15 pages, 2022.
- [5] H. Naderpour, Danial Rezazadeh Eidgahee, and A. PouyanFakharian, R. Hossein and S. M. Kalantari, A new proposed approach for moment capacity estimation of ferrocement members using Group Method of Data Handling, Engineering Science and Technology," *An International Journal*, vol. 23, pp. 382–391, 2020.
- [6] S. Jayaprakash, Jegatheeswaran Dhanapal Vivek Deivasigamani, and G. Elias, "Flexural behaviour of chicken mesh ferrocement laminates with partial replacement of fine aggregate by steel slag," *Advances in Material Science and Engineering*, vol. 219 pages, 2021.
- [7] A. Ismail, "Estimating moment capacity of ferrocement members using self-evolving network," *Frontiers of Structural and Civil Engineering*, vol. 13, no. 4, pp. 926–936, 2019.
- [8] K. Sankar and D. Shoba Rajkumar, "Experimental investigation on different high rich cement mortar for ferrocement application," *Materials Today Proceedings*, vol. 1-7, 2019.
- [9] C. Samson Jerold Samuel and A. Ramesh, "Investigation on microstructure and tensile behaviour of stir cast LM13 Aluminium alloy reinforced with copper coated short steel fibres using response surface methodology," *Tran Indian Inst Met*, vol. 71, no. 9, pp. 2221–2230, 2018.
- [10] A. Hammoudi, K. Moussaceb, C. Belebchouche, and F. Dahmoune, "Comparison of artificial neural network (ANN) and response surface methodology (RSM) prediction in compressive strength of recycled concrete aggregates," *Construction and Building Materials*, vol. 209, pp. 425–436, 2019.
- [11] Y. Moodi, SR. Mousavi, A. Ghavidel, R. S. Mohammad, and R. Mohsen, "Using response surface methodology and providing a modified model using whale algorithm for estimating the compressive strength of columns confined with FRP sheets," *Construction and Building Materials Mater*, vol. 183, pp. 163–170, 2018.
- [12] C. Samson Jerold Samuel, A. Ramesh, NT. Arun prasad, and S. Hari Shankar, "Dry sliding wear characterization of squeeze cast LM13/FeCu composite using response surface methodology," *China Foundry*, vol. 14, no. 6, pp. 525–533, 2017.
- [13] M. Aziminehad, M. Mahdikhani, and M. Mahdi Memarpour, "RSM-based modelling and optimization of self-consolidating mortar to predict acceptable ranges of rheological properties," *Construction and Building Materials*, vol. 189, pp. 1200–1213, 2018.
- [14] T. Kalman Sipo and P. Parse, "Empirical formulation of ferrocement members moment capacity using artificial neural networks," *Journal of Soft computing in Civil Engineering*, vol. 4, no. 2, pp. 111–126, 2020.
- [15] A. Madadi, H. Eskandari-Naddaf, R. Shadnia, and L. Zhang, "Characterization of ferrocement slab panels containing lightweight expanded clay aggregate using digital image correlation technique," *Construction and Building Materials*, vol. 180, pp. 464–476, 2018.
- [16] J. ChithambaramS and S. Kumar, "Flexural behaviour of bamboo based ferrocement slab panels with flyash," *Construction and Building Materials*, vol. 134, pp. 641–648, 2017.
- [17] K. Zhang and Q. Sun, "The use of Wire Mesh-Polyurethane Cement (WM-PUC) composite to strengthen RC T-beams under flexur," *Journal of Building Engineering*, vol. 15, pp. 122–136, 2018.
- [18] W. Wang, Y. Cheng, and G. Tan, "Design Optimization of SBS-modified asphalt mixture reinforced with eco-friendly

Research Article

Influence of Planetary Ball Mill Parameters on Powder Flowability of AlSi10Mg with Niobium Carbide Using Central Composite Design (CCD)

Raj Mohan R ¹, Venkatraman R ¹, Raghuraman S ¹, Manoj Kumar P ²,
Rajneesh Sharma ³, Ankit ⁴, Atul Sarojwal ⁵ and Rajkumar S ⁶

¹School of Mechanical Engineering, SASTRA Deemed to Be University, Thanjavur 613401, Tamil Nadu, India

²Department of Mechanical Engineering, KPR Institute of Engineering and Technology, Coimbatore 641407, Tamil Nadu, India

³Department of Civil Engineering, Government Engineering College, Jhalawar 326023, Rajasthan, India

⁴Department of Mechanical Engineering, Government Engineering College, Jhalawar 326023, Rajasthan, India

⁵Department of Electrical Engineering, FET, MJP Rohilkhand University, Bareilly 243006, UP, India

⁶Department of Mechanical Engineering, Faculty of Manufacturing, Institute of Technology, Hawassa University, Hawassa, Ethiopia

Correspondence should be addressed to Rajkumar S; rajkumar@hu.edu.et

Received 13 April 2022; Accepted 7 July 2022; Published 3 August 2022

Academic Editor: Adel Mohamed

Copyright © 2022 Raj Mohan R et al. This is an open access article distributed under the Creative Commons Attribution License, which permits unrestricted use, distribution, and reproduction in any medium, provided the original work is properly cited.

The hypoeutectic aluminum alloy (AlSi10Mg) is a well-known candidate material used predominantly for its processability and inherent characteristics in metal-based additive manufacturing. Besides, transition metal carbide, such as niobium carbide (NbC), is added to the AlSi10Mg, enhancing its mechanical properties and preferably its wear resistance to the matrix. However, in additive manufacturing, the mixed powder's flowability is a prerequisite for determining the final properties of the specimens. In this study, mixed powder flowability analysis was carried out through the regular mixing of AlSi10Mg with a varying weight percentage of NbC conducted in the planetary ball mill with different time, speed, and NbC composition following the Central Composite Design (CCD), with a total of 20 experiments. Here, regular mixing was preferred to retain the morphology of the AlSi10Mg (spherical shape) instead of ball milling, which contributes to the degradation of the powder's shape and size. Finally, based on the combined analysis of apparent density (AD), tapped density (TD), and static angle of repose (SAoR), the flowability characteristics of the mixed powders (AlSi10Mg + X % NbC) were evaluated. The optimum combination (AlSi10Mg + X% NbC) was attained based on the composite desirability criteria.

1. Introduction

Metal-based additive manufacturing is an emerging technology that produces components within the stipulated period and achieves high dimensional accuracy [1]. Generally, this technology employs only a specified powder category, such as atomized particles, depending on the manufacturer's specification. The atomized powder properties must be addressed based on the processability criterion to ensure the component's print quality [2]. The properties of the powder comprise the flowability, the

density of the powder (apparent density and tapped density), particle shape (morphology), the powder synthesis process, and the particle size distribution (PSD) that affect the building of the powder layer on the platform. The flowability of the powder should be adequate for an effective additive manufacturing process [3]. In processing aluminum alloys by additive manufacturing, the powder's morphology and size distribution play a decisive role in ensuring the material's packing density [4]. The particle shape significantly influences good flowability than the size distribution [5]. Ball milling is widely preferred for aluminum-based matrix

composites to mix/blend the two different sizes and shapes of powders (matrix + reinforcement) in varying volumes or weight percentages following other optimization techniques.

Moreover, the ball mill's input parameters substantially affect the blended powder flow properties [6–14]. For the application of greater hardness, niobium carbide (NbC) is preferred among other transition metal carbides (TMC) due to its higher bulk modulus and incorporating an irregular-shaped carbide as reinforcement improves the wear resistance of the matrix element [15, 16]. The mixing of two different powders (metals as matrix and ceramic as reinforcement) with various morphologies was possible to process through casting [17] and powder metallurgy [18] routes for powder preparation. Compared to the previous routes, ceramic reinforcements (other TMCs) in the Al-based matrix showed remarkable mechanical properties such as high hardness and high wear resistance [19] when compared to the base alloy through the selective laser melting (SLM) process and are suitable for tribological applications. Furthermore, compared to traditional approaches such as casting and powder metallurgy, composite fabrication via additive manufacturing has benefits in terms of design, freedom, and the ability to manufacture complicated designs [20]. However, it is challenging because of the additive manufacturing processability [21].

From a critical review of the literature, it was noted that the optimization of powder flow characteristics in the combination of hypoeutectic aluminum alloy (AlSi10Mg) and group VB transition metal carbide (NbC) was not explored much in the scope of additive manufacturing. Therefore, evaluating the mixed powder characteristics of AlSi10Mg (spherical) and NbC (aggregate irregular) with varying weight percentages is required before being fed into the processing window of additive manufacturing. The objective of the work is to investigate the powder flowability characteristics of AlSi10Mg with the addition of NbC based on apparent density (AD), tapped density (TD), and static angle of repose (SAoR) values through regular mixing in a planetary ball mill following the central composite design approach. At the same time, the Hausner's Ratio (HR) and the Carr Index (CI) values resulted from the apparent and tapped densities of the mixed powder.

2. Materials and Methods

The AlSi10Mg powder (Si–10; Mg–0.35; Al–Balance; Supplier: Carpenter Additive, UK) of a mean particle size of 41.79 microns and NbC powder (99% Pure; Supplier: Alfa Aesar, UK) of a mean particle size of 12.05 microns were used. The AlSi10Mg was considered a matrix element in the experimental study, whereas the NbC was taken as particulate ceramic reinforcement. The morphology of procured AlSi10Mg with a spherical shape and NbC with an aggregate irregular shape was observed using a scanning electron microscope (Vega3 TESCAN) analysis, as shown in Figures 1(a) and 1(b). The X-ray photoelectron spectroscopy (Thermo Fisher) analysis was carried out for procured powders, as shown in Figure 2, and no impurities were identified in either of the powder samples. Two powders

were regularly mixed using a planetary ball mill with a single jar holder (VB Ceramic Consultants, India). For maintaining the spherical shape of the AlSi10Mg, the balls are not used during regular mixing. Using MINITAB (Version-18.0), the central composite design (CCD) was preferred in this investigation to analyze and optimize the planetary ball mill's input parameters to ensure the effects of extreme levels of factors involved. The three main input parameters for regular mixing using a planetary ball mill are time (hours), speed (RPM), and NbC composition (% weight), which play a vital role in predicting powder flowability. The input parameters and levels are shown in Table 1. Based on the three input factors and five levels of each factor, 20 sets of experiments were designed and included in Table 2. The scanning electron microscope (SEM) samples examined the morphology change of the master alloy and ensured the distribution of reinforcement in the matrix. The powder flow characteristics study was performed based on apparent density: ASTM B 212, tapped density: ASTM B 527 [22], static angle of repose: ASTM B213 [23], Hausner's Ratio: ASTM D7481-09, and Carr Index: ASTM D6393-14 [24].

3. Results and Discussion

3.1. Analysis of CCD Experiments. The CCD was employed to predict the influence of the extreme limits of the input parameters such as time, speed, and composition on the output responses. Also, CCD was used for developing the mathematical model for the responses such as apparent density, tapped density, and static angle of repose. The apparent density and tapped density values were obtained by the Hall flowmeter method and mechanical tapping 50 times, respectively, conforming to the ASTM standards. Generally, the lower values of apparent and tapped densities exhibit the poor flowability of the powders. For the flowability indication of mixed powder, the HR and CI values were attained using (1) and (2). For better flowability, the lower Hausner's Ratio and Carr Index values were preferred. The static angle of repose of the mixed powder was attained using (3) based on the piling diameter and height, followed by the fixed cone height approach. The static angle of repose was used to assess the mixed powder's internal condition, such as cohesiveness or friction between the particles. More cohesiveness leads to an increased static angle of repose and affects the flow of the mixed powder. Table 3 shows the data of output responses based on the CCD experiments. In experimental analysis, the CCD experiments were classified into three categories, namely, center-based (E5, E6, E11, E18, E19, and E20), extreme-based (E3, E4, E9, E13, E16, and E17), and factor-based (E1, E2, E7, E8, E10, E12, E14, and E15). From Table 3, it was noted that experiments E4 and E9 show the worst flow characteristics based on the results of the output responses due to the mixing in extreme conditions like a more extended time (6.02 hours) and higher NbC composition (11.043% weight) under the rotational speed of 150 RPM.

Conversely, E8, E10, E12, E13, E14, and E15 show good flowability of mixed powders based on the lower HR, CI, and SAoR. The remaining experiments, E1, E2, E3, E5, E6,

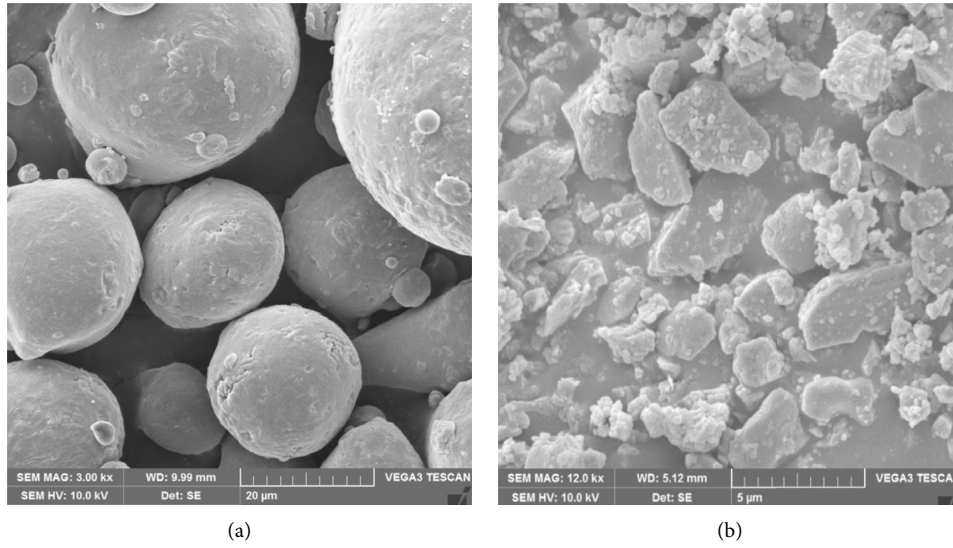


FIGURE 1: Morphology of (a) AlSi10Mg and (b) NbC.

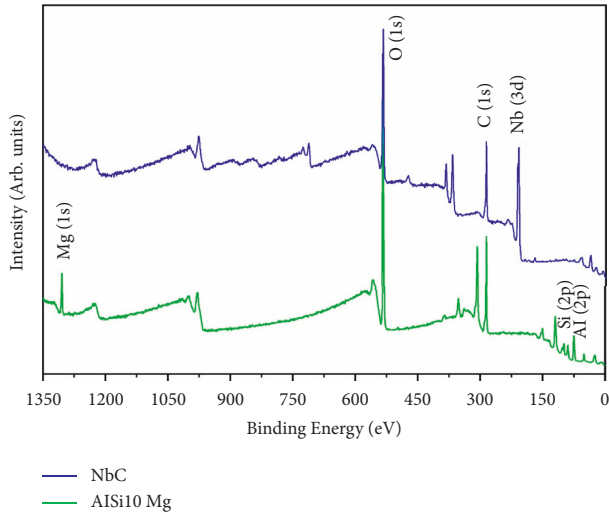


FIGURE 2: XPS spectra of AlSi10Mg and NbC.

TABLE 1: Input parameters and their levels for regular mixing.

Input parameters	Levels				
	$-\alpha$	-1	0	1	$+\alpha$
Time (hours): A	0.98	2	3.5	5	6.02
Speed (RPM): B	65.95	100	150	200	234.05
NbC composition (% weight): C	0.957	3	6	9	11.043

E7, E11, E16, E17, E18, E19, and E20, exhibit fair flow characteristics. From the observations, irrespective of varying NbC composition, it was clear that the factor-based experiments yielded a good flow for the mixed powders

TABLE 2: CCD experiment design with factors.

Experiment no.	A	B	C
E1	2	200	3
E2	5	200	9
E3	0.98	150	6
E4	3.5	150	11.043
E5	3.5	150	6
E6	3.5	150	6
E7	5	200	3
E8	2	100	3
E9	6.02	150	6
E10	5	100	9
E11	3.5	150	6
E12	5	100	3
E13	3.5	234.05	6
E14	2	200	9
E15	2	100	9
E16	3.5	65.95	6
E17	3.5	150	0.957
E18	3.5	150	6
E19	3.5	150	6
E20	3.5	150	6

owing to the proper set of input parameters, except for E1, E2, and E7. These experiments also exhibit good HR and CI, but the angle of repose is high due to the nonuniform dispersion of NbC particles, affecting the flow and inducing a frictional effect between the reinforcement and matrix. Moreover, the center-based and extreme-based experiments do not yield satisfactory results, except for experiment E13, because the mixing occurs at a higher speed of 234.05 RPM.

TABLE 3: Output responses based on CCD-based experiments.

Experiment no.	Apparant density (g/cc)	Tapped density (g/cc)	Static angle of repose (Radian)	Hausner's Ratio (no unit)>	Carr Index (%)
E1	1.140	1.359	0.547	1.19	16.14
E2	1.270	1.529	0.567	1.20	16.94
E3	1.258	1.522	0.531	1.21	17.33
E4	1.284	1.608	0.597	1.25	20.15
E5	1.251	1.545	0.510	1.23	19.02
E6	1.251	1.545	0.540	1.23	19.02
E7	1.161	1.375	0.516	1.18	15.58
E8	1.234	1.470	0.479	1.19	16.05
E9	1.242	1.603	0.597	1.29	22.53
E10	1.292	1.531	0.486	1.18	15.59
E11	1.251	1.555	0.528	1.24	19.52
E12	1.276	1.507	0.440	1.18	15.33
E13	1.187	1.334	0.489	1.12	11.04
E14	1.280	1.486	0.488	1.16	13.89
E15	1.333	1.537	0.448	1.15	13.28
E16	1.310	1.601	0.389	1.22	18.18
E17	1.153	1.409	0.542	1.22	18.17
E18	1.251	1.545	0.528	1.23	19.02
E19	1.251	1.545	0.528	1.23	19.02
E20	1.251	1.545	0.528	1.23	19.02

$$\text{Hausner's Ratio (HR)} = \frac{\text{Tapped Density}}{\text{Apparant Density}}, \quad (1)$$

$$\text{Carr Index (CI)} = \frac{\text{Tapped Density} - \text{Apparant Density}}{\text{Tapped Density}} \times 100, \quad (2)$$

$$\text{Static Angle of Repose (SAoR), } \tan \theta = \frac{2 \times \text{Height of the Piling (H in mm)}}{\text{Base Diameter of the Piling (D in mm)}}, \quad (3)$$

The center-based, extreme-based, and factor-based scanning electron microscope (SEM) images are shown in Figures 3–5, respectively. The SEM images of the mixed powder under various input parameters were used to ensure the morphology of the AlSi10Mg with NbC and the distribution of the reinforcement (NbC) in the matrix (AlSi10Mg). Figures 3–5 depict that the AlSi10Mg morphology is not modified, and NbC particles' presence was observed. Here, the yellow circle is used to indicate the presence of NbC particles in the matrix.

3.2. Percentage Contribution of Input Parameters for Responses. Table 4 shows the statistical values based on the full quadratic model. The values depict that the model is adequate for analysis and further experimentation. If the p value and F -value are less than 0.05 and greater than 4, respectively, at a 95 percent confidence level, the proposed model is significant, and the corresponding input parameter is taken into account for the output response. The model's R square value for all responses was greater than 90 percent, which reveals that the model could explore 90 percent of the possible changes in the

output responses. The model can significantly predict the process if the R square and adjusted R square values are greater than 80 percent. The input parameters, such as speed and NbC composition, contribute more substantially to the responses, such as apparent density and tapped density. The most vital input parameter affecting the static angle of repose is speed. Also, the interaction of time and NbC composition contributes to the static angle of repose.

3.3. Validation of Regression Equation. The regression equations (4)–(6) were used to predict output responses such as apparent density, tapped density, and static angle of repose by including quadratic terms of linear, square, and two-way interaction of input parameters. The residual value was obtained from the difference between experimented and predicted data. If the residual values are small, the proposed regression equations are accurate. Table 5 shows the residual values for the responses, depicting that the fitted data are close to the experimented data. So, the proposed regression equations have verified the adequacy of the full quadratic model.

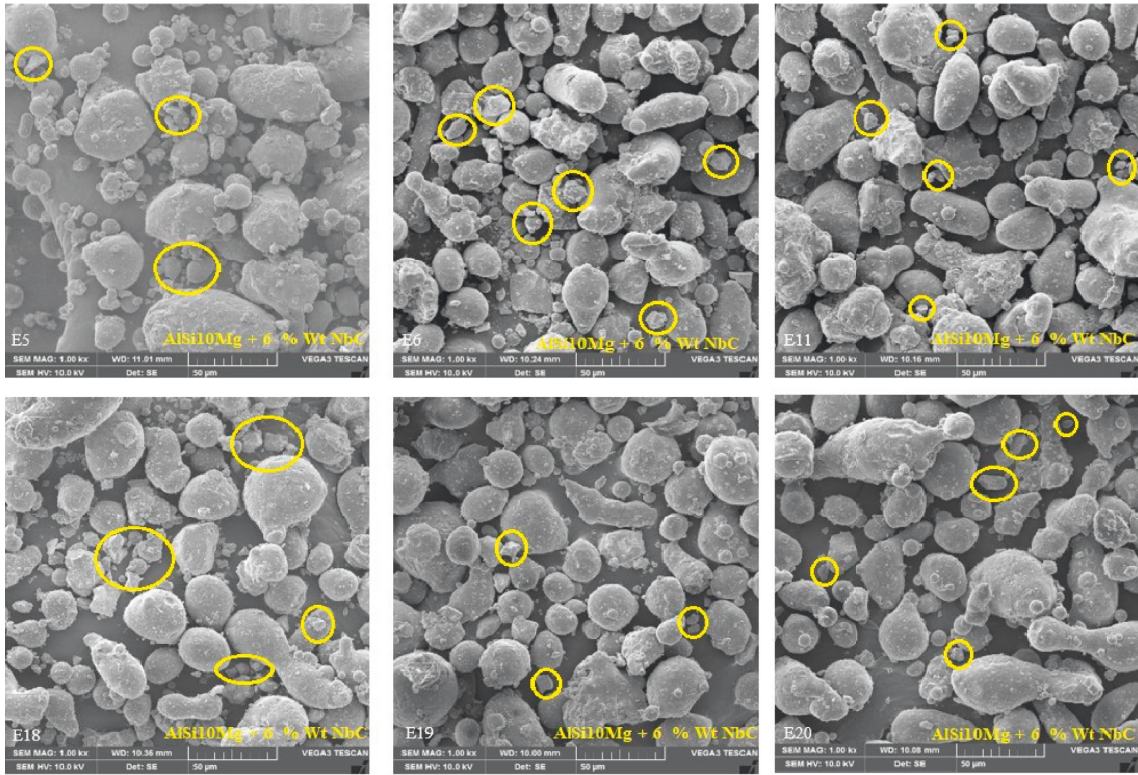


FIGURE 3: SEM images of center-based experiments.

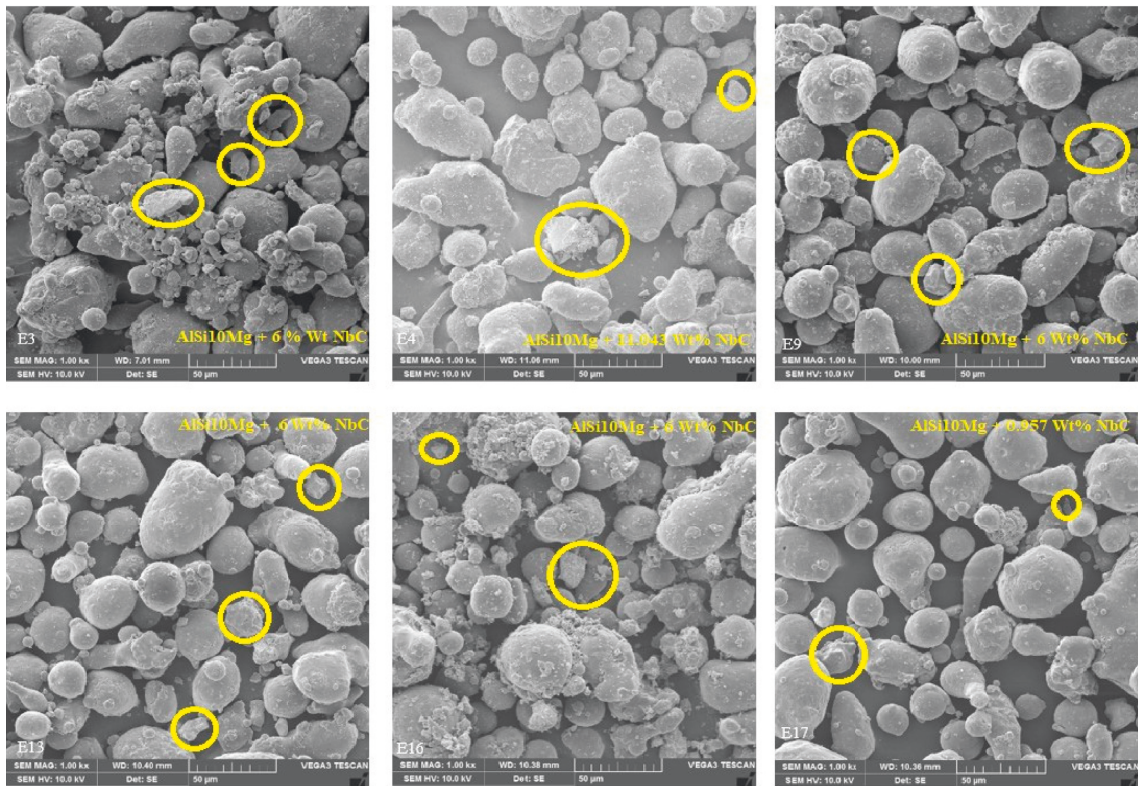


FIGURE 4: SEM images of extreme-based experiments.

TABLE 5: Validation of regression equation.

Run order	Predicted (P) vs. experimented (E)								
	Apparent density (g/cc)			Tapped density (g/cc)			Static angle of repose (radian)		
	<i>p</i>	<i>E</i>	Residue	<i>p</i>	<i>E</i>	Residue	<i>p</i>	<i>E</i>	Residue
E1	1.134	1.140	0.006	1.337	1.359	0.022	0.540	0.547	0.007
E2	1.254	1.270	0.016	1.528	1.529	0.001	0.584	0.567	-0.017
E3	1.258	1.258	0.000	1.514	1.522	0.008	0.529	0.531	0.002
E4	1.296	1.284	-0.012	1.575	1.608	0.033	0.566	0.597	0.031
E5	1.251	1.251	0.000	1.548	1.545	-0.003	0.528	0.510	-0.018
E6	1.251	1.251	0.000	1.548	1.545	-0.003	0.528	0.540	0.012
E7	1.163	1.161	-0.002	1.381	1.375	-0.006	0.529	0.516	-0.013
E8	1.242	1.234	-0.008	1.500	1.470	-0.030	0.483	0.479	-0.004
E9	1.254	1.242	-0.012	1.570	1.603	0.033	0.568	0.597	0.029
E10	1.290	1.292	0.002	1.583	1.531	-0.052	0.515	0.486	-0.029
E11	1.251	1.251	0.000	1.548	1.555	0.007	0.528	0.528	0.000
E12	1.266	1.276	0.010	1.531	1.507	-0.024	0.447	0.440	-0.007
E13	1.193	1.187	-0.006	1.355	1.334	-0.021	0.477	0.489	0.012
E14	1.282	1.280	-0.002	1.492	1.486	-0.006	0.502	0.488	-0.014
E15	1.323	1.333	0.010	1.560	1.537	-0.023	0.457	0.448	-0.009
E16	1.315	1.310	-0.005	1.539	1.601	0.062	0.370	0.389	0.019
E17	1.152	1.153	0.001	1.401	1.409	0.008	0.541	0.542	0.001
E18	1.251	1.251	0.000	1.548	1.545	-0.003	0.528	0.528	0.000
E19	1.251	1.251	0.000	1.548	1.545	-0.003	0.528	0.528	0.000
E20	1.251	1.251	0.000	1.548	1.545	-0.003	0.528	0.528	0.000

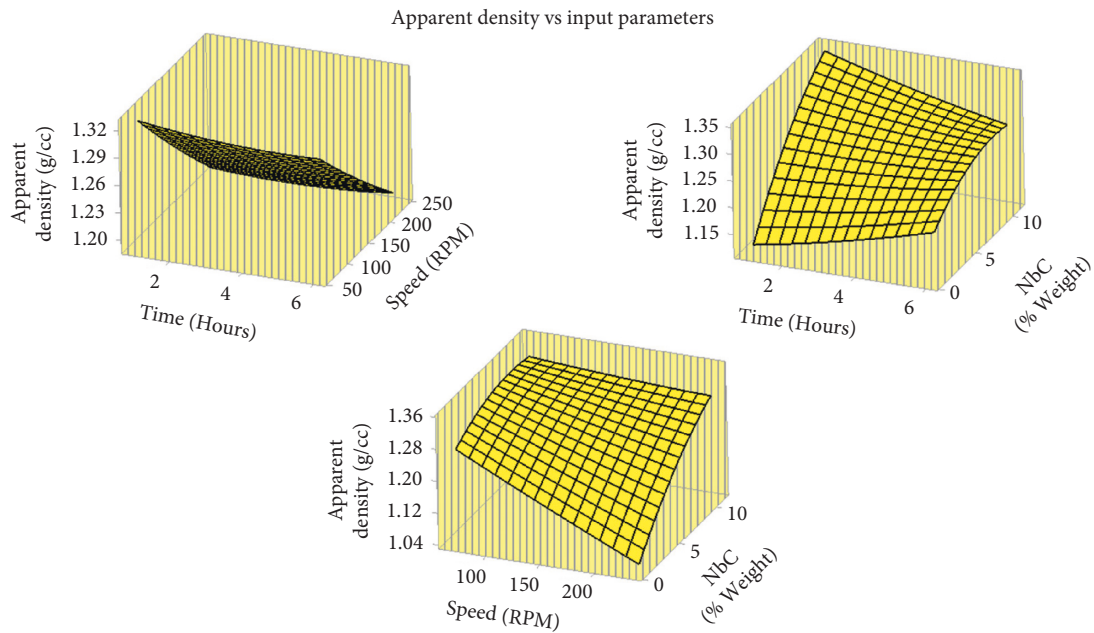


FIGURE 6: Surface plots for apparent density.

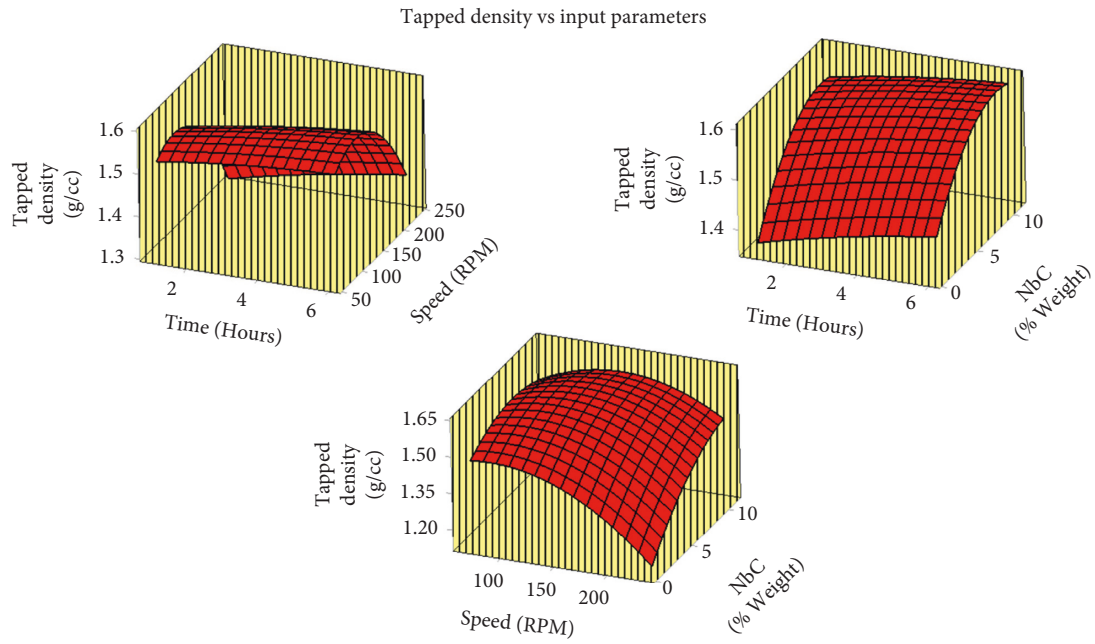


FIGURE 7: Surface plots for tapped density.

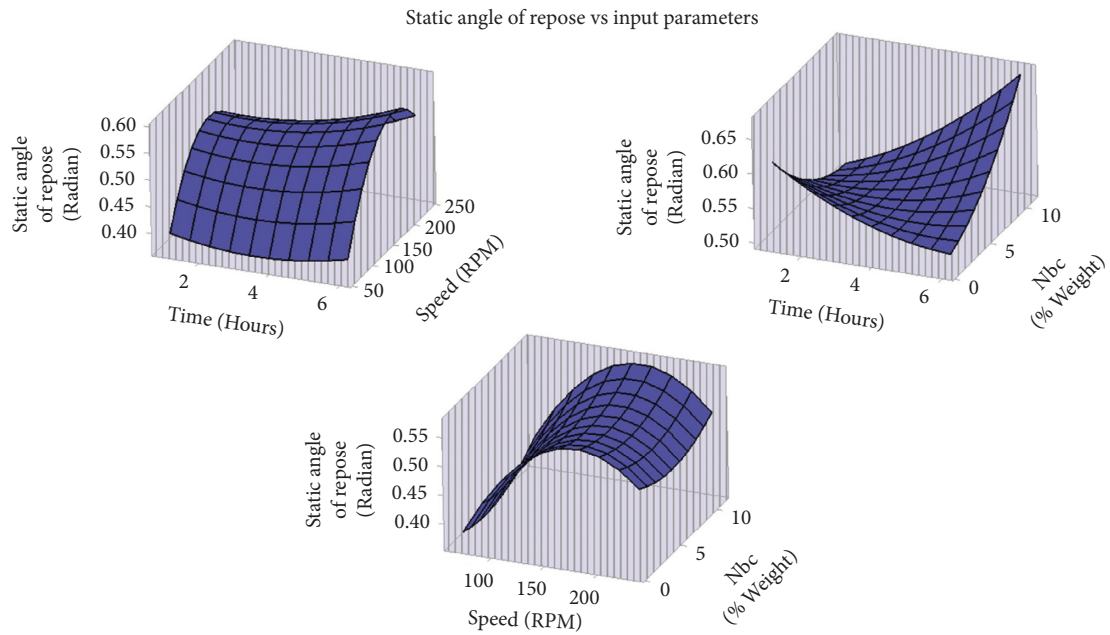


FIGURE 8: Surface plots for the static angle of repose.

TABLE 6: Criteria for composite desirability function.

Output response	Goal/objective	Lower value	Target	Upper value	Importance	Weight
Apparent density	Maximum	1.3340	1.6083	—	1	1
Tapped density	Maximum	1.1396	1.3330	—	1	1
Static angle of repose	Minimum	—	0.3892	0.597	1	1

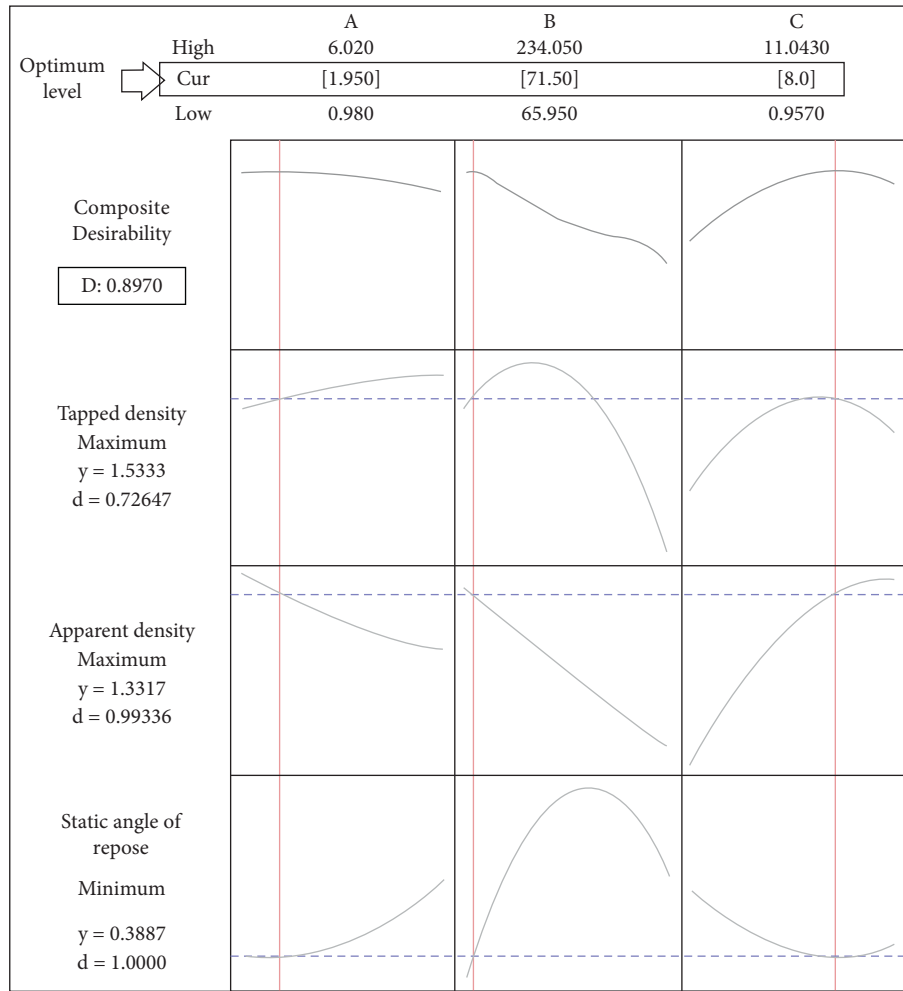


FIGURE 9: Composite desirability plot based on multiple responses.

$$\begin{aligned} \text{Apparent Density} = & 1.2995 + 0.0105 A - 0.00157 B + 0.0212 C + 0.00074 AA + 0.000000 BB - 0.00105 CC \\ & + 0.000017 AB - 0.00316 AC + 0.000112 BC, \end{aligned} \tag{4}$$

$$\begin{aligned} \text{Tapped Density} = & 1.3080 + 0.0135 A + 0.00210 B + 0.0234 C - 0.00095 AA - 0.000014 BB - 0.00236 CC \\ & + 0.000047 AB - 0.00046 AC + 0.000158 BC, \end{aligned} \tag{5}$$

$$\begin{aligned} \text{Static Angle of Repose} = & 0.2680 - 0.0579 A - 0.00491 B - 0.0249 C + 0.00371 AA - 0.000015 BB + 0.01007 CC \\ & + 0.000081 AB + 0.00519 AC - 0.000019 BC \end{aligned} \tag{6}$$

3.4. *Surface Plots for the Output Responses.* Based on the proposed and verified model, the 3D surface plots for apparent density, tapped density, and static angle of repose are generated and shown in Figures 6–8, respectively. It displays the influence of time versus speed, time versus NbC composition, and speed versus NbC composition on different output responses with fixed input parameters at the zero (coded) level. It is observed that the apparent density and tapped density decreased as the speed increased. In contrast, both the densities were increased as the NbC composition increased. At the lower mixing speed (less than 100 RPM) with a higher weight percentage of NbC, the apparent and

tapped density values were high. So, the HR and CI values were high at the low-speed mixing. The static angle of repose decreases with decreasing speed. Irrespective of increasing the NbC composition, the value of the static angle of repose was minimum at a low speed of less than 100 RPM. Finally, time plays a less significant role in deciding the change in output responses.

3.5. *Composite Desirability and Validation.* The composite desirability function can achieve multiple response objectives/goals. Here, the objective is to attain a maximum apparent and

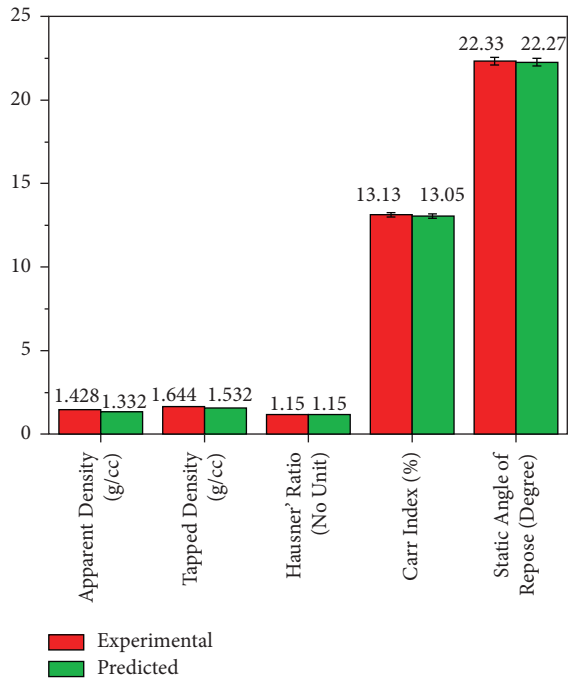


FIGURE 10: Comparison between experimental and predicted values for optimum conditions.

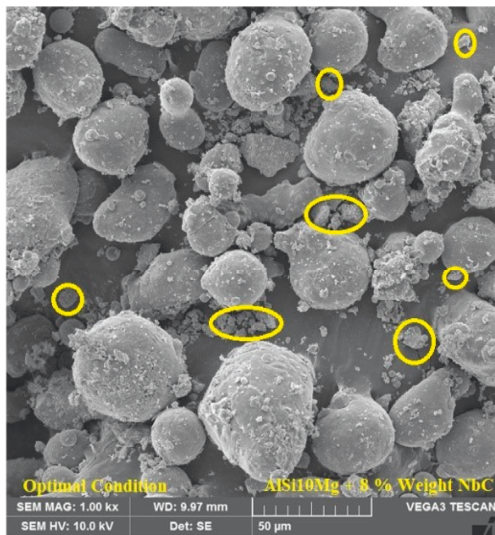


FIGURE 11: SEM image for the optimum combination of AlSi10Mg + 8% weight of NbC.

tapped densities with the minimum static angle of repose. The maximum apparent density ensures that the mixed powders are not entirely irregular in morphology, introduce smaller particles (NbC) between the AlSi10Mg particles, and have low pores in the initial packed density. The particles' cohesiveness was controlled, establishing good flow to the mixed powder at maximum tapped density criteria. Based on the maximum condition of both densities, low HR and CI were attained. These values ensure good flowability characteristics. Finally, the minimum static angle of repose confirms the low cohesiveness and minimum frictional effect during the powder

flow. The static angle of repose is inversely proportional to the flowability of the mixed powder. Table 6 shows the goal of the output responses with importance and weight, along with constraint values.

Figure 9 displays the optimal results with a composite desirability limit to address the multiple objective output response by pulling out the higher and lower point from the 3D surface plot concerning the defined objective. The optimum condition is as follows: time = 1.95 hours, speed = 71.50 RPM, NbC composition = 8% weight. The predicted values of apparent density, tapped density, and static angle of repose are 1.3317 g/cc, 1.5333 g/cc, and 0.3887 radians (22.17 degrees) with composite desirability of 0.897.

As shown in Figure 10, the validation experiment was carried out under optimized conditions for the confirmatory purpose, and the experimental data were compared with predicted data, as shown in Figure 10. From Figure 11, it was observed that there was no change in the matrix (AlSi10Mg) morphology and tiny satellites on the surface of the matrix.

4. Conclusion

In this experimental investigation, the CCD was employed to predict the processing conditions for regular mixing of AlSi10Mg and NbC. From the experimental analysis, the following points can be observed:

- (1) The factor-based experiments show promising results based on flowability characteristics when compared to center-based and extreme-based experiments
- (2) Based on the SEM images, the morphology of the matrix element (AlSi10Mg) had not been changed after being mixed with varying percentages of NbC at a different set of parameters, and proper distribution of NbC was observed.
- (3) The apparent and tapped density ratio was insufficient for predicting the flow of mixed powder. Another response is also required to assess the flow characteristics. So, the static angle of repose was employed to predict the mixed powder's cohesiveness despite its low HR and CI values. The undesired flow characteristics were observed at a high percentage of NbC and the extended mixing time.
- (4) The optimum condition of input parameters reveals that the low-speed mixing was preferable to achieve maximum apparent and tapped densities with the minimum static angle of repose.
- (5) Finally, the optimized combination of mixed powder (AlSi10Mg + 8% weight of NbC) was attained, showing good flowability characteristics. Furthermore, it satisfies the processability criteria of additive manufacturing.

Data Availability

The data used to support the findings of this study are included in the article.

Conflicts of Interest

The authors declare that there are no conflicts of interest regarding the publication of this paper.

Acknowledgments

This work was funded by the SASTRA Deemed to be University under Prof. T. R. Rajagopalan (TRR) Research Fund.

References

- [1] G. Marchese, A. Aversa, M. Lorusso et al., "Development and characterisation of aluminium matrix nanocomposites AlSi10Mg/MgAl₂O₄ by laser powder bed fusion," *Metals*, vol. 8, no. 3, p. 175, 2018.
- [2] J. Zegzulka, D. Gelnar, L. Jezerska, R. Prokes, and J. Rozbroj, "Characterization and flowability methods for metal powders," *Scientific Reports*, vol. 10, no. 1, Article ID 21004, 2020.
- [3] A. B. Spierings, M. Voegtlin, T. Bauer, and K. Wegener, "Powder flowability characterisation methodology for powder-bed-based metal additive manufacturing," *Progress in Additive Manufacturing*, vol. 1, no. 1-2, pp. 9–20, 2016.
- [4] R. Raj Mohan, R. Venkatraman, S. Raghuraman et al., "Processing of aluminium-silicon alloy with metal carbide as reinforcement through powder-based additive manufacturing: a critical study," *Scanning*, vol. 2022, pp. 1–14, 2022.
- [5] K. Riener, N. Albrecht, S. Ziegelmeier et al., "Influence of particle size distribution and morphology on the properties of the powder feedstock as well as of AlSi10Mg parts produced by laser powder bed fusion (LPBF)," *Additive Manufacturing*, vol. 34, Article ID 101286, 2020.
- [6] P. Ashwath and M. A. Xavior, "The effect of ball milling & reinforcement percentage on sintered samples of aluminium alloy metal matrix composites," *Procedia Engineering*, vol. 97, pp. 1027–1032, 2014.
- [7] L. Kollo, M. Leparoux, C. R. Bradbury, C. Jäggi, E. Carreño-Morelli, and M. Rodríguez-Arbaizar, "Investigation of planetary milling for nano-silicon carbide reinforced aluminium metal matrix composites," *Journal of Alloys and Compounds*, vol. 489, no. 2, pp. 394–400, 2010.
- [8] Y. Afkham, R. A. Khosroshahi, R. Kheirifard, R. T. Mousavian, and D. Brabazon, "Microstructure and morphological study of ball-milled metal matrix nanocomposites," *The Physics of Metals and Metallography*, vol. 118, no. 8, pp. 749–758, 2017.
- [9] Q. Han, R. Setchi, and S. L. Evans, "Synthesis and characterisation of advanced ball-milled Al-Al₂O₃ nanocomposites for selective laser melting," *Powder Technology*, vol. 297, pp. 183–192, 2016.
- [10] N. Senthil Kannan, R. Parameshwaran, P. T. Saravanakumar, P. M. Kumar, and M. L. Rinawa, "Performance and quality improvement in a foundry industry using fuzzy MCDM and lean methods," *Arabian Journal for Science and Engineering*, pp. 1–12, 2022.
- [11] W. I. Gu, "Bulk Al/SiC nanocomposite prepared by ball milling and hot pressing method," *Transactions of Nonferrous Metals Society of China*, vol. 16, pp. s398–s401, 2006.
- [12] V. Erturun and O. Sahin, "Investigation of microstructural evolution in ball-milling of SiC reinforced aluminum matrix composites," *Powder Metallurgy and Metal Ceramics*, vol. 57, no. 11-12, pp. 687–696, 2019.
- [13] P. Kishore, P. M. Kumar, and D. Dinesh, "Wear analysis of Al 5052 alloy with varying percentage of tungsten carbide," *AIP Conference Proceedings*, vol. 2128, no. No. 1, 2019, July.
- [14] P. Garg, A. Jamwal, D. Kumar, K. K. Sadasivuni, C. M. Hussain, and P. Gupta, "Advance research progresses in aluminium matrix composites: manufacturing & applications," *Journal of Materials Research and Technology*, vol. 8, no. 5, pp. 4924–4939, 2019.
- [15] P. W. Muchiri, V. M. Mwalukuku, K. K. Korir, G. O. Amolo, and N. W. Makau, "Hardness characterization parameters of Niobium Carbide and Niobium Nitride: a first principles study," *Materials Chemistry and Physics*, vol. 229, pp. 489–494, 2019.
- [16] M. Cuppari and S. Santos, "Physical properties of the NbC carbide," *Metals*, vol. 6, no. 10, p. 250, 2016.
- [17] T. Satish Kumar, G. Suganya Priyadarshini, S. Shalini, K. Krishna Kumar, and R. Subramanian, "Characterization of NbC-reinforced AA7075 alloy composites produced using friction stir processing," *Transactions of the Indian Institute of Metals*, vol. 72, no. 6, pp. 1593–1596, 2019.
- [18] D. N. Travessa, M. J. Silva, and K. R. Cardoso, "Niobium carbide-reinforced Al matrix composites produced by high-energy ball milling," *Metallurgical and Materials Transactions B*, vol. 48, no. 3, pp. 1754–1762, 2017.
- [19] A. T. Ertürk, M. Şahin, and M. Aras, "Tribological behavior of SiC particulate reinforced AA5754 matrix composite under dry and lubricated conditions," *Transactions of the Indian Institute of Metals*, vol. 70, no. 5, pp. 1233–1240, 2017.
- [20] A. T. Erturk, M. E. Bulduk, G. Tarakçi, G. Özer, and E. Yazar, "Investigation of the microstructure and mechanical characteristics of lattice structures produced by laser powder bed fusion method," *Metals and Materials International*, vol. 28, no. 1, pp. 155–167, 2022.
- [21] Y. Li, D. Gu, H. Zhang, and L. Xi, "Effect of trace addition of ceramic on microstructure development and mechanical properties of selective laser melted AlSi10Mg alloy," *Chinese Journal of Mechanical Engineering*, vol. 33, no. 1, p. 33, 2020.
- [22] J. W. Carson and B. H. Pittenger, "Bulk properties of powders, içinde," *ASM Handbook Volume*, vol. 7, pp. 287–301, 1998.
- [23] D. Geldart, E. C. Abdullah, A. Hassanpour, L. C. Nwoke, and I. Wouters, "Characterization of powder flowability using measurement of angle of repose," *China Particuology*, vol. 4, no. 3-4, pp. 104–107, 2006.
- [24] M. A. Kaleem, M. Z. Alam, M. Khan, S. H. I. Jaffery, and B. Rashid, "An experimental investigation on accuracy of Hausner Ratio and Carr Index of powders in additive manufacturing processes," *Metal Powder Report*, vol. 76, pp. 1–5, 2020.

Retraction

Retracted: Dynamic Analysis and Fabrication of Single Screw Conveyor Machine

Advances in Materials Science and Engineering

Received 11 July 2023; Accepted 11 July 2023; Published 12 July 2023

Copyright © 2023 Advances in Materials Science and Engineering. This is an open access article distributed under the Creative Commons Attribution License, which permits unrestricted use, distribution, and reproduction in any medium, provided the original work is properly cited.

This article has been retracted by Hindawi following an investigation undertaken by the publisher [1]. This investigation has uncovered evidence of one or more of the following indicators of systematic manipulation of the publication process:

- (1) Discrepancies in scope
- (2) Discrepancies in the description of the research reported
- (3) Discrepancies between the availability of data and the research described
- (4) Inappropriate citations
- (5) Incoherent, meaningless and/or irrelevant content included in the article
- (6) Peer-review manipulation

The presence of these indicators undermines our confidence in the integrity of the article's content and we cannot, therefore, vouch for its reliability. Please note that this notice is intended solely to alert readers that the content of this article is unreliable. We have not investigated whether authors were aware of or involved in the systematic manipulation of the publication process.

Wiley and Hindawi regrets that the usual quality checks did not identify these issues before publication and have since put additional measures in place to safeguard research integrity.

We wish to credit our own Research Integrity and Research Publishing teams and anonymous and named external researchers and research integrity experts for contributing to this investigation.

The corresponding author, as the representative of all authors, has been given the opportunity to register their agreement or disagreement to this retraction. We have kept a record of any response received.

References

- [1] S. Moorthi, M. Megaraj, L. Nagarajan, A. Karthick, M. Bharani, and P. P. Patil, "Dynamic Analysis and Fabrication of Single Screw Conveyor Machine," *Advances in Materials Science and Engineering*, vol. 2022, Article ID 3843968, 10 pages, 2022.

Research Article

Dynamic Analysis and Fabrication of Single Screw Conveyor Machine

Sundarraaj Moorthi,¹ Meikandan Megaraj,¹ Lenin Nagarajan,¹ Alagar Karthick,^{2,3} Murugesan Bharani ,⁴ and Pravin P. Patil⁵

¹Department of Mechanical Engineering, Veltech Rangarajan Dr. Sagunthala R & D Institute of Science and Technology, Avadi 600 062, India

²Renewable Energy Lab, Department of Electrical and Electronics Engineering, KPR Institute of Engineering and Technology, Coimbatore 641407, Tamilnadu, India

³Departamento de Quimica Organica, Universidad de Cordoba, Edificio Marie Curie (C-3), Ctra Nnal IV-A, Km 396, E14014 Cordoba, Spain

⁴School of Textile Leather and Fashion Technology Kombolcha 208, Kombolcha Institute of Technology, Wollo University, South Wollo, Ethiopia

⁵Department of Mechanical Engineering, Graphic Era Deemed to be University, Bell Road, Clement Town, 248002 Dehradun, Uttarakhand, India

Correspondence should be addressed to Murugesan Bharani; bharani.murugesan@kiot.edu.et

Received 10 February 2022; Revised 21 March 2022; Accepted 30 March 2022; Published 12 April 2022

Academic Editor: Penchal Reddy

Copyright © 2022 Sundarraaj Moorthi et al. This is an open access article distributed under the Creative Commons Attribution License, which permits unrestricted use, distribution, and reproduction in any medium, provided the original work is properly cited.

The design and development of machine tools play a vital role in the current economic growth. It facilitates the reduction of manufacturing cost coping with a quickly changing business environment. During the design of the machine tool, the dynamic characteristics need to be calibrated for avoiding uncertainties. This paper investigates the design, dynamic characteristics, and development of a single screw conveyor machine which is used to blend waste plastic material with catalysts. The conveyor machine model is created based on the idea developed from filament extruder machine with Pro-E solid modelling software. Its multibody dynamic analysis was carried out for the selected operational requirements in the ADAMS View. It shows that when the conveyor screw operated above the velocity of 42 m/s, the deformation will occur at a maximum value of 4.23 mm. The rigid body dynamic was carried out in ANSYS to solve the performance forecasting problems at their design stage. The dynamic analysis results were suggested to improve the conveying machine and driving mechanisms design parameters.

1. Introduction

Solid modelling is currently the primary method to create new ideas for products and structures. The main advantage of solid modelling is that it gives a realistic visual representation of the product and helps the user make changes quickly and easily. During the design process, the availability, accessibility, and environmental aspects are considered. However, individual components dynamic characteristics need to be analyzed to make the designed model into higher durability and effective one [1, 2]. Ahmad

et al. [3] surveyed that around 7 percentage of the gross national product failed due to product performance-related issues. Most products are developed from research and development. Ahmad and Ismail et al. [4, 5] reviewed the problems during the production of new products and their aftermarket. They suggested that before the product came into manufacturing, its characteristics need to be analyzed thoroughly to avoid failure rates and manufacturing cost. They also presented a framework for the analysis of products during their design process. Li et al. and Jiao et al. [6, 7] surveyed the requirement of new product developments in

the market to satisfy customer requirements. He framed the topological structure to help the designer to develop new products. The topological structure includes customer requirement and existing products in the market and their failure reasons. He identified that most of the product failures happen in improper design and not considering the machine's dynamic characteristic and safety factor. He [8] discussed and developed the empirical relationship of modelling techniques and static and dynamic characteristics of welded joints and analyzed its possible failure modes. Lahari and Srinivas Sharma [9] developed single screw extruder for recycling of waste plastic material and examined the parametric analysis of the developed model; from the analytical report, they identified decreased pressure due to barrel radius and higher length of the screw. Wang et al. and Tso et al. [10, 11] discussed the design and analysis of mechanical linkages used in mechanical press. They optimized the linkage length to provide the best actuation. He suggested that computer-aided modelling and analysis techniques make the design more perfect and reduce the failure causes during the design stage itself. Hence, the production cost can be saved. Singh et al. [12] studied the making of energy storage device through 3D printing technique by utilizing commercially available waste plastics based 3D printer filament developed through twin screw extruder machine. The filament was developed with additives of zinc metal and the additives of different chemicals for enabling conduciveness.

The present work investigates modelling and dynamic analysis of a single screw conveyor machine. The dynamic analysis was carried out with the ADAMS View's help by considering the conveyor machine operational parameters. The outcome results were considered for the conveyor machine's development to avoid failure due to dynamic characteristics.

2. Materials and Methods

2.1. Modelling of Single Screw Conveyor (SSC) Machine. The basic idea for developing a conveyor machine is taken by considering a single screw filament extruder and its operational parameters. Filament extruders are used to melt the plastics and feed them through the nozzle in the desired shape. In the case of a screw conveyor, the materials are transferred from one place to another place using a rotating helical screw blade connecting these two ideas, and the development of a single screw conveyor was generated. The 3D solid modelling of a single screw conveyor was created with the help of Pro-E 5.0 software. The conveyor machine consists of a hopper, screw barrel, helical screw, and driving mechanisms. For creating a conveyor screw from the filament extruder, the screw nomenclature is studied, and it is shown in Figure 1. The main component of the conveyor screw machine designed in Pro-E software is shown in Figures 2–4, respectively.

2.2. Multibody Dynamic Analysis of Single Screw Conveyor Machine Using MSC ADAMS. The conveyor machine and its assembly components are created through Pro-E software; it

was saved into Parasolid file format to make the ease of exchanging the modelling data of created model into ADAM View/ANSYS environment. ADAMS View is a program that allows the building of mechanical systems models and simulates the models' full-motion behaviour [14–16]. It can also be used to quickly analyze multiple design variations until the optimal design is found. ANSYS Rigid dynamics helps to understand mechanical systems' motion behaviour in the design cycle [17–20]. In the proposed research, the single screw conveyor model is analyzed with the help of ADAMS View and ANSYS 14.5 software. In ADAMS, the model's constraints and boundary conditions are applied using the build tool. The constraint consists of relative movement between the components.

A screw conveyor machine consists of links and joints. Each component in the conveyor will move or rotate with the preceding constraints. The model imported in the ADAMS View Environment and the boundary conditions (constraints) created to model are as shown in Figure 5.

The initial simulation was taken to validate and for finding any redundant constraint added to the model. Afterwards, the operational functions of the screw are applied, and its dynamic analysis was carried out. Initially, the conveyor machine is operated for a period of 20 seconds with the speed of 3000 rpm, and its performance behaviour is taken. The two sets of markers are located in the model one which is at the screw centre and another is at the barrel edge to find the displacement of the conveyor screw. The operation functions can be improved by adding more complex elements like friction or general state equation to make the model accurate. The results of the position and velocity of a conveyor screw in the X-axis are obtained in graphic form using the windows of measures interface shown in Figures 6(a) and 6(b), respectively.

The conveyor screw is rotating at a constant speed about its longitudinal axis. The displacement field is implicit by choosing coordinates x with the conveyor screw axis, as shown in Figure 7.

$$\begin{aligned} U(x, y, z, t) &= U_0(x, t) + z\beta_x(x, t) - y\beta_y(x, t), \\ V(x, y, z, t) &= V_0(x, t) - z\phi(x, t), \\ W(x, y, z, t) &= W_0(x, t) + y\phi(x, t). \end{aligned} \quad (1)$$

U , V , and W are the flexural displacements of the conveyor screw at any point of its cross section in x , y , and z directions. The variables U_0 , V_0 , and W_0 are the flexural displacements of the screw axis, while β_x and β_y are the rotation angles of the screw, about the y - and z -axis, respectively. ϕ is the angular displacement of the conveyor screw due to its torsional deformation.

In ADAMS View Environment, the rotational displacement, velocity, and accelerations can be calculated with the help of markers created in the conveyor screw at prescribed locations, and markers act as an imaginary point with coordinate values.

2.3. Rigid Dynamic Analysis of Single Screw Conveyor Machine Using ANSYS. In the ANSYS workbench environment, the model saved in the Parasolid format from Pro-E software is

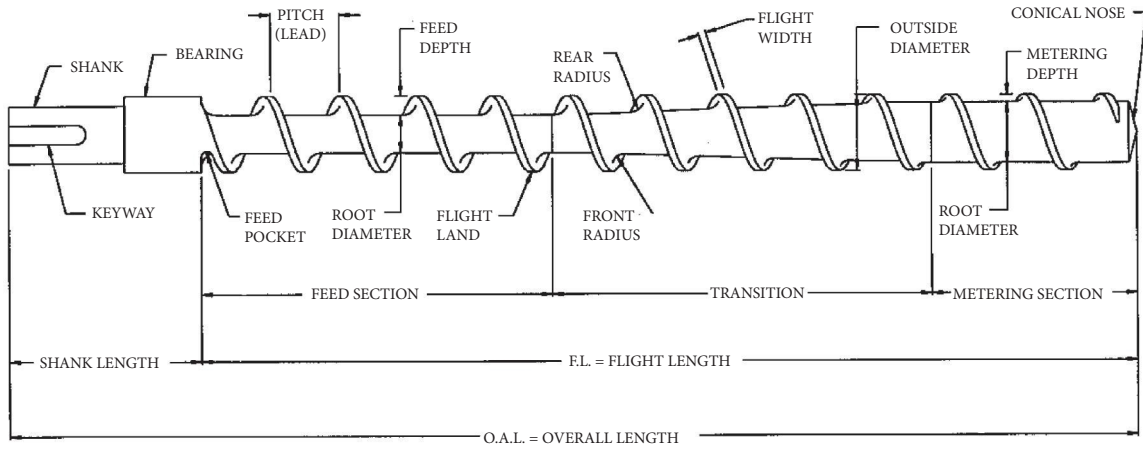


FIGURE 1: Screw nomenclature [13].

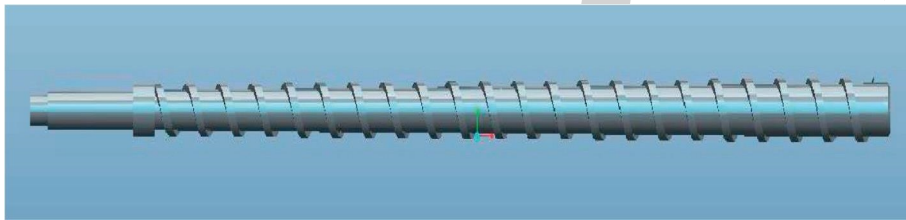


FIGURE 2: Pro-E model of conveyor screw.

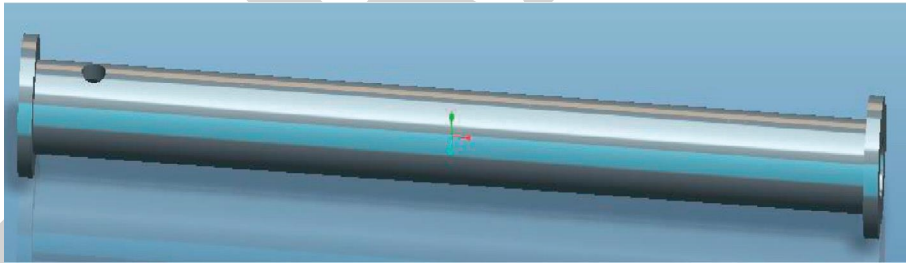


FIGURE 3: Pro-E model of conveyor screw barrel.

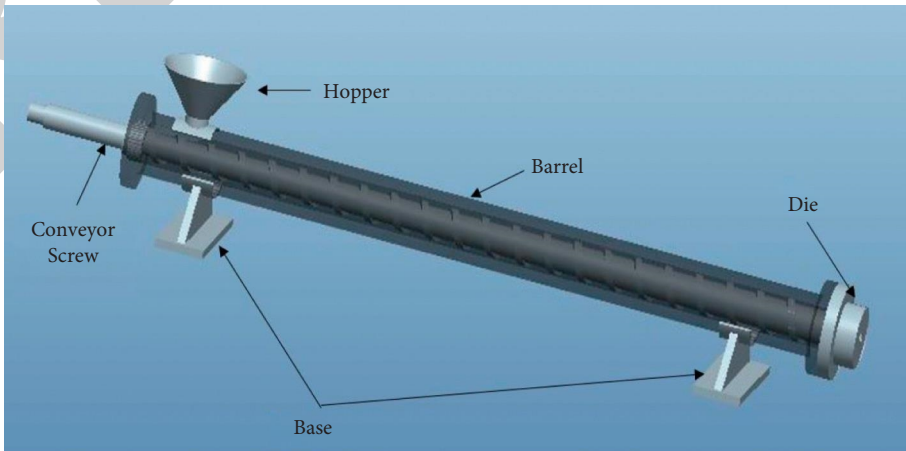


FIGURE 4: Assembly view of conveyor screw machine.

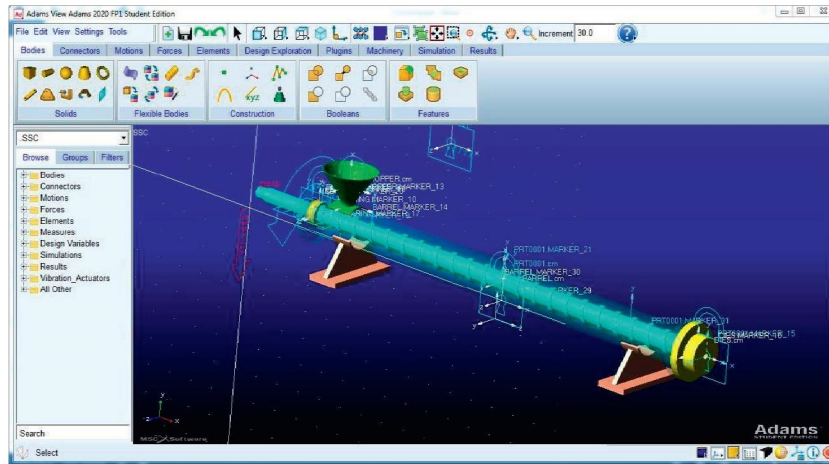
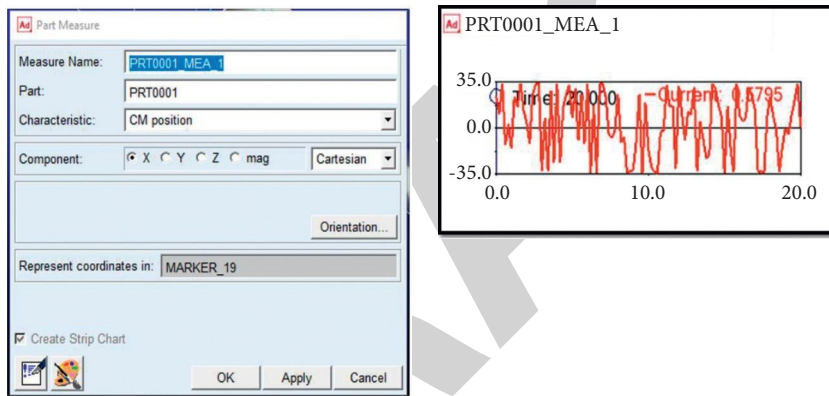


FIGURE 5: ADAMS View Environment and the constraint created to model.



(a)

(b)

FIGURE 6: (a) Window of the part measure and (b) position of conveyor screw-in X-axis direction.

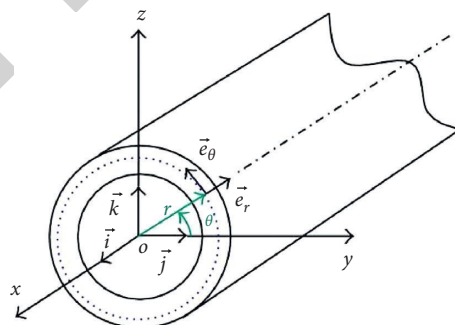


FIGURE 7: Cylindrical-coordinate system [14].

imported, and connections between the assembly models are added with the joints menu toolbar. The screw is operated with a speed of 3000 rpm, and its characteristics are analyzed. The model imported to the ANSYS workbench environment and the model's connections are as shown in Figure 8.

2.4. Development of Single Screw Conveyor. The single screw conveyor machine is developed by considering the resulting outcome from ADAMS and ANSYS software. The fabricated single screw conveyor machine and its components are shown in Figures 9 and 10, respectively.

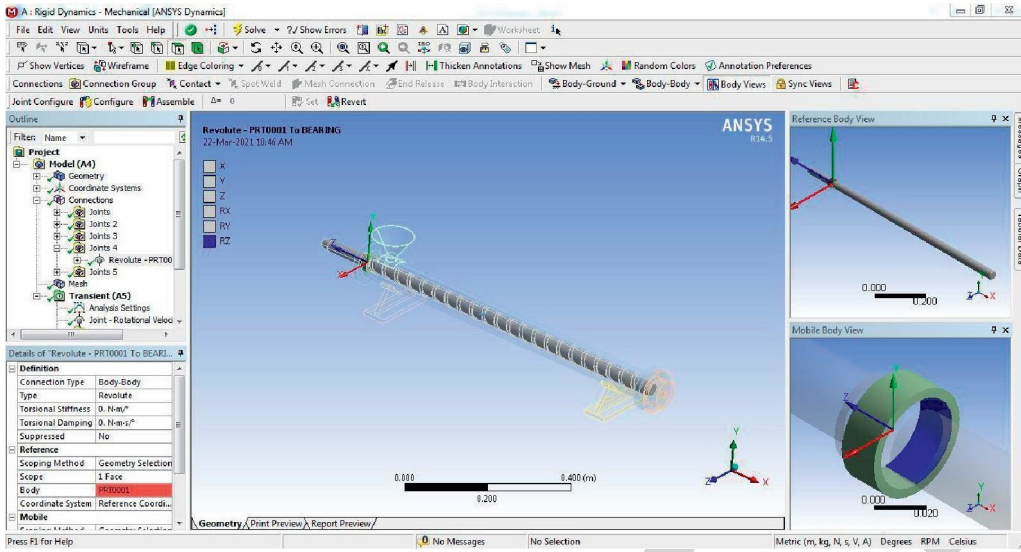


FIGURE 8: ANSYS environment and the constraint created to conveyor model.



FIGURE 9: Machining image of single screw conveyor.

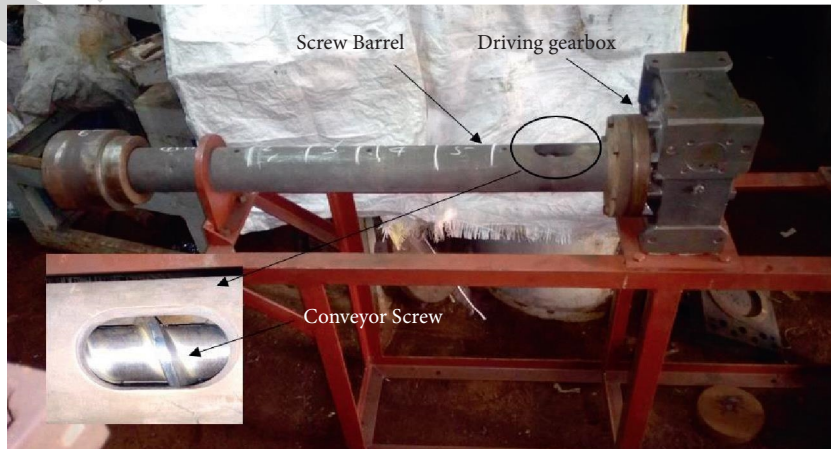


FIGURE 10: Single screw conveyor and driving gearbox setup.

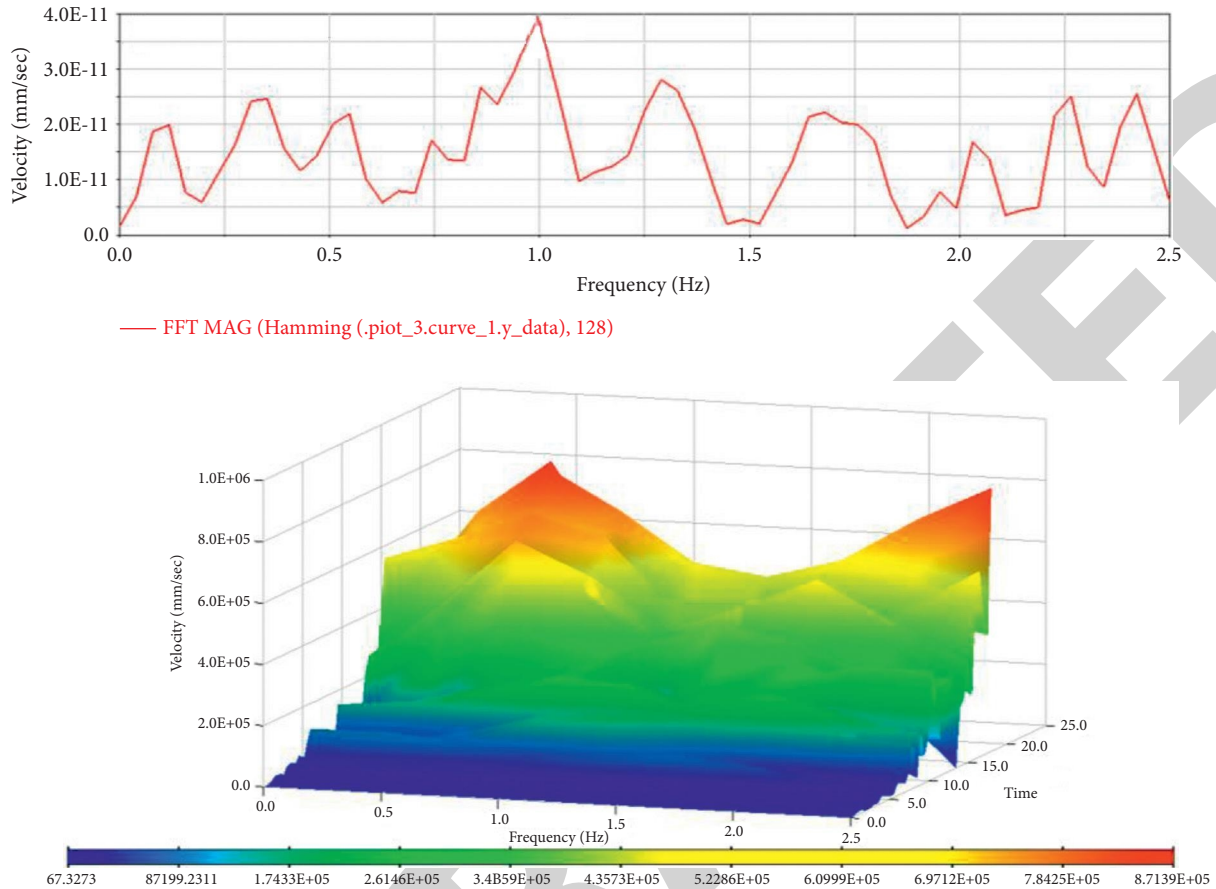


FIGURE 11: Velocity of single screw conveyor.

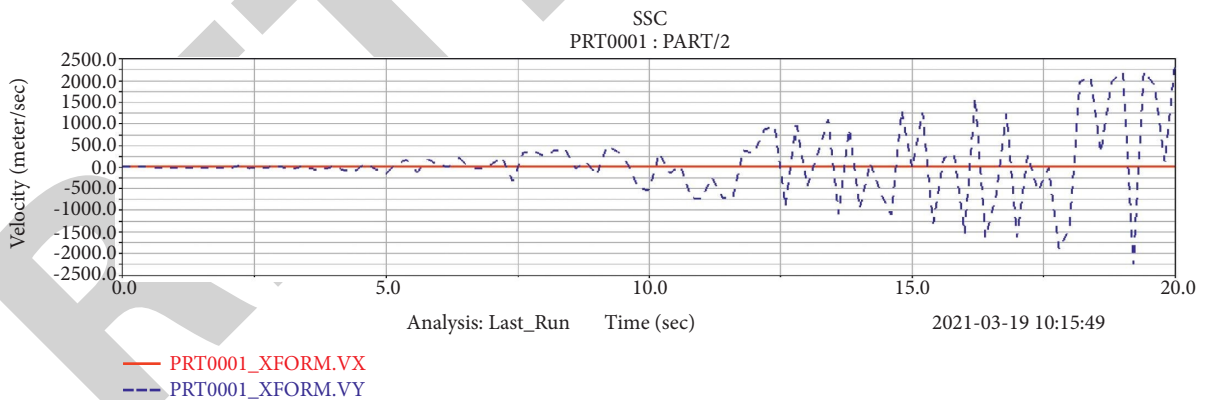


FIGURE 12: Velocity of single screw conveyor concerning time period.

3. Results and Discussion

3.1. Velocity, Deformation, and Acceleration of Single Screw Conveyor in ADAMS View. The dynamic response characteristics help to identify the vibration at a particular region and its velocity compound. To study the dynamic characteristic and effect, the single screw conveyor machine is freely allowed to operate in the ADAMS View Environment. Its dynamic responses are noted to determine the velocity,

acceleration, and displacement of the system or component. The frequency of a single screw conveyor concerning velocity is as shown in Figure 11.

The velocity and deformation of a conveyor screw analyzed in the ADAMS View Environment are presented in Figures 12 and 13, respectively. It shows that the maximum deformation value of a single screw conveyor (SSC) is 4.23 mm concerning the operating period. Based on the results data analyzed from the ADAMS View, the velocity of

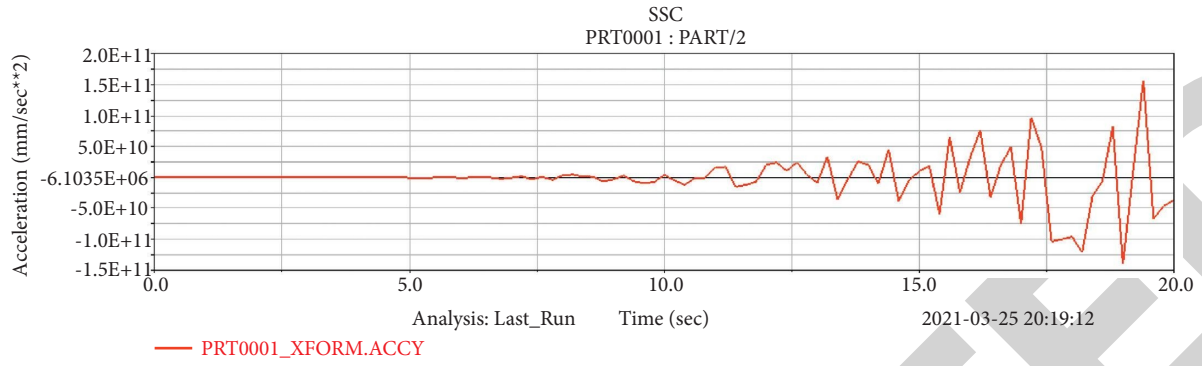


FIGURE 13: Acceleration of single screw conveyor.

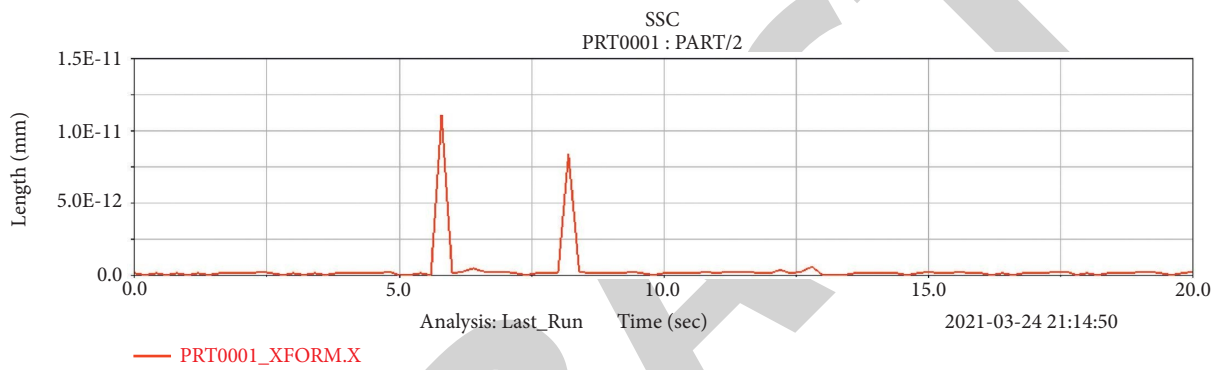


FIGURE 14: Deformation of single screw conveyor.

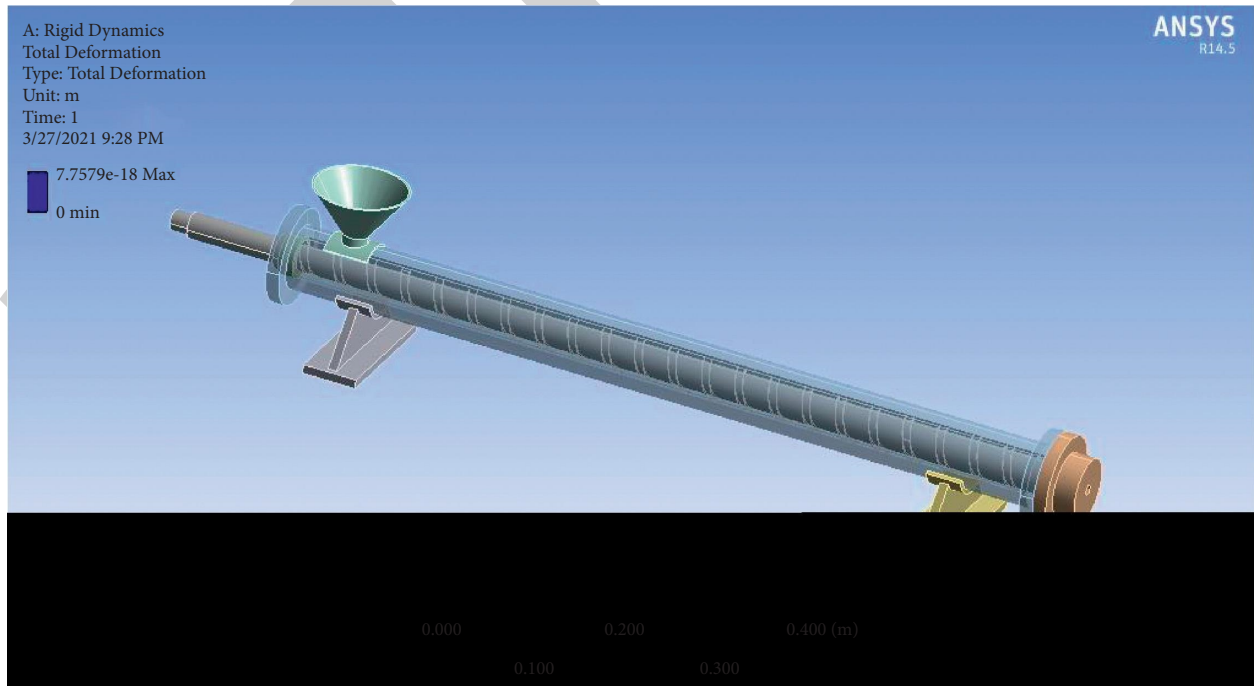


FIGURE 15: Total deformation of single screw conveyor.

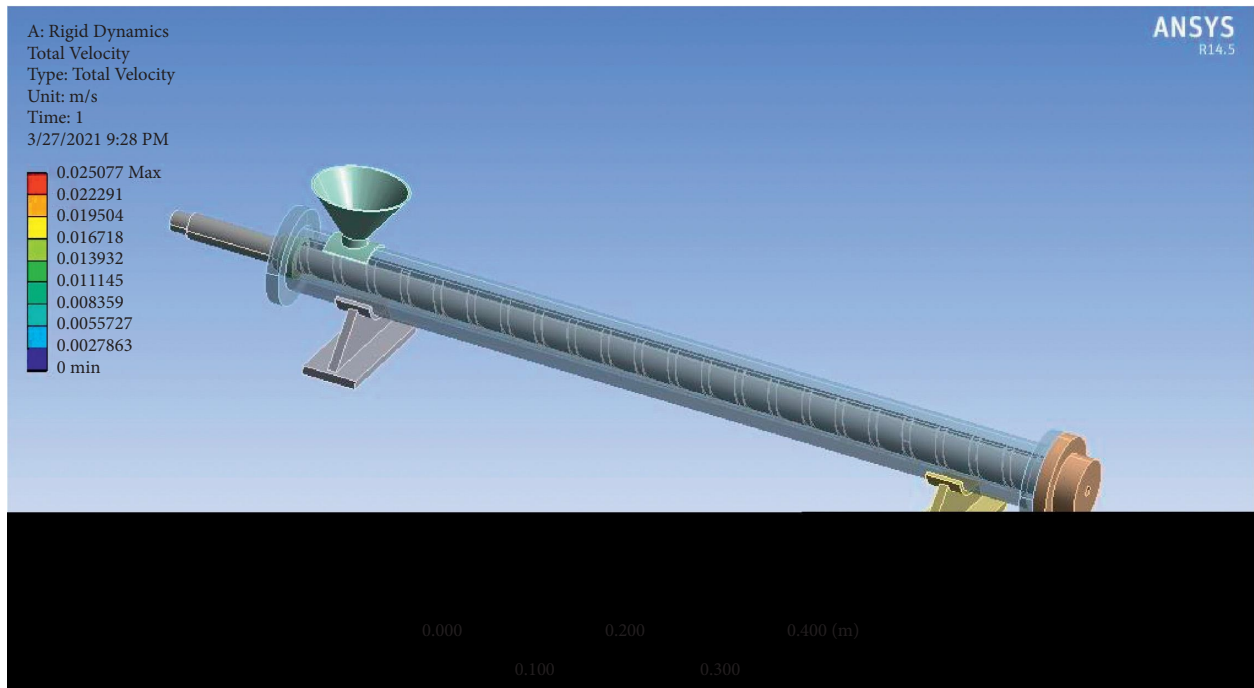


FIGURE 16: Total velocity of single screw conveyor.

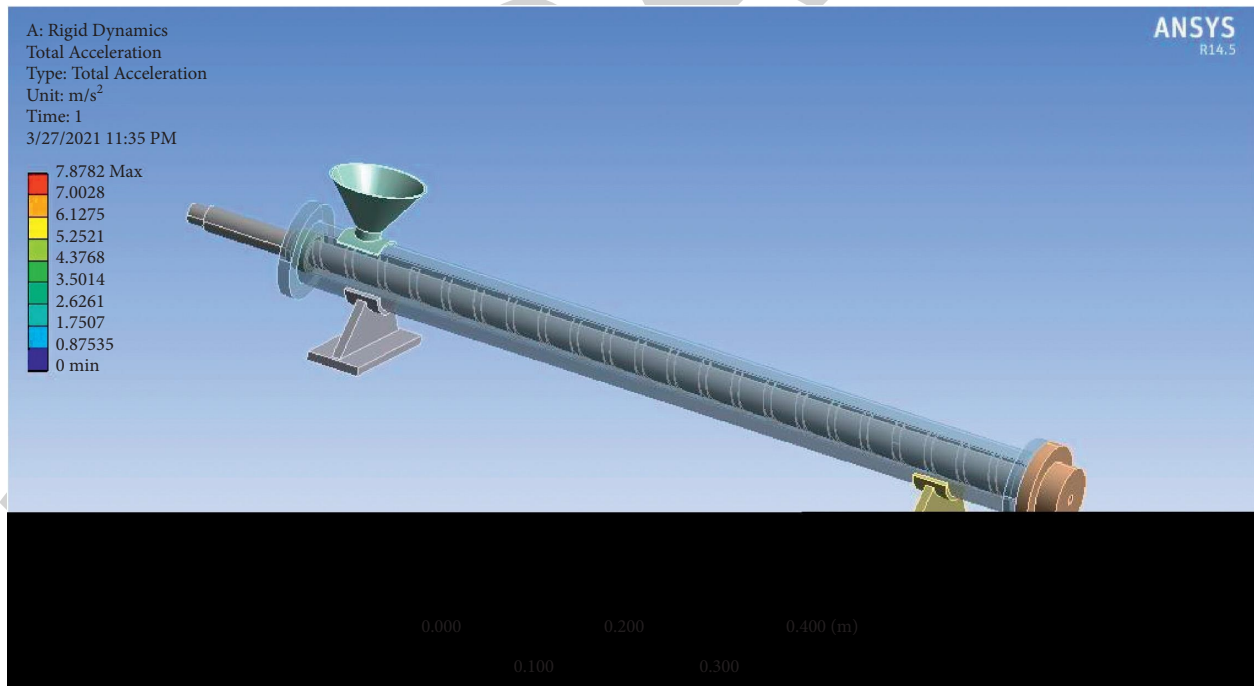


FIGURE 17: Total acceleration of single screw conveyor.

the conveyor screw increased above 42 m/s leads to vibration and also the velocity distribution of components leads to failure of bearing systems. Hence, the single screw conveyor should be operated below its critical velocity.

The acceleration value of a single screw conveyor is shown in Figure 14. Based on the acceleration data from the ADAMS View Environment, the control system can be

developed. In many cases, maximum speed and acceleration are predominant characteristics of the machine tool component, which helps create proper driving mechanisms.

3.2. Deformation, Velocity, and Acceleration of Single Screw Conveyor (SSC) in ANSYS. The output result of ADAMS

View software is considered for the input speed of the conveyor machine in ANSYS. The screw is operated with the maximum speed of 3000 rpm, and its characteristic is analyzed. Figure 15 shows the total deformation of the conveyor screw; it was observed that during the rotary motion, the single screw conveyor tends to deform at a maximum range of 4.23 mm. Hence, the clearance between the barrel to the screw conveyor can be given above its maximum deformation value during its fabrication.

The total velocity outcome of a single screw conveyor analyzed from ANSYS is as shown in Figure 16. It shows the velocity of all the components combined by vectorial addition, and it has a maximum velocity of 42 m/s. The result is compared with the multibody dynamic analysis result value from ADAMS View, and it showed the lower value. Hence, the velocity of single screw conveyor will not create vibration to the machine tool component.

The total acceleration of a single screw conveyor analyzed from ANSYS is shown in Figure 17. It was observed that the maximum acceleration of 7.87 m/s^2 is obtained for a unit time. Hence, the acceleration value should be considered during the development of the driving mechanism for the single screw conveyor.

4. Conclusion

- (i) The multibody dynamic analysis results from ADAMS View shows the maximum displacement and velocity of the single screw conveyor. During the rotary motion, the conveyor screw tends to vibrate in the lateral and vertical axis direction. Hence, the conveyor machine should operate below its maximum velocity to avoid the resonance and stress created over the surface of the screw.
- (ii) The rigid body dynamic analysis result from the ANSYS workbench shows the velocity, deformation, and acceleration characteristics of a single screw conveyor. The velocity of the single screw conveyor creates less total displacement, so the clearance between the screw to the barrel should be appropriately maintained. The acceleration parameter needs to be considered during the development of the control/driving mechanism.

Data Availability

The data used to support the findings of this study are included within the article.

Conflicts of Interest

The authors declare that there are no conflicts of interest regarding the publication of this article.

Acknowledgments

Alagar Karthick gratefully acknowledges group FQM-383 from Universidad de Cordoba, Spain, for the provision of a honorary research position in the group.

References

- [1] V. V. Telegin, A. M. Kozlov, and V. I. Sakalo, "Solid modeling and dynamic analysis of mechanisms of press-forging machines," *Procedia Engineering*, vol. 206, pp. 1258–1263, 2017.
- [2] J. Zhang, R. Zhang, G. Ren, and X. Zhang, "A method for using solid modeling CAD software to create an implant library for the fabrication of a custom abutment," *The Journal of Prosthetic Dentistry*, vol. 117, no. 2, pp. 209–213, 2017.
- [3] M. F. Ahmad, H. Chun, N. Abdul Hamid et al., "The impact of product design and process design towards new product performance in manufacturing industry: a survey result in Malaysia," *International Journal of Supply Chain Management*, vol. 7, no. 2, pp. 102–105, 2018.
- [4] M. F. Ahmad, N. Zakuan, A. Jusoh, S. M. Yusof, J. Takala, and M. S. M. Arif, "Comparative study of TQM practices between Japanese and non-Japanese companies: proposed conceptual framework," *Advanced Materials Research*, vol. 903, pp. 371–377, 2014.
- [5] R. Ismail and I. Jajri, "Analisis perubahan kecekapan teknikal, perubahan teknologi, pertumbuhan produktiviti faktor keseluruhan dan pertumbuhan output dalam industri peralatan pengangkutan di Malaysia," *Jurnal Teknologi*, vol. 49, no. 1, pp. 31a–48, 2008.
- [6] X. Li, W. Zhao, Y. Zheng, R. Wang, and C. Wang, "Innovative product design based on comprehensive customer requirements of different cognitive levels," *TheScientificWorldJOURNAL*, vol. 2014, Article ID 627093, 2014.
- [7] J. Jiao and C.-H. Chen, "Customer requirement management in product development: a review of research issues," *Concurrent Engineering*, vol. 14, no. 3, pp. 173–185, 2006.
- [8] X. He, "Finite element analysis of laser welding: a state of art review," *Materials and Manufacturing Processes*, vol. 27, no. 12, pp. 1354–1365, 2012.
- [9] T. R. Lahari and G. Srinivas Sharma, "Parametric analysis of Single Screw extruder for processing of re-cycled plastics," *International Journal of Current Engineering and Technology*, vol. 12, no. 1, pp. 9–14, 2022.
- [10] A. C.-Y. Wang and L. W. Cisko, "Computer-aided design, analysis and optimization of mechanical press linkages," *MATERIAL AND MANUFACTURING PROCESS*, vol. 1, no. 3-4, pp. 455–471, 1986.
- [11] P. L. Tso and K. C. Liang, "A nine-bar linkage for mechanical forming presses," *International Journal of Machine Tools and Manufacture*, vol. 42, no. 1, pp. 139–145, 2002.
- [12] R. Singh, H. Singh, I. Farina, F. Colangelo, and F. Fraternali, "On the additive manufacturing of an energy storage device from recycled material," *Composites Part B: Engineering*, vol. 156, pp. 259–265, 2019.
- [13] H. F. Giles, E. M. Mount, and J. R. Wagner, *Extrusion: The Definitive Processing Guide and Handbook*, William Andrew, Norwich, NY, 2004.
- [14] D. Srinivasan, G. Veerappan, R. M et al., "Investigation on electric erosion behavior of nickel-based super alloy (Waspaloy: Ni, Cr, Co, Mo, Ti, Al) using response surface methodology," *Surface Topography: Metrology and Properties*, vol. 9, no. 3, Article ID 035006, 2021.
- [15] B. Stalin, M. Ravichandran, G. T. Sudha et al., "Effect of titanium diboride ceramic particles on mechanical and wear behaviour of Cu-10 wt% W alloy composites processed by P/ M route," *Vacuum*, vol. 184, Article ID 109895, 2021.
- [16] S. V. Alagarsamy, R. Balasundaram, R. M, V. Mohanavel, A. Karthick, and S. S. Devi, "Taguchi approach and decision tree algorithm for prediction of wear rate in zinc oxide-filled